Multivalley Simulation and Design of Quantum Cascade Lasers

X. Gao, D. Botez, and I. Knezevic

Department of Electrical and Computer Engineering, University of Wisconsin–Madison,

1415 Engineering Dr, Madison, WI 53706-1691, USA

Contents

Book chapter in Encyclopedia of Nanoscience and Nanotechnology,
Edited by H. S. Nalwa, American Scientific Publishers, in press. (2008)

X. Gao, D. Botez, and I. Knezevic, "Multivalley simulation and design of quantum cascade lasers,"
in Encyclopedia of Nanoscience and Nanotechnology, Edited by H. S. Nalwa, American Scientific Publishers, in press. (2008)

I. INTRODUCTION

Quantum cascade lasers (QCLs) are electrically pumped unipolar coherent light sources. They operate based on intersubband transitions in multiple-quantum-well (MQW) heterostructures, designed by means of band-structure engineering. The operating principle of these lasers is based on two fundamental phenomena in quantum mechanics: tunneling and quantum confinement. The emission wavelength of this type of laser is not limited by the band gap of constituent materials, but can be tuned in a very wide range by tailoring the layers thicknesses.

The basic concept of QCLs was introduced by Kazarinov and Suris [1] in 1971. It took more than twenty years before an actual working device was first demonstrated by Faist *et al.* [2] at Bell Laboratories in 1994. Since then, the lasers' performance has remarkably improved. The emission wavelength has spanned the mid- to far-infrared spectral range (from 3 to 190 μm). At present, the best device performances are obtained at wavelengths between 3.8-9.5 μm, where continuous-wave (CW) room temperature operation is routinely achieved [3].

QCLs are rapidly acquiring new applications, due to their wide tunable emission wavelength range and the capability for above-room-temperature pulsed and CW operation. Mid-infrared (mid-IR) QCLs have been used for real-time spectroscopic detection of environmental gases, whose spectra lie in the 3-5 μm and 8-13 μm atmospheric windows [4–6]. Mid-IR QCLs can also be well adapted for chemical spectroscopy in medical applications [7, 8]. They are also candidates for free space telecommunications: e.g., the Jet Propulsion Laboratory has just chosen a QCL-based sensor for the 2009 Mars Science Laboratory mission [6]. Other applications may include cruise control in conditions of poor visibility, collision-avoidance radar, and industrial process control [9]. Thus, QCLs appear as the semiconductor solution for lasers in the mid- and far-infrared spectral regions [3].

Quantum cascade lasers are made of a sequence of alternating wide band-gap and narrow band-gap semiconductor layers. The alternating wide and narrow band-gap layers form quantum wells for carriers. The thickness of each layer is in the range of a few nanometers. These multiple-quantum-well structures consist of repeated stages (typically 25-70), each stage containing an active region and an electron-injecting region (injector). The injector also works as the electron-collecting region (collector) as well as the Bragg-mirror region

X. Gao, D. Botez, and I. Knezevic, "Multivalley simulation and design of quantum cascade lasers,"
in Encyclopedia of Nanoscience and Nanotechnology, Edited by H. S. Nalwa, American Scientific Publishers, in press. (2008)

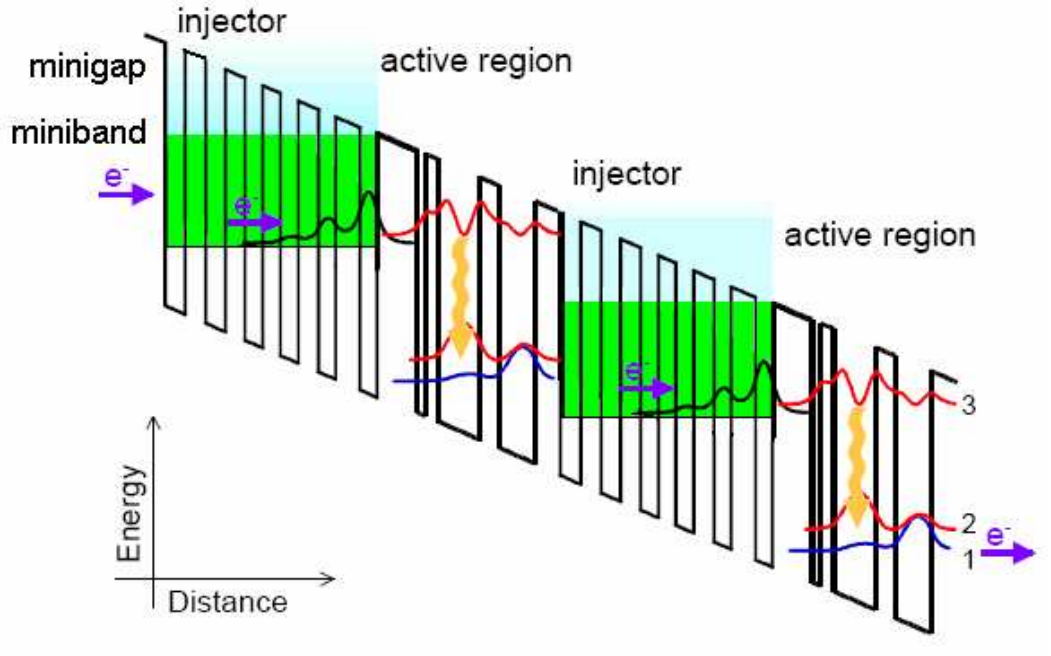

FIG. 1. Conduction band profile in two adjacent stages of a generic QCL under an applied bias.

(for the electrons in the upper lasing level) for the previous stage. A certain number of layers in each injector region are n-type doped with silicon to serve as an electron reservoir. Figure 1 depicts the conduction band profile in two adjacent stages of a generic QCL under an applied bias. Due to the quantum confinement in multiple quantum wells, a miniband (green in Fig. 1) and a minigap (light blue) are formed in the injector region, but discrete energy levels are formed in the active region (levels 3, 2, 1 in the figure). When an electrical current flows through such a structure, electrons from the injector region tunnel through the barriers and fill the upper lasing level 3 in the active region. Electrons in level 3 make radiative transitions (the yellow wavy lines in Fig. 1) to the lower lasing level 2, giving off photons, provided there is population inversion between the two levels (i.e., level 3 has more electrons than level 2). Once electrons relax to level 2, this level gets depopulated fast to level 1 by the electron-longitudinal optical phonon interaction processes, which in turn ensures the population inversion between levels 3 and 2. Electrons then tunnel to the next-stage injector region and trigger the photon-emitting process in the next stage. Intuitively, when an electrical current flows through a quantum cascade laser, electrons cascade down an energy staircase emitting a photon at each step, which makes this type of laser earn its name. Each injected electron generates N_p photons, where N_p is the number of stages, leading to

X. Gao, D. Botez, and I. Knezevic, "Multivalley simulation and design of quantum cascade lasers,"
in Encyclopedia of Nanoscience and Nanotechnology, Edited by H. S. Nalwa, American Scientific Publishers, in press. (2008)

an optical power proportional to N_p. This cascading process leads to the intrinsic high-power capability of QCLs, but also to high voltages and subsequently low power-conversion efficiency (so called wallplug efficiency) which, at the present time, prevents their practical use as CW or quasi-CW light sources.

A. State-of-the-Art Quantum Cascade Lasers

The first demonstration of a QCL was achieved in 1994 by Faist *et al.* [2] using the InGaAs/InAlAs heterostructure lattice-matched to an InP substrate. Since then, tremendous progress has been made in InP-based QCL device performance. CW room-temperature (RT) operation was first demonstrated by Beck *et al.* [10]. Following this breakthrough, InP-based QCLs have been reported to achieve CW RT operation at wavelengths between 3.8 and 9.5 μm [10–17], with devices in the 4.5-5.5 μm range [14–17] reaching optical output powers in the range of 300-600 mW. However, with one exception [17], all QCLs operating at CW RT have relatively low ($< 5\%$) wallplug efficiency, and their electro-optical characteristics are extremely temperature sensitive, due both to carrier backfilling of the lower lasing level and carrier leakage out of the upper lasing level. Even the exception, that is a narrow-width, buried-heterostructure device which achieved 9% wallplug efficiency at RT [17], has a fast decreasing slope efficiency due to carrier leakage (to the continuum). The emission wavelengths from 3.5 [18] to 24 μm [19] have been obtained using the same InGaAs/InAlAs materials system grown on InP. A shorter wavelength of 3.05 μm was recently achieved by both Semtsiv *et al.* [20], using strain-compensated $In_{0.73}Ga_{0.27}As/In_{0.55}Al_{0.45}As/AlAs$ on InP, and by Revin *et al.* [21], using $In_{0.53}Ga_{0.47}As/AlAs_{0.56}Sb_{0.44}$ lattice-matched to InP. Although these shorter-wavelength QCLs can currently only operate in pulsed mode up to low temperatures (150 K), the emission wavelength of high-performance, CW RT InP-based QCLs is expected to cover the entire 3-5 μm atmospheric window in the very near future.

The GaAs/AlGaAs heterostructure grown on a GaAs substrate is another very important materials system for the fabrication of QCLs. In fact, GaAs substrate is the only contender to InP for fabricating QCLs [22]. Compared to InP-based QCLs, GaAs QCLs have several advantages. First of all, GaAs is the most technologically mature semiconductor after silicon, so its feature parameters are accurately determined and documented. Secondly, GaAs QCLs based on the deep-active-well design [23] hold the potential to achieve wallplug efficiency as

X. Gao, D. Botez, and I. Knezevic, "Multivalley simulation and design of quantum cascade lasers,"
in Encyclopedia of Nanoscience and Nanotechnology, Edited by H. S. Nalwa, American Scientific Publishers, in press. (2008)

high as 15% and watt-range CW optical power [24], thus making them potentially the first CW-operating QCLs of practical use. In addition, GaAs QCLs can achieve wavelengths in a very wide range due to the design flexibility offered by the good lattice matching across the full range of Al contents. The emission wavelengths of reported GaAs QCLs have spanned from 7.4 μm (mid-infrared) [25] to 190 μm (far-infrared) [26]. However, GaAs-based QCLs have several drawbacks that limit their performance and will be discussed in Sec. I C. This work is restricted to the study of GaAs-based mid-IR QCLs.

The very first attempt at using the GaAs/AlGaAs materials system in QCL structures was back in 1997, when Strasser *et al.* [27] reported the electroluminescence of a GaAs QCL design at 6.9 μm using 45% Al in the barriers (no lasing was observed). Since then, mid-infrared (mid-IR) GaAs-based QCLs have utilized Al contents of 33% [28–30], 45% [31–36], and 100% [37–39], respectively, in the AlGaAs barrier layers. The first lasing GaAs QCL structure [28] employed 33% Al in the barriers, and emitted at $\lambda = 9.4$ μm under pulse operation up to 140 K. With a low-loss Al-free waveguide [29], the threshold current density $J_{\rm th}$ of the 33% Al QCL design was reduced to an average of 5.0 kA/cm^2 at 77 K, and a maximum pulsed operation temperature of 200 K. Mid-IR GaAs QCLs with 33% Al in the barriers have so far achieved the highest operating temperature of 285 K under pulsed operation [30], and have not achieved CW operation.

On the other hand, great progress has been made in the device performance of GaAs/$Al_{0.45}Ga_{0.55}$As QCLs, since its first realization [31]. Room temperature pulsed operation has been reported for several active region designs, i.e., three quantum-well active region design emitting at 9.4 μm [31, 32], a superlattice active region design emitting at 12.6 μm [33], and a bound-to-continuum design emitting at 11.0 μm [34]. Continuous wave operation of 45% Al QCLs based on the original design [31] has recently been achieved [35, 36] through optimized device processing, with a maximum temperature of 150 K [36].

Several GaAs/AlAs QCLs emitting in the mid-IR spectral region have also been reported [37–39]. Though showing the lowest temperature dependence of $J_{\rm th}$ [37] and CW operation close to 30 K [38], these lasers are limited by the negative differential resistance effect, which strongly limits the maximum operating temperature [22]. By depositing InAs monolayers in the device active regions, Carder *et al.* reported room temperature pulse operation of an InAs/GaAs/AlAs QCL [40] lasing at 8.5 μm.

X. Gao, D. Botez, and I. Knezevic, "Multivalley simulation and design of quantum cascade lasers,"
in Encyclopedia of Nanoscience and Nanotechnology, Edited by H. S. Nalwa, American Scientific Publishers, in press. (2008)

B. Theoretical Approaches for QCL Transport Simulation

Much theoretical work has been done to accompany the rapid experimental developments of mid-IR QCLs. These include Monte Carlo simulations [41–44], self-consistent rate equations [45, 46], as well as nonequilibrium Green's function (NEGF) formalism [47, 48]. Among these simulation approaches, there has been a long-term debate of whether the nature of charge transport in QCL structures is coherent or incoherent. Although recent work [48] using the NEGF formalism argued that the transport in QCLs should be treated as coherent, this formalism takes enormous computation time and has to be carefully customized for each particular structure. As a result, it takes a long time to obtain useful results for improvement of experimental designs.

On the other hand, theoretical studies by Iotti and Rossi [41, 49] showed that, although clear coherent oscillations of population inversion and gain overshoot were observed during the initial transient, the oscillations are damped on the sub-picosecond timescale. This time is much shorter than the average transit time across one stage. These features have been observed experimentally [50, 51] and the timescales are comparable. Hence, they concluded that the resulting steady-state transport in mid-IR QCLs is incoherent (i.e., governed by scattering). Therefore, the QCL simulation community tends to adopt the semiclassical transport concept in their models [43–45]. The self-consistent rate equations model [45] has been used extensively to study the influence of external parameters (e.g., doping density) on the QCL devices performance [46, 52] and provide insight in improving QCL designs [53–55], but this model does not account for the electron dynamics in the plane parallel to the layers, which has been shown critical in determining the actual transport properties in mid-IR QCLs [49].

Ensemble Monte Carlo (EMC)[56] method is a powerful technique for the numerical solution of the kinetic Boltzmann-like transport equation that governs the incoherent transport in QCLs [41]. One of the main advantages of the ensemble Monte Carlo approach is that it allows one to include, on an equal footing, a large variety of scattering mechanisms on the microscopic level, and the in-plane electron dynamics is automatically taken into account. The computational time of this approach is longer than that of the rate equations model, but still takes much less time than the NEGF formalism, so it can produce useful results promptly for a QCL design. Furthermore, this approach is very versatile and robust: once

X. Gao, D. Botez, and I. Knezevic, "Multivalley simulation and design of quantum cascade lasers,"
in Encyclopedia of Nanoscience and Nanotechnology, Edited by H. S. Nalwa, American Scientific Publishers, in press. (2008)

the simulator has been developed, it can easily be adapted to simulate transport properties of different QCL structures.

C. Issues in GaAs-based QCLs

Although mid-IR GaAs QCLs have achieved dramatic progress in the past few years, these devices have not achieved CW operation at room temperature. Several issues have limited their device performance; in this chapter we will focus on investigating the following four:

(1) Carrier leakage

The relatively large threshold current density ($J_{\rm th}$) and power consumption [22] of these QCLs have made it very challenging to achieve room temperature CW operation. The high value of $J_{\rm th}$ primarily arises from the high leakage, including the leakage to the continuum [57] and to the satellite valley (X-valley) [58, 59]. To further improve the performance of GaAs/AlGaAs QCLs, a detailed knowledge of possible current leakage paths and carrier loss in particular designs is highly desirable. Although the leakage via the continuum states has been well recognized [22, 31] and studied [60], satellite-valley leakage was not systematically investigated in theory until recently [58, 59]. Properly quantifying both the continuum leakage and the intervalley leakage in GaAs/AlGaAs QCL structures is an essential step towards the improvement of existing designs.

(2) Electron heating

The challenge for GaAs QCLs to operate in CW regime at RT is in part coming from the enormous internal (electron and lattice) heating at high heatsink temperatures [61]. The electron heating is caused by the high input power density and the low power conversion efficiency: the electron system is not able to dissipate (via optical-phonon emission) the relatively large amount of energy provided by the applied bias. The excessive input power heats up the electron system first, and ultimately the whole device through multiple-phonon emission processes. It is important to characterize the degree of electron heating in a given design.

(3) Short wavelength limit

The emission wavelength of mid-IR GaAs/AlGaAs QCLs incorporating a single injection barrier has been limited to above 8 μm due to the intervalley Γ-X electron transfer [39].

X. Gao, D. Botez, and I. Knezevic, "Multivalley simulation and design of quantum cascade lasers,"
in Encyclopedia of Nanoscience and Nanotechnology, Edited by H. S. Nalwa, American Scientific Publishers, in press. (2008)

By utilizing a double injection barrier [39] or by depositing InAs monolayers in the wide active wells [25], the emission wavelength is reduced from 8 μm to 7.3 μm for the former case, and from 9.4 μm to 7.4 μm for the latter case, but the lasing was observed only below cryogenic temperature in pulsed mode for both cases. A novel GaAs-based QCL design is needed to achieve room-temperature emission wavelength below 7 μm. A rigorous theoretical simulator is necessary to characterize transport properties of the novel design and optimize it for high-performance operation.

(4) Phonon confinement

QCLs are multiple-quantum-well heterostructures, spatially confined along the grown direction. Transport simulation of QCLs generally neglects the influence of spatial confinement on the phonon spectra, and assumes that phonons behave the same as in bulk semiconductors. It has long been unclear whether the spatial confinement of phonons has a strong effect on the electron transport properties of cascaded structures. There has so far been no systematic account of the phonon confinement on the transport properties of GaAs-based QCLs, such as the current-field characteristics or population inversion.

D. What This Chapter Covers

In this chapter, we show how the use of a multivalley Monte Carlo simulation (MMC) can help address and overcome problematic issues arising in the design of QCLs. This microscopic simulation can help us better understand the physics of the laser operation and pinpoint the fundamental physical limitations. Moreover, computational optimization of a laser design is much cheaper than experimental trial-and-error, and a detailed microscopic simulation such as MMC can help identify the culprits in a particular design that lead to leakage or excessive heating ahead of time, so that time and resources spent on fabrication are minimized.

Section II describes in detail the theory behind the EMC QCL simulator [58, 59]. First, the Boltzmann-like transport model for mid-IR QCL structures including both the Γ- and X-valley transport is presented. The charge-conserving scheme is introduced and it enables one to simulate the transport in QCLs by solving the Boltzmann-like kinetic equations over two adjacent stages. The ensemble Monte Carlo procedure for simulating QCL structures is briefly described and the corresponding flow chart is given. Details of solving the Γ- and X-

X. Gao, D. Botez, and I. Knezevic, "Multivalley simulation and design of quantum cascade lasers,"
in Encyclopedia of Nanoscience and Nanotechnology, Edited by H. S. Nalwa, American Scientific Publishers, in press. (2008)

valley electronic states are then presented. Effects of the electrostatic potential on subband energy levels and wavefunctions are studied by self-consistently solving the Schrödinger-Poisson equations. All the relevant scattering rates are evaluated in detail. The interaction mechanisms included are electron-longitudinal polar optical (electron-LO) phonon, electron-electron, and intervalley scattering processes within the same stage and between adjacent stages.

In Section III, the Monte Carlo simulator described in Section II is used to simulate the transport properties of two well-known equivalent-design GaAs/AlGaAs mid-IR QCLs [28, 31]. The relevant Γ- and X-subband energy levels and wavefunctions for the two lasers are first illustrated and the difference in wavefunctions between the two QCLs is pointed out. The field versus current density characteristics at different temperatures for the two QCLs are analyzed, together with the field dependence of the Γ- and X-valley electron density. The analysis leads to identification of the dominant X-valley leakage path. The effects of the X-valley leakage on the two QCLs are investigated and compared. In addition, the effect of the electron-electron interaction and electron heating are investigated and discussed.

Section IV presents the simulation and optimization of three deep-active-well QCLs, emitting at 6.7 μm, based on the strain-compensated $In_{0.1}Ga_{0.9}As/GaAs/Al_{0.45}Ga_{0.55}As$ heterostructure grown on GaAs substrates. Simulation results of the first structure reveal that this laser is incapable of lasing emission at room temperature. To achieve room-temperature emission, an improved design was proposed, which has enough gain to allow room-temperature lasing, but cannot lase at cryogenic temperature. Simulation results from the two structures directly help to obtain a third optimized structure. The optimization of the third structure is explained and its device performance is compared to that of the state-of-the-art GaAs QCL.

Section V fully incorporates the phonon confinement in the multivalley Monte Carlo simulator and investigates its effects in detail. Details of the phonon spectra and potentials calculation due to spatial confinement are presented using the transfer matrix method with periodic boundary conditions, and they are followed with calculation of the phonon potential normalization coefficients. The scattering rates of all the Γ- and X-valley electron states of interest by all the phonon modes are then computed and included in the multivalley simulator. The effects of phonon confinement on the transport properties of GaAs QCLs are investigated.

X. Gao, D. Botez, and I. Knezevic, "Multivalley simulation and design of quantum cascade lasers,"
in Encyclopedia of Nanoscience and Nanotechnology, Edited by H. S. Nalwa, American Scientific Publishers, in press. (2008)

II. THEORETICAL APPROACH

A. Boltzmann-Like Transport Equation for QCLs

It has been shown [41, 49] that the stationary charge transport in mid-IR QCL heterostructures is incoherent in nature, and can therefore be described by a Boltzmann-like transport equation. These structures are normally grown along the (001) direction, defined as a z-axis, with the x-y plane parallel to the layers. Since the GaAs/AlGaAs QCL heterostructure is the main focus in this work, both Γ and the three X valleys are important in determining the transport properties. Electronic states near the minima of the Γ and X valleys are characterized by $|\mathbf{k}\alpha\rangle = |\mathbf{k}, \nu\lambda\eta\rangle$, where $\mathbf{k} = (k_x, k_y)$ is the wave vector in the x-y plane, ν is the subband index, λ denotes the stage, and η is the valley index ($\eta = \Gamma, \mathrm{X}_x, \mathrm{X}_y, \mathrm{X}_z$). The electron distribution function $f_{\mathbf{k}\alpha}(t)$, measuring the probability that an electron resides in a state $|\mathbf{k}\alpha\rangle$ at time t, evolves with time according to the Boltzmann-like transport equation [41]

$$\frac{d}{dt} f_{\mathbf{k}\alpha}(t) = \sum_{\mathbf{k}'\alpha'} \left\{ S^{\alpha}_{\alpha'}(\mathbf{k}', \mathbf{k}) f_{\mathbf{k}'\alpha'}(t) \left[1 - f_{\mathbf{k}\alpha}(t)\right] - S^{\alpha'}_{\alpha}(\mathbf{k}, \mathbf{k}') f_{\mathbf{k}\alpha}(t) \left[1 - f_{\mathbf{k}'\alpha'}(t)\right] \right\}, \qquad (1)$$

where $S^{\alpha'}_{\alpha}(\mathbf{k}, \mathbf{k}')$ is the total transition rate from state $|\mathbf{k}\alpha\rangle$ to $|\mathbf{k}'\alpha'\rangle$, and $S^{\alpha'}_{\alpha} = \sum_s S^{\alpha'}_{\alpha,s}$, is the sum over all possible scattering mechanisms s. Compared to the standard Boltzmann transport equation (BTE) [62], Eq. (1) does not have the in-plane drift and diffusion terms on the left hand side, since there is no electric field applied in the x-y plane, and the plane is large enough to be regarded as having uniform distribution in real space. The electric field applied along z does not explicitly accelerate electrons, but through modifying the Γ and X band profiles, affects the electronic states and therefore indirectly changes the electron distribution. The motion of electrons along z is purely hopping among subbands due to scattering.

The translational symmetry of QCL structures (i.e., the wavefunctions in any two stages are simple translations in space and energy) allows for simulating electron transport over a generic central stage λ only. Spatially remote stages have little wavefunction overlap with the central stage, making it sufficient to limit the interstage scattering ($\lambda' \neq \lambda$) to the nearest neighbors ($\lambda' = \lambda \pm 1$). A schematic of three adjacent stages under bias is shown in Fig.2.

X. Gao, D. Botez, and I. Knezevic, "Multivalley simulation and design of quantum cascade lasers,"
in Encyclopedia of Nanoscience and Nanotechnology, Edited by H. S. Nalwa, American Scientific Publishers, in press. (2008)

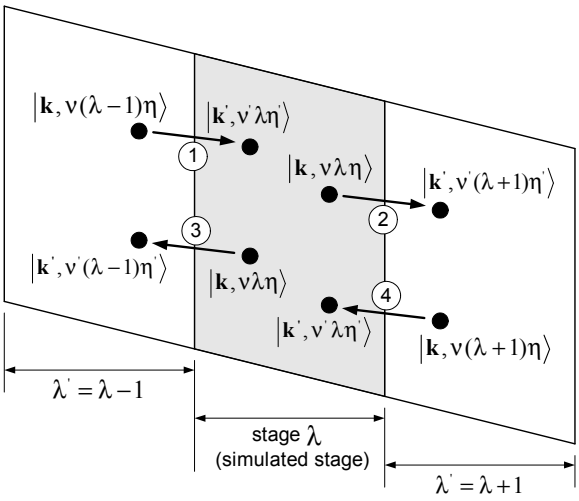

FIG. 2. Schematic of three adjacent stages under an applied field. Reprinted with permission from [59], X. Gao, D. Botez, and I. Knezevic, *J. Appl. Phys.* 101, 063101 (2007). © 2007, American Institute of Physics.

In addition, periodicity of the structures ensures the validity of the charge-conserving scheme [41] employed in our EMC simulation: each time an electron in a state $|\mathbf{k},\nu\lambda\eta\rangle$ undergoes an interstage scattering process to a new state $|\mathbf{k}',\nu'(\lambda\pm1)\eta'\rangle$ (e.g., processes ② and ③ in Fig. 2), another electron is properly injected into the central region by the corresponding processes ① and ④, so that the number of electrons in the simulated stage λ is conserved. Furthermore, the transition rates for processes ② and ③ can be regarded as the same as those of processes ① and ④, respectively, thanks to the translational symmetry. As a benefit of this equivalence, it is only necessary to solve for energy levels and wavefunctions in two full adjacent stages (e.g., stages λ and $\lambda+1$) to compute all the *intrastage* ($\lambda'=\lambda$) and nearest-neighbor *interstage* ($\lambda'=\lambda\pm1$) transition rates.

The current density J across the whole device is defined in terms of the net electron flux through the interface between the simulated stage λ and the next stage $\lambda+1$,

$$J \propto \sum_{\mathbf{k}\nu\eta}\sum_{\mathbf{k}'\nu'\eta'}\left[S^{\nu'(\lambda+1)\eta'}_{\nu\lambda\eta}(\mathbf{k},\mathbf{k}')f_{\nu\lambda\eta}(\mathbf{k}) - S^{\nu'\lambda\eta'}_{\nu(\lambda+1)\eta}(\mathbf{k},\mathbf{k}')f_{\nu(\lambda+1)\eta}(\mathbf{k})\right]. \tag{2}$$

In the EMC implementation, J is calculated by counting the interstage scattering events. Details of obtaining the energy levels and wavefunctions in stages λ and $\lambda+1$ are described in Sec. II.

X. Gao, D. Botez, and I. Knezevic, "Multivalley simulation and design of quantum cascade lasers,"
in Encyclopedia of Nanoscience and Nanotechnology, Edited by H. S. Nalwa, American Scientific Publishers, in press. (2008)

1. *Ensemble Monte Carlo Method*

The ensemble Monte Carlo (EMC) method [56] is an efficient approach for solving the Boltzmann-like equation Eq. (1) using random numbers. (Details for implementing an EMC simulation of bulk semiconductors or devices can be found in Refs. [56, 62, 63].) The EMC method is based on calculating the motion of an ensemble of particles during a short time dt. It can be applied to analyze the transient as well as steady-state electron transport in unipolar devices. Figure 3 shows the flight dynamics of an EMC calculation. The horizontal lines show the trajectories of particles 1 through N along the time axis. Each star-like symbol on the horizontal line represents a scattering event, where an electron is scattered by a phonon or another electron. Between two consecutive scattering events, an electron flies freely in the x-y plane (no external field is applied in the x-y plane). Random numbers are used to determine the time between two consecutive scattering events (also called the free-flight time), and to choose the proper scattering process among many scattering mechanisms. The vertical dotted lines indicate the sampling times, spaced by dt, at which the electron distribution function f is evaluated from the ensemble. Macroscopic quantities of interest (e.g., electron density, current density) can be readily evaluated from the distribution f. The time interval dt should be chosen small enough (typically 1 femtosecond) to capture the right electron dynamics.

Figure 4 shows a flow chart of the ensemble Monte Carlo transport kernel for QCL structures. Between scattering events, particles fly freely in the plane parallel to the layers (x-y plane) and remain in a given subband in the z-direction. Positions of electrons in the x-y plane are not tracked due to translational symmetry (the structure is considered unbound in the x-y plane), and the electron transport in QCL structures is essentially vertical (scattering between subbands determines the transport). Input of the Monte Carlo transport kernel is provided by a self-consistent Schrödinger-Poisson solver, as depicted in Fig. 5, which solves for the electronic states in the conduction band of a QCL structure. It was found that the Poisson solver has a negligible effect on the electronic states for typical doping densities ($\leq 4 \times 10^{11}$ cm^{-2}) in QCLs, as investigated in Sec. II C, so in order to reduce the computation time, the electron states from the Schrödinger solver within the linear potential drop approximation were directly used to compute the scattering rates in

X. Gao, D. Botez, and I. Knezevic, "Multivalley simulation and design of quantum cascade lasers,"
in Encyclopedia of Nanoscience and Nanotechnology, Edited by H. S. Nalwa, American Scientific Publishers, in press. (2008)

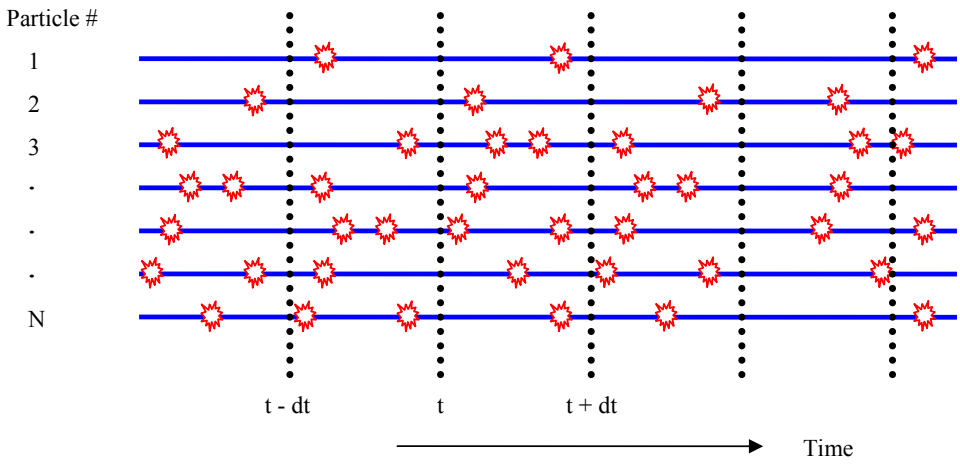

FIG. 3. Flight dynamics of the ensemble Monte Carlo method. The horizontal lines show the trajectories of particles 1 through N along the time axis, and each star-like symbol on the horizontal line represents a scattering event. The vertical dotted lines indicate the sampling times, spaced by dt, at which the electron distribution function f is evaluated from the ensemble.

the transport kernel. Output from the transport kernel includes the current density J, subband electron density n_i, population inversion Δn, optical modal gain G_m, and electron temperature T_e.

X. Gao, D. Botez, and I. Knezevic, "Multivalley simulation and design of quantum cascade lasers,"
in Encyclopedia of Nanoscience and Nanotechnology, Edited by H. S. Nalwa, American Scientific Publishers, in press. (2008)

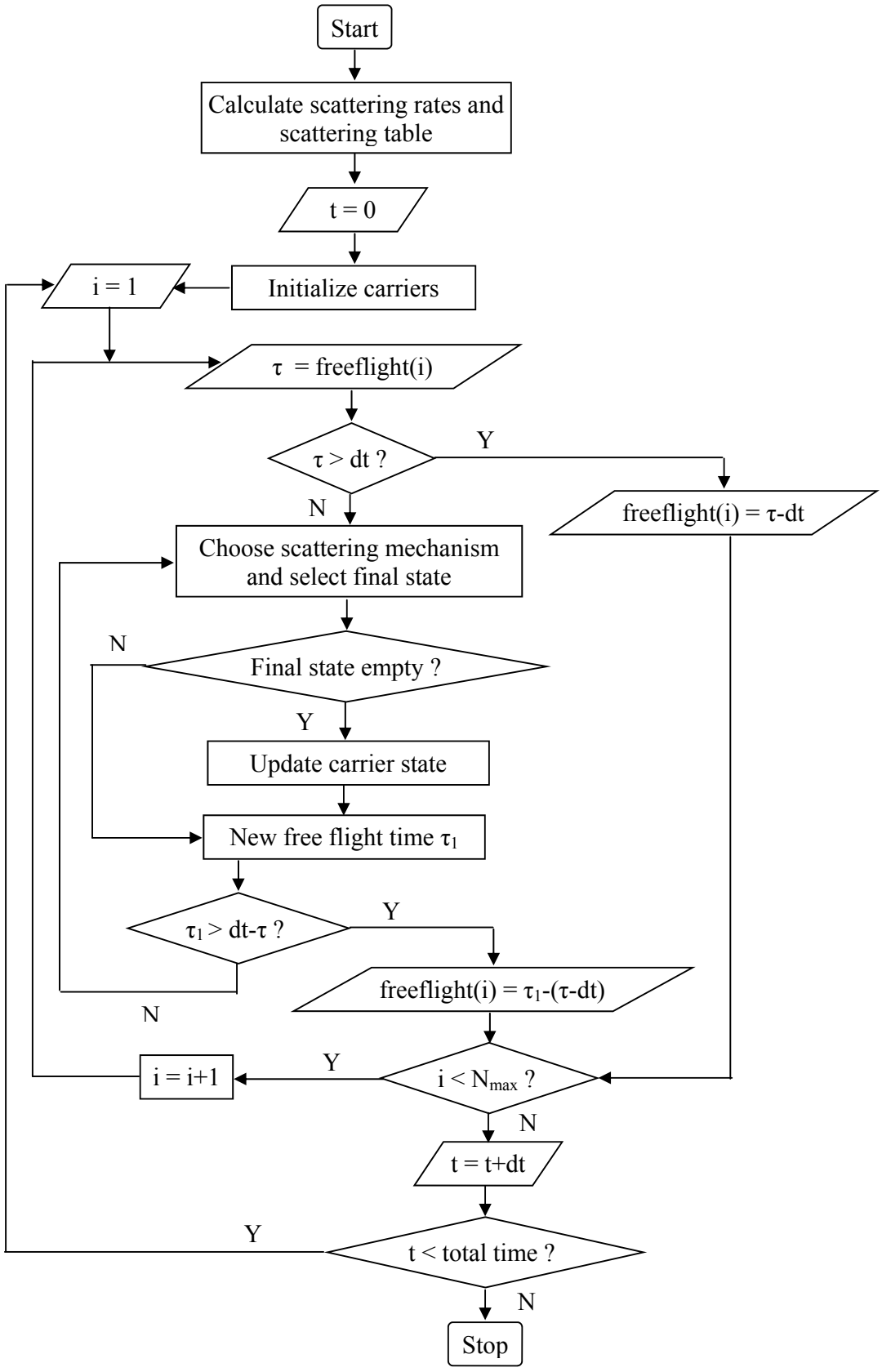

FIG. 4. Flowchart of the ensemble Monte Carlo transport kernel for QCL structures.

X. Gao, D. Botez, and I. Knezevic, "Multivalley simulation and design of quantum cascade lasers,"
in Encyclopedia of Nanoscience and Nanotechnology, Edited by H. S. Nalwa, American Scientific Publishers, in press. (2008)

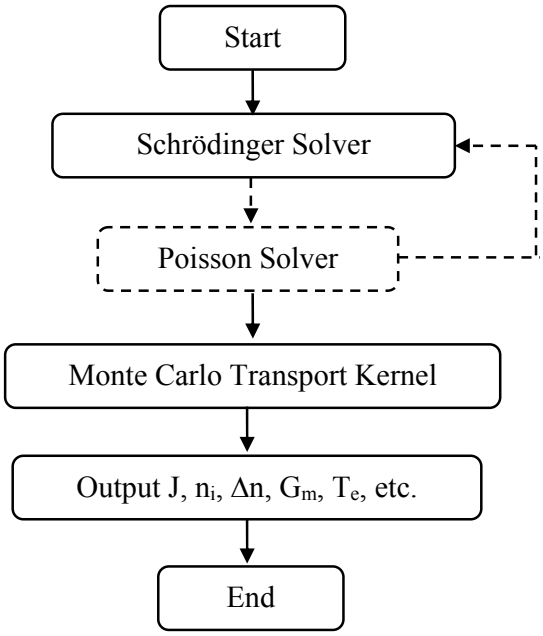

FIG. 5. Flowchart of an EMC simulation for QCL structures.

B. Electronic States

1. Γ-valley electronic states

In most literature on QCL modeling, Γ-valley electronic states are obtained using the conduction-band effective mass equation, whereas this work employs the $\mathbf{k}\cdot\mathbf{p}$ method to obtain the Γ-states. The $\mathbf{k}\cdot\mathbf{p}$ method provides a good way of solving the electronic band structure near the band edges, where most of the interesting physical phenomena occur in optical devices. It can conveniently account for the lattice-mismatch strain effect, and the influence of valence bands in narrow-gap semiconductor materials [64].

The standard eight-band $\mathbf{k}\cdot\mathbf{p}$ model [65, 66] consists of the conduction band (c), heavy-hole (hh), light hole (lh), and the spin-orbit split-off (so) band, all with their spin degeneracies. The Hamiltonian matrix can be found for unstrained [65] and lattice-mismatched biaxially strained [66] bulk semiconductors without external perturbation. With the in-plane wave vector $\mathbf{k} = 0$ and the remaining spin degeneracy, the eight-band $\mathbf{k}\cdot\mathbf{p}$ model [66] reduces to a three-band problem, with the hh band factoring out. The reduced 3×3 matrix takes

X. Gao, D. Botez, and I. Knezevic, "Multivalley simulation and design of quantum cascade lasers,"
in Encyclopedia of Nanoscience and Nanotechnology, Edited by H. S. Nalwa, American Scientific Publishers, in press. (2008)

the form

$$H_{3\times3} = \begin{bmatrix} E_{\rm c} + (1+2F_K)E_z + A_\epsilon & \sqrt{\frac{2}{3}E_P E_z} & \sqrt{\frac{1}{3}E_P E_z} \\ \sqrt{\frac{2}{3}E_P E_z} & E_{\rm v} - (\gamma_1+2\gamma_2)E_z - P_\epsilon + Q_\epsilon & -2\sqrt{2}\gamma_2 E_z + \sqrt{2}Q_\epsilon \\ \sqrt{\frac{1}{3}E_P E_z} & -2\sqrt{2}\gamma_2 E_z + \sqrt{2}Q_\epsilon & E_{\rm v} - \Delta_{\rm so} - \gamma_1 E_z - P_\epsilon \end{bmatrix}, \tag{3}$$

where

$$\begin{aligned} E_z &= \frac{\hbar^2 k_z^2}{2m_0}, \\ E_P &= \frac{2m_0}{\hbar^2} P_{\rm cv}^2, \\ P_{\rm cv} &= \frac{\hbar}{m_0}\langle iS\,|p_x|\,X\rangle, \\ \gamma_1 &= \gamma_1^L - \frac{E_P}{3E_g}, \\ \gamma_2 &= \gamma_2^L - \frac{E_P}{6E_g}, \\ A_\epsilon &= a_{\rm c}(\epsilon_{xx}+\epsilon_{yy}+\epsilon_{zz}), \\ P_\epsilon &= -a_{\rm v}(\epsilon_{xx}+\epsilon_{yy}+\epsilon_{zz}), \\ Q_\epsilon &= -\frac{b}{2}(\epsilon_{xx}+\epsilon_{yy}-2\epsilon_{zz}). \end{aligned} \tag{4}$$

$E_{\rm c}$ and $E_{\rm v}$ are the unstrained conduction- and valence-band edges, respectively, relative to a common reference energy. $\Delta_{\rm so}$ is the spin-orbit split-off energy. γ_1 and γ_2 are the modified Luttinger parameters [67], and γ_1^L and γ_2^L are the standard Luttinger parameters [68]. The explicit inclusion of the interaction between the valence and conduction bands in the $\mathbf{k}\cdot\mathbf{p}$ model leads to the modified Luttinger parameters discussed by Pidgeon and Brown [67]. F_K [69] represents the contribution of higher conduction bands to the effective mass of the Γ_6 conduction-band electrons. $P_{\rm cv}$ is the interband momentum matrix element defined by Kane [69], and E_P is the energy parameter for $P_{\rm cv}$. $a_{\rm c}$, $a_{\rm v}$, and b are the Bir-Pikus deformation potentials [70], with the sign conventions being negative, positive, and negative, respectively.

For a strained semiconductor layer pseudomorphically grown on a (001)-oriented (z axis) substrate, the strain tensor components are [64]

$$\begin{aligned} \epsilon_{xx} &= \epsilon_{yy} = \frac{a_0 - a}{a}, \\ \epsilon_{zz} &= -\frac{2c_{12}}{c_{11}}\epsilon_{xx}, \\ \epsilon_{xy} &= \epsilon_{yz} = \epsilon_{zx} = 0, \end{aligned} \tag{5}$$

X. Gao, D. Botez, and I. Knezevic, "Multivalley simulation and design of quantum cascade lasers,"
in Encyclopedia of Nanoscience and Nanotechnology, Edited by H. S. Nalwa, American Scientific Publishers, in press. (2008)

where a_0 and a are the lattice constants of the substrate and the layer material, respectively, and c_{11} and c_{12} are the elastic stiffness constants of the strained layer. Therefore, A_ϵ, P_ϵ, and Q_ϵ are simplified to

$$\begin{aligned} A_\epsilon &= 2a_c\left(1-\frac{c_{12}}{c_{11}}\right)\epsilon_{xx}, \\ P_\epsilon &= -2a_v\left(1-\frac{c_{12}}{c_{11}}\right)\epsilon_{xx}, \\ Q_\epsilon &= -b\left(1+\frac{2c_{12}}{c_{11}}\right)\epsilon_{xx}. \end{aligned} \tag{6}$$

The material parameters for most III-V semiconductors are documented in Ref. [71].

Within the envelope function approximation (EFA) and the three-band $\mathbf{k}\cdot\mathbf{p}$ model, the full Γ-valley electron wavefunctions near the zone-center in each layer of a heterostructure can be written as [64, 65]

$$\Psi^\Gamma_{n,\mathbf{k}}(\mathbf{r},z) = \frac{1}{\sqrt{A}}e^{i\mathbf{k}\cdot\mathbf{r}}\sum_j \psi^\Gamma_{n,j}(z)u^\Gamma_{j\,0}(\mathbf{r},z), \tag{7}$$

where A is the normalization area, $\mathbf{r} = (x,y)$, j sums over the three bands (c, lh, so), and $\psi^\Gamma_{n,j}(z)$ is the normalized envelope function, slowly varying with coordinate z over the elementary cells of the crystalline lattice; the periodic Bloch function $u^\Gamma_{j\,0}(\mathbf{r},z)$ conserves its bulk properties within each layer except the small (1-2 monolayer wide) regions in the vicinity of the interfaces, and is assumed not to differ much from layer to layer. It should be noted that $|\mathbf{k}| \ll \pi/a$ in Eq. (7), with a being the monolayer thickness, because only the electron states near the minimum of the Γ valley are of interest in this work.

In the presence of an external potential, the envelope functions $\psi^\Gamma_{n,j}(z)$ satisfy the second-order differential equations [64, 65]

$$\sum_{j'}\left[H_{jj'}(\mathbf{k}=0,k_z) + U_\Gamma(z)\delta_{jj'}\right]\psi^\Gamma_{n,j'}(z) = E^\Gamma_n\psi^\Gamma_{n,j}(z), \tag{8}$$

where $H_{jj'}(\mathbf{k}=0,k_z)$ are the elements of the 3×3 $\mathbf{k}\cdot\mathbf{p}$ matrix in Eq. (3), and k_z will be replaced by the differential operator $-i\partial/\partial z$; $\delta_{jj'}$ is the Kronecker delta, and j' runs over the three bands (c, lh, so); the external potential $U_\Gamma(z) = -|e|F(z-d/2) - |e|\phi(z)$, where F is the applied uniform electric field, and $\phi(z)$ is the electrostatic potential owing to the specific distribution of free electrons from dopants in the system. ($\phi(z)$ is the correction to the approximation of linear potential drop, and it can be obtained from solving the Poisson

X. Gao, D. Botez, and I. Knezevic, "Multivalley simulation and design of quantum cascade lasers,"
in Encyclopedia of Nanoscience and Nanotechnology, Edited by H. S. Nalwa, American Scientific Publishers, in press. (2008)

equation.) The effects of $\phi(z)$ on the electronic states will be investigated in Sec. II C, and are disregarded in this section and Sec. II B 2. The band discontinuity at the interfaces is taken into account in $E_{\rm c}$ and $E_{\rm v}$ in the $H_{jj'}$ matrix.

The coupled differential Eqs. (8) may be solved by using the transfer matrix method [72], the finite difference method [73], or the finite element method [74]. However, all these real-space numerical methods would generate spurious solutions (i.e., solutions outside of the first reduced Brillouin zone (BZ) of the periodic structure) [75]. The reciprocal-space numerical technique [76, 77] ensures the wave vector k_z well within the first BZ to avoid spurious solutions, and is employed in our simulation. This approach relies on the periodicity of the QCL structure along the z direction. The envelope function $\psi^{\Gamma}_{n,j}(z)$ is expanded in a Fourier series [77]

$$\psi^{\Gamma}_{n,j}(z) = \sum_{m} a^{\Gamma,j}_{mn} e^{iG_m z}, \tag{9}$$

where d denotes the length of two stages, $G_m = 2m\pi/d$ ($m = 0, \pm1, \pm2, \cdots$) are the reciprocal vectors associated with the periodic heterostructure along the z-axis, and index m is an integer, $-N_G \le m \le N_G$ ($N_G = 50$ used), which runs over the number of Fourier components retained. Substituting this expression into Eq. (8), multiplying both sides by $e^{-iG_{m'}z}$, and integrating over d, one obtains an approximation to Eq. (8) as the eigenvalue problem

$$\sum_{j,m'}\sum_{j',m} a^{\Gamma,j'}_{mn}\frac{1}{d}\int_0^d {\rm d}z e^{i(G_m - G_{m'})z}\left[H_{jj'}(G_m, z) + U_{\Gamma}(z)\delta_{jj'}\right] = E^{\Gamma}_n a^{\Gamma,j}_{m'n}. \tag{10}$$

The matrix element $H_{jj'}(G_m, z)$ has the same form as Eq. (3) for each layer at position z, with k_z replaced by G_m. Eq. (10) is a standard eigenvalue problem for the coefficients $a^{\Gamma,j}_{m'n}$ with a super-matrix of size $3(2N_G{+}1) \times 3(2N_G{+}1)$. A diagonalization of this matrix then leads to $3(2N_G{+}1)$ eigenenergies E^{Γ}_n and the corresponding eigenvectors. The top $2N_G{+}1$ energy levels belong to the conduction subbands, and the associated eigenvectors construct the full subband wavefunctions. The remaining $2(2N_G{+}1)$ eigenenergies and eigenvectors characterize the valence subbands, which are not of interest in this work, since QCLs utilize electron transitions in the conduction band. As an example, Fig. 6 illustrates the energy levels and wavefunction moduli squared of ten Γ-valley subbands in two adjacent stages for the 45% Al QCL of Ref. [31] without $\phi(z)$ (linear potential drop only).

After obtaining $\psi^{\Gamma}_{n,j}(z)$, an average in-plane effective mass (to be used in the EMC cal-

X. Gao, D. Botez, and I. Knezevic, "Multivalley simulation and design of quantum cascade lasers,"
in Encyclopedia of Nanoscience and Nanotechnology, Edited by H. S. Nalwa, American Scientific Publishers, in press. (2008)

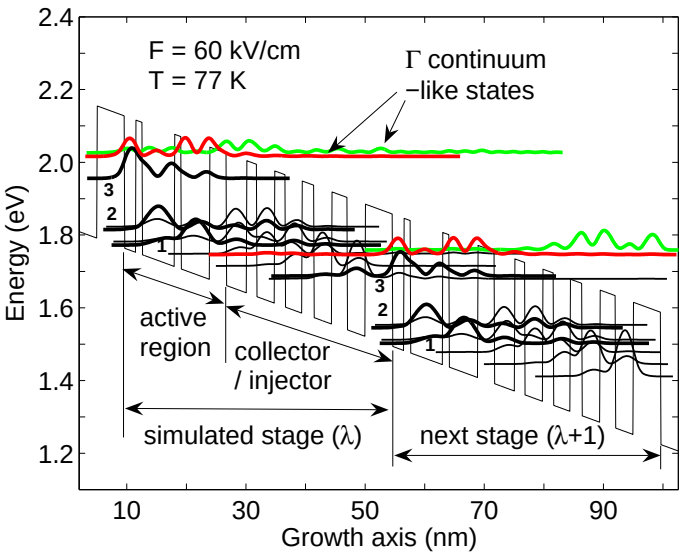

FIG. 6. Energy levels and wavefunction moduli squared of ten Γ-valley subbands in two adjacent stages for the 45% Al QCL of Ref. [31] within the linear potential drop approximation. The bold black curves denote the lasing levels (3-upper, 2-lower, 1-ground), while thin black curves are the injector states. The red and green curves indicate the Γ continuum-like states.

culation) is calculated for each Γ-conduction subband n as

$$\frac{1}{m_n^*} = \sum_j \int_0^d \mathrm{d}z \frac{\left|\psi_{n,j}^{\Gamma}(z)\right|^2}{m^*(j,z)}, \tag{11}$$

where $m^*(j,z)$ is the effective mass of band j of the material at position z. Based on the new electron effective mass, the in-plane energy dispersion is regarded as parabolic: $E_{n,\mathbf{k}}^{\Gamma} = E_n^{\Gamma} + \hbar^2\mathbf{k}^2/2m_n^*$.

2. X-valley electronic states

There are two groups of X valleys in (001)-grown QCL structures: the X_z valley along the axis z, and two side valleys $\mathrm{X}_x, \mathrm{X}_y$ oriented along the x and y directions, respectively. The X_x and X_y valleys are equivalent within the effective mass framework, and are regarded as one doubly-degenerate X_x valley.

In the EFA, near the X valley minima, the electron wavefunctions $\Psi_{n,\mathbf{k}}^{\mathrm{X}_x}(\mathbf{r},z)$ and $\Psi_{n,\mathbf{k}}^{\mathrm{X}_z}(\mathbf{r},z)$

X. Gao, D. Botez, and I. Knezevic, "Multivalley simulation and design of quantum cascade lasers,"
in Encyclopedia of Nanoscience and Nanotechnology, Edited by H. S. Nalwa, American Scientific Publishers, in press. (2008)

can be expressed by

$$\Psi^{\mathrm{X}_x}_{n,\mathbf{k}}(\mathbf{r},z) = \frac{1}{\sqrt{A}} e^{i\left(\mathbf{k}\cdot\mathbf{r}+\frac{\pi}{a}x\right)} \psi^{\mathrm{X}_x}_n(z) u^{\mathrm{X}_x}(\mathbf{r},z), \tag{12a}$$

$$\Psi^{\mathrm{X}_z}_{n,\mathbf{k}}(\mathbf{r},z) = \frac{1}{\sqrt{A}} e^{i\mathbf{k}\cdot\mathbf{r}} \psi^{\mathrm{X}_z}_n(z) u^{\mathrm{X}_z}(\mathbf{r},z), \tag{12b}$$

where $\psi^{\ell}_n(z)$ ($\ell = \mathrm{X}_x, \mathrm{X}_z$) are the envelope functions along z, $u^{\ell}(\mathbf{r},z)$ are the Bloch functions, and a is the monolayer width.

To solve for $\psi^{\ell}_n(z)$, the effective-mass equations are sufficient, since the X valleys are well above the valence bands and the effect of the valence bands on the electronic states is negligible. $\psi^{\mathrm{X}_x}_n(z)$ and $\psi^{\mathrm{X}_z}_n(z)$ in each layer satisfy the effective-mass Eqs. (13a) and (13b), respectively.

$$\left[\frac{-\hbar^2}{2m^*_t(z)}\frac{\mathrm{d}^2}{\mathrm{d}z^2} + U_{\mathrm{X}}(z)\right] \psi^{\mathrm{X}_x}_n(z) = E^{\mathrm{X}_x}_n \psi^{\mathrm{X}_x}_n(z), \tag{13a}$$

$$\left[\frac{-\hbar^2}{2m^*_l(z)}\frac{\mathrm{d}^2}{\mathrm{d}z^2} + U_{\mathrm{X}}(z)\right] \psi^{\mathrm{X}_z}_n(z) = E^{\mathrm{X}_z}_n \psi^{\mathrm{X}_z}_n(z), \tag{13b}$$

where $m^*_t(z)$ and $m^*_l(z)$ are the corresponding transverse and longitudinal X-valley electron effective mass; $U_{\mathrm{X}}(z) = E_{\mathrm{X}}(z) - |e|F(z-d/2)$ is the external potential, where $E_{\mathrm{X}}(z)$ contains the X-valley conduction-band offset relative to a common energy reference level.

In the reciprocal-space approach [77], following a similar procedure as described for the Γ-subband envelope function $\psi^{\Gamma}_{n,j}(z)$, Eqs. (9) and (10), one obtains the eigenvalue problem

$$\sum_{m',m} a^{\mathrm{X}_x}_{mn} \frac{1}{d} \int_0^d \mathrm{d}z e^{i(G_m - G_{m'})z} \left[\frac{\hbar^2 G^2_m}{2m^*_t(z)} + U_{\mathrm{X}}(z)\right] = E^{\mathrm{X}_x}_n a^{\mathrm{X}_x}_{m'n}, \tag{14}$$

for the Fourier coefficients $a^{\mathrm{X}_x}_{mn}$. The eigenvalue problem for $a^{\mathrm{X}_z}_{mn}$ is similar to Eq. (14) with $m^*_t(z)$ replaced by $m^*_l(z)$. Solutions to the eigenvalue problems provide $2N_G+1$ energy levels and the corresponding eigenvectors for the X_x (X_z) subbands, where X_x subbands are doubly-degenerate. Figures 7 and 8 show the energy levels and wavefunction moduli squared of the X_x- and X_z-subbands, respectively, in two adjacent stages for the 45% Al QCL [31], without $\phi(z)$ (linear potential drop only).

With the envelope function $\psi^{\ell}_n(z)$, one can compute the average in-plane longitudinal ($m^{\ell *}_{ln}$) and transverse ($m^{\ell *}_{tn}$) electron effective mass for each X-subband n,

$$\frac{1}{m^{\ell^*}_{in}} = \int_0^d \mathrm{d}z \frac{\left|\psi^{\ell}_n(z)\right|^2}{m^*_i(z)}, \quad i = l, t. \tag{15}$$

X. Gao, D. Botez, and I. Knezevic, "Multivalley simulation and design of quantum cascade lasers,"
in Encyclopedia of Nanoscience and Nanotechnology, Edited by H. S. Nalwa, American Scientific Publishers, in press. (2008)

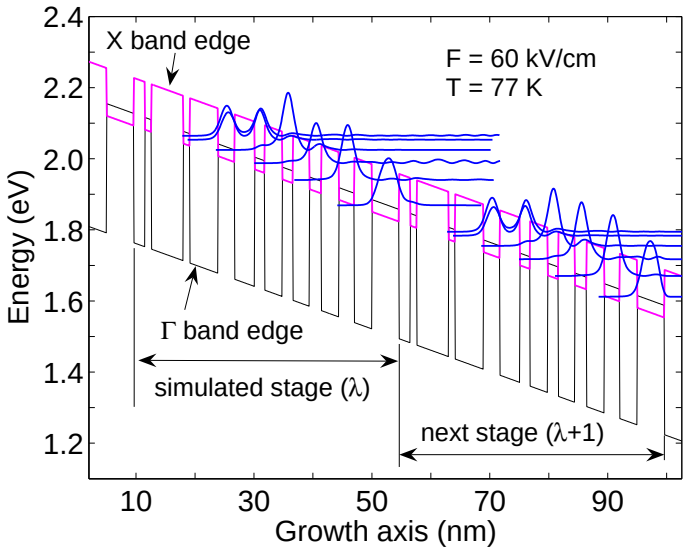

FIG. 7. Energy levels and wavefunction moduli squared of six X_x-subbands (doubly-degenerate) in two adjacent stages for the 45% Al QCL [31] within the linear potential drop approximation.

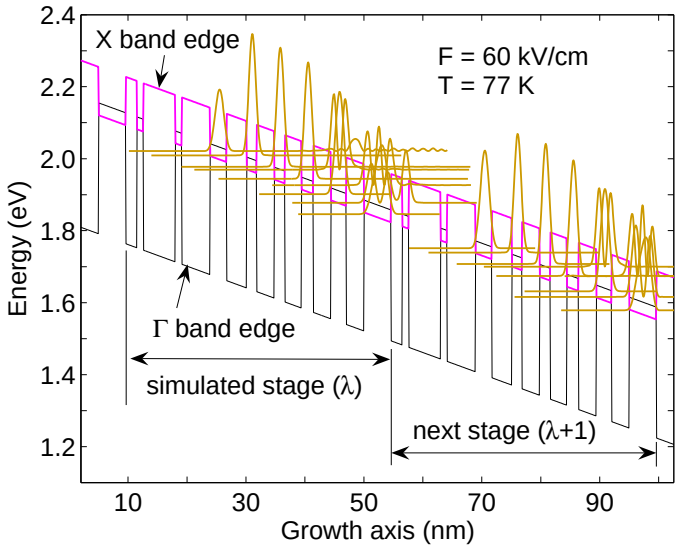

FIG. 8. Energy levels and wavefunction moduli squared of nine X_z-subbands in two adjacent stages for the 45% Al QCL [31] within the linear potential drop approximation.

For GaAs, X-valley effective masses are $m_l^* = 1.3$ and $m_t^* = 0.23$, while for AlAs, $m_l^* = 0.97$ and $m_t^* = 0.22$. A parabolic in-plane dispersion relation is assumed, with the averaged

X. Gao, D. Botez, and I. Knezevic, "Multivalley simulation and design of quantum cascade lasers,"
in Encyclopedia of Nanoscience and Nanotechnology, Edited by H. S. Nalwa, American Scientific Publishers, in press. (2008)

effective mass:

$$E^{\mathrm{X}_x}_{n,\mathbf{k}} = E^{\mathrm{X}_x}_n + \frac{\hbar^2\mathbf{k}^2}{2\sqrt{m^*_{ln}m^*_{tn}}}, \tag{16a}$$

$$E^{\mathrm{X}_z}_{n,\mathbf{k}} = E^{\mathrm{X}_z}_n + \frac{\hbar^2\mathbf{k}^2}{2m^*_{tn}}. \tag{16b}$$

The above wavefunctions $\Psi^{\eta}_{n,\mathbf{k}}$ and energy dispersions $E^{\eta}_{n,\mathbf{k}}$ ($\eta = \Gamma, \mathrm{X}_x, \mathrm{X}_z$) are obtained by treating two adjacent stages as one period. They need to be properly assigned to each stage according to the localization of wavefunctions. Then the lowest N_η conduction subbands in each stage are selected for transport simulation. N_η values depend on the QCL structure and applied field, and is significantly smaller than the actually obtained levels ($2N_G + 1$ or so). One can relabel the chosen electronic states in stage λ as $|\mathbf{k}, \nu\lambda\eta\rangle$ (νth subband, λth stage, and ηth valley), the associated effective mass as $m^{\eta*}_{\nu\lambda}$, and the energy dispersion $E^{\eta}_{\nu\lambda}(\mathbf{k})$, which satisfies the following relation

$$E^{\eta}_{\nu\lambda}(\mathbf{k}) = \frac{\hbar^2\mathbf{k}^2}{2m^{\eta*}_{\nu\lambda}} + E^{\eta}_{\nu\lambda}. \tag{17}$$

The states $|\mathbf{k}, \nu\lambda\eta\rangle$ are rewritten in the form

$$|\mathbf{k}, \nu\lambda\Gamma\rangle = \frac{1}{\sqrt{A}} e^{i\mathbf{k}\cdot\mathbf{r}} \sum_j \psi^{\Gamma}_{j,\nu\lambda}(z) u^{\Gamma}_{j0}(\mathbf{r}, z), \tag{18a}$$

$$|\mathbf{k}, \nu\lambda\mathrm{X}_x\rangle = \frac{1}{\sqrt{A}} e^{i\left(\mathbf{k}\cdot\mathbf{r} + \frac{\pi}{a}x\right)} \psi^{\mathrm{X}_x}_{\nu\lambda}(z) u^{\mathrm{X}_x}(\mathbf{r}, z), \tag{18b}$$

$$|\mathbf{k}, \nu\lambda\mathrm{X}_z\rangle = \frac{1}{\sqrt{A}} e^{i\mathbf{k}\cdot\mathbf{r}} \psi^{\mathrm{X}_z}_{\nu\lambda}(z) u^{\mathrm{X}_z}(\mathbf{r}, z). \tag{18c}$$

The subband index $\nu = 1, 2, \cdots, N_\eta$ for valley η. Similar notation is used for electronic states in stage λ+1.

C. Self-Consistent Schrödinger-Poisson Solver

The last two subsections have focused on solving the Schrödinger equations under the assumption that the electrostatic potential $\phi(z) = 0$ (potential drop is linear). This subsection accounts for $\phi(z)$, a correction to the linear potential drop which would imply charge neutrality everywhere, by solving the Schrödinger equations self-consistently with the Poisson equation. Also, we investigate the influence of $\phi(z)$ on the subband energies and wavefunctions, and explore the validity of disregarding $\phi(z)$ in the simulation to reduce the computational burden.

X. Gao, D. Botez, and I. Knezevic, "Multivalley simulation and design of quantum cascade lasers,"
in Encyclopedia of Nanoscience and Nanotechnology, Edited by H. S. Nalwa, American Scientific Publishers, in press. (2008)

$\phi(z)$ has the same profile in each stage due to the translational symmetry of QCL structures, and satisfies the one-dimensional Poisson equation

$$\frac{\partial}{\partial z}\left(\varepsilon_{\rm s}\frac{\partial\phi}{\partial z}\right) = -|e|\left[N_D^+(z) - n(z)\right], \tag{19}$$

where $\varepsilon_{\rm s}$ is the static dielectric permittivity. An effective constant value for $\varepsilon_{\rm s}$ is assumed throughout the heterostructure, which is a reasonable approximation for GaAs/AlGaAs systems. $N_D^+(z)$ and $n(z)$ are the ionized donor and electron concentrations, respectively, and the hole concentration $p(z)$ is neglected since QCL structures are n-type doped. Assuming conservation of charge in each stage (i.e., the charge-conserving scheme in Sec. II A), one can define a position-independent quasi-Fermi level E_F in each stage [44, 78]. The electron concentration $n(z)$ in stage λ is related to the electronic wavefunctions by

$$n(z) = \sum_{\nu=1}^{N_\Gamma}\sum_j \left|\psi^\Gamma_{j,\nu\lambda}(z)\right|^2 N^\Gamma_{\nu s} + \sum_\ell\sum_{\nu=1}^{N_\ell}\left|\psi^\ell_{\nu\lambda}(z)\right|^2 N^\ell_{\nu s}, \tag{20}$$

where the sum over j is over the three (c, lh, so) bands, ℓ sums over the X_x and X_z valleys, and $N^\eta_{\nu s}$ ($\eta = \Gamma,\ \mathrm{X}_x,\ \mathrm{X}_z$) is the sheet electron density in subband ν. $N^\eta_{\nu s}$ can be calculated as [64]

$$N^\eta_{\nu s} = \frac{2}{A}\sum_{\mathbf{k}}\frac{1}{1+\exp\left(\frac{E^\eta_{\nu\lambda}(\mathbf{k})-E_F}{k_BT}\right)}, \tag{21}$$

where the Fermi-Dirac distribution is used for the in-plane electron distribution in each subband, $E^\eta_{\nu\lambda}(\mathbf{k})$ is the electronic dispersion relation given by Eq. (17), and T is the lattice temperature. (The electron ensemble and the lattice are assumed to have the same temperature here.) Making use of the "sum-to-integral" rule

$$\frac{1}{A}\sum_{\mathbf{k}} = \frac{1}{(2\pi)^2}\int d^2\mathbf{k} = \int_0^\infty \frac{2\pi k dk}{(2\pi)^2}, \tag{22}$$

and the integral identity

$$\int\frac{dx}{1+e^x} = \int\frac{e^{-x}}{1+e^{-x}}dx = -\ln(1+e^{-x}), \tag{23}$$

the sheet electron density is obtained as

$$N^\eta_{\nu s} = \frac{k_BTm^{\eta*}_{\nu\lambda}}{\pi\hbar^2}\ln\left[1+\exp\left(\frac{E_F-E^\eta_{\nu\lambda}}{k_BT}\right)\right]. \tag{24}$$

X. Gao, D. Botez, and I. Knezevic, "Multivalley simulation and design of quantum cascade lasers,"
in Encyclopedia of Nanoscience and Nanotechnology, Edited by H. S. Nalwa, American Scientific Publishers, in press. (2008)

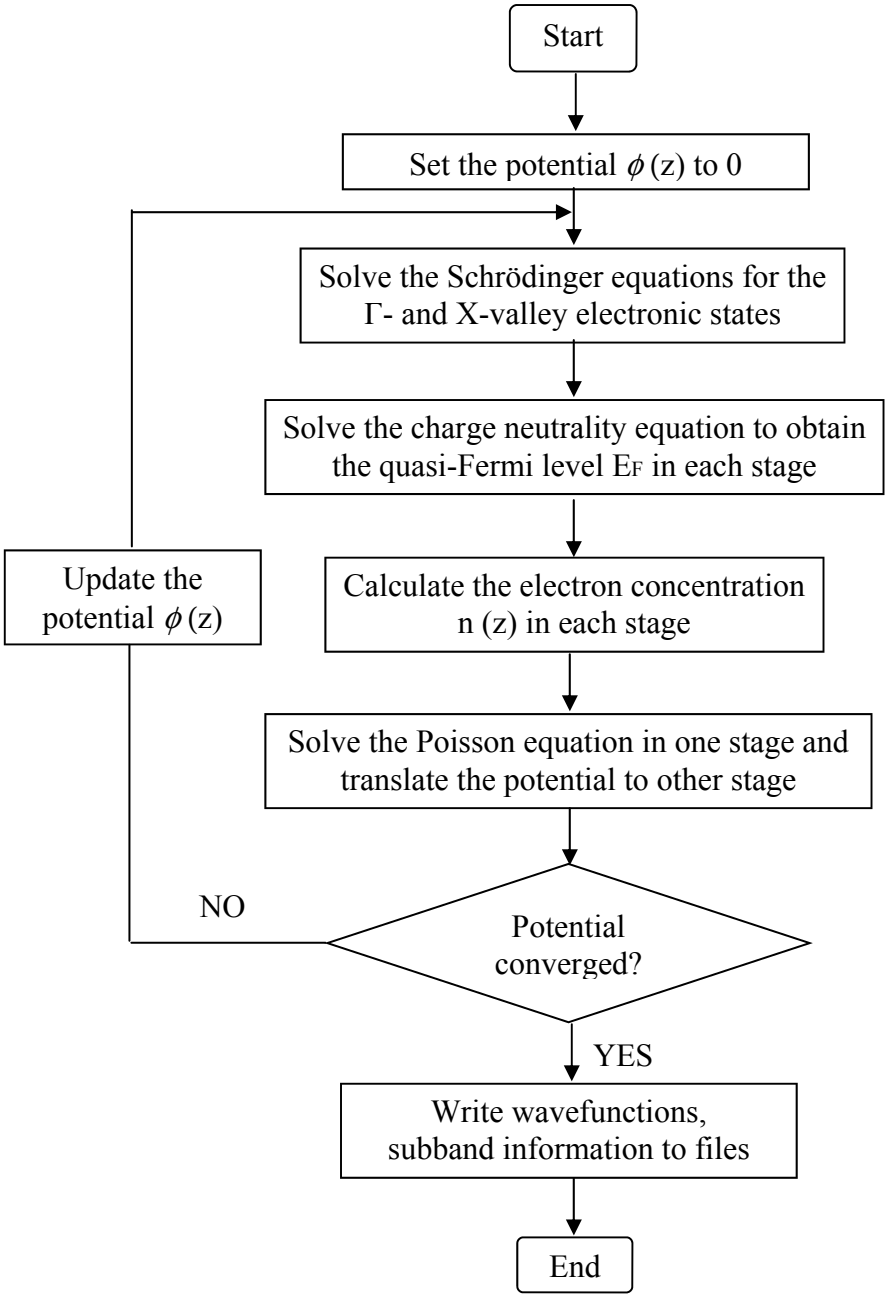

FIG. 9. Flow chart of a self-consistent Schrödinger-Poisson solver.

For $\eta = \mathrm{X}_x$, Eq. (24) needs to be multiplied by 2 to give $N_{\nu s}^{\mathrm{X}_x}$, since the X_x valley is doubly-degenerate. The sum of $N_{\nu s}^{\eta}$ in one stage (active region + injector) is equal to the total sheet electron density N_s from the charge neutrality condition [64, 78, 79]

$$N_s = \sum_{\eta} \sum_{\nu=1}^{N_\eta} N_{\nu s}^{\eta} = \int_{one\ stage} N_D^+(z) dz, \tag{25}$$

X. Gao, D. Botez, and I. Knezevic, "Multivalley simulation and design of quantum cascade lasers,"
in Encyclopedia of Nanoscience and Nanotechnology, Edited by H. S. Nalwa, American Scientific Publishers, in press. (2008)

where η sums over all valleys ($\eta = \Gamma,\ X_x,\ X_z$). For a given N_s, the quasi-Fermi level E_F is obtained by iteratively solving Eq. (25). When including $\phi(z)$ in Eqs. (8), (13a), and (13b), it is required to solve these equations self-consistently with Eqs. (19)-(20) and (24)-(25). The flow chart of a self-consistent calculation is given in Fig. 9.

The results from the self-consistent Schrödinger-Poisson solver in two adjacent stages for the 45% Al QCL [31] at F = 60 kV/cm and T = 77 K are presented in Figs. 10-11. Figure 10 shows the electrostatic potential energy profile $-|e|\phi(z)$ from the self-consistent Schrödinger-Poisson solver. The Poisson equation is solved using the total $n(z)$ in the stage defined by the red $\times$ marks with periodic boundary conditions, and then the potential is translated to the whole simulated region. For this particular example, the potential energy $-|e|\phi(z)$ has a peak-to-peak value of about 25 meV, but the external potential energy drop is $-|e|FL_p = 270$ meV ($L_p = 45$ nm, the length of one stage), the former being less than 10% of the applied potential energy drop. This small band bending owing to the specific electron distribution slightly changes the electronic structure (energies and wavefunctions), as shown in the right panel of Fig. 11. It is seen from Fig. 11 that Γ-subband wavefunctions remain nearly the same and the subband energy levels are modified within a few meVs when the band bending is included. This result holds true for all doping levels less than 4.0×10^{11} cm^{-2}, in agreement with the calculation in Ref. [46]. Thanks to the small effect of potential $\phi(z)$ on the electronic states, $\phi(z)$ is neglected due to low doping levels ($< 4 \times 10^{11}$ cm^{-2}) in this work.

X. Gao, D. Botez, and I. Knezevic, "Multivalley simulation and design of quantum cascade lasers,"
in Encyclopedia of Nanoscience and Nanotechnology, Edited by H. S. Nalwa, American Scientific Publishers, in press. (2008)

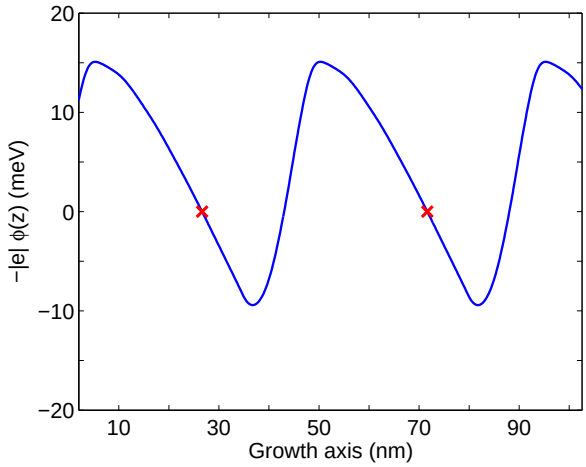

FIG. 10. Electrostatic potential energy profile $-|e|\phi(z)$ from the self-consistent Schrödinger-Poisson solver in two adjacent stages. The $\times$ marks define the stage where the Poisson equation is solved with periodic boundary conditions, and the resulting potential is then translated to the whole simulated region. It is noticed that the potential is periodic between stages.

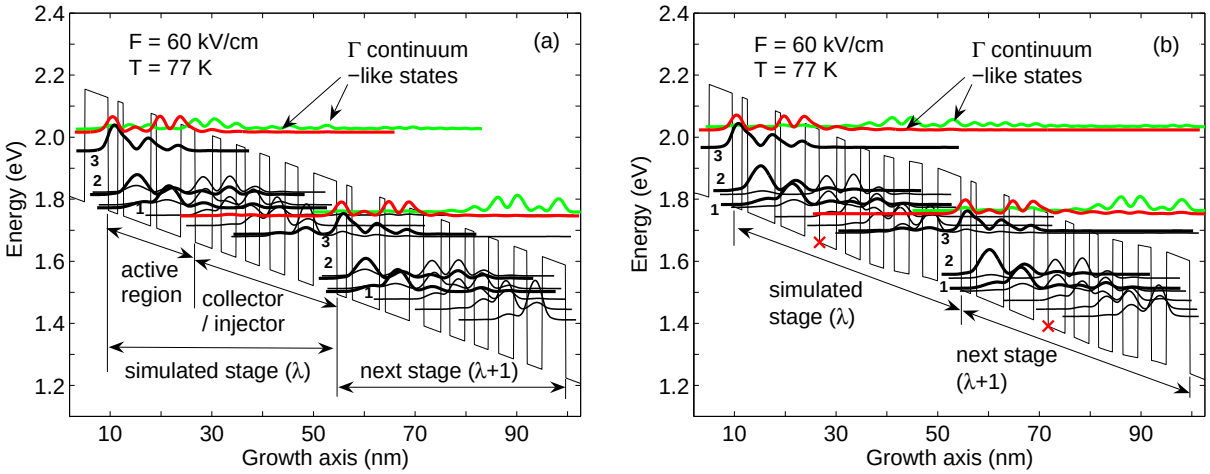

FIG. 11. Ten Γ-subband energy levels and wavefunction moduli squared for the 45% Al QCL [31] with $\phi(z) = 0$ (a) and with $\phi(z)$ (b) obtained from the self-consistent Schrödinger-Poisson solver.

D. Scattering Mechanisms

The various scattering mechanisms included in the Monte Carlo simulation are listed in Table I. The intervalley scattering mechanism is written in the form of A→B (e.g., $\Gamma \rightarrow X_x$) in the table, with A being the initial valley and B the final valley. The electron-LO

X. Gao, D. Botez, and I. Knezevic, "Multivalley simulation and design of quantum cascade lasers,"
in Encyclopedia of Nanoscience and Nanotechnology, Edited by H. S. Nalwa, American Scientific Publishers, in press. (2008)

TABLE I. Scattering mechanisms included in the Monte Carlo simulation for the Γ- and X-valley states. Reprinted with permission from [59], X. Gao, D. Botez, and I. Knezevic, *J. Appl. Phys.* 101, 063101 (2007). © 2007, American Institute of Physics.

	Γ valley	X_x valley	X_z valley
intrastage	electron-LO	electron-LO	electron-LO
$(\lambda \rightarrow \lambda)$	electron-electron		
&	$\Gamma \rightarrow X_x$	$X_x \rightarrow \Gamma$	$X_z \rightarrow \Gamma$
interstage	$\Gamma \rightarrow X_z$	$X_x \rightarrow X_x$	$X_z \rightarrow X_x$
$(\lambda \rightarrow \lambda \pm 1)$		$X_x \rightarrow X_z$	

phonon scattering is included for all the valleys, but the electron-electron (e-e) interaction is implemented only for the Γ states. (Electron population of the X valleys is relatively low under typical operating conditions, so the e-e scattering is not important.) The intervalley $X_x \rightarrow X_x$ scattering takes place due to the double-degeneracy of the X_x states. For all the scattering mechanisms, both the intrastage and interstage scattering events are included, with the latter yielding the current flow through the QCL. The interstage $\lambda \rightarrow \lambda - 1$ scattering rates are equal to those for the interstage $\lambda + 1 \rightarrow \lambda$, due to the translational symmetry. The Pauli exclusion principle of final states is included in the EMC code following the rejection technique of Lugli and Ferry [80].

1. Electron-longitudinal optical (LO) phonon scattering

The scattering of electrons with longitudinal polar optical (LO) phonons in a multiple-quantum-well (MQW) system is usually described by the Fröhlich interaction [81]. Though electrons have been widely accepted as quasi-two-dimensional (2D) particles in such systems, the correct model for the lattice vibrational modes is still an area of active research. The assumption of dispersionless unscreened bulk phonon modes has been shown [82] to reproduce the total scattering rates reasonably well in quantum-well systems, and is adopted in our calculation of the electron-LO phonon scattering rates in Secs. II-IV. The effect of spatial phonon confinement on the electron-LO scattering strength is studied in Sec. V, where it will be shown that the bulk phonon approximation is sufficiently good.

X. Gao, D. Botez, and I. Knezevic, "Multivalley simulation and design of quantum cascade lasers,"
in Encyclopedia of Nanoscience and Nanotechnology, Edited by H. S. Nalwa, American Scientific Publishers, in press. (2008)

The transition rate from a state $|\mathbf{k}, \nu\lambda\eta\rangle$ to a new state $|\mathbf{k}', \nu'\lambda'\eta\rangle$ (λ' could be λ, $\lambda+1$, or $\lambda-1$) is given by Fermi's Golden Rule

$$S_{\nu\lambda\eta}^{\nu'\lambda'\eta}(\mathbf{k},\mathbf{k}') = \frac{2\pi}{\hbar}\left|\langle \mathbf{k}', \nu'\lambda'\eta | H_{e-LO} | \mathbf{k}, \nu\lambda\eta\rangle\right|^2 \delta(E' - E \mp \hbar\omega_0), \tag{26}$$

where $\hbar\omega_0$ is the LO phonon energy, $\delta(\cdot)$ is the delta function, and the upper and lower signs correspond to phonon absorption and emission, respectively (this convention will be used throughout this section). The electron-LO interaction Hamiltonian H_{e-LO} takes the following form

$$H_{e-LO} = \left[\frac{e_0^2\hbar\omega_0}{2V}\left(\frac{1}{\varepsilon_\infty} - \frac{1}{\varepsilon_0}\right)\right]^{1/2} \sum_{\mathbf{Q}} \frac{1}{iQ}\left(\hat{a}_{\mathbf{Q}} e^{i\mathbf{Q}\cdot\mathbf{R} - i\omega_0 t} + \hat{a}_{\mathbf{Q}}^{+} e^{-i\mathbf{Q}\cdot\mathbf{R} + i\omega_0 t}\right), \tag{27}$$

for bulk LO phonons, where e_0 is the universal electron charge, V is the generic volume, ε_0 and ε_∞ are the static and high-frequency dielectric permittivity, respectively, $\mathbf{Q}$ is the bulk phonon wave vector, $\mathbf{R} = (\mathbf{r}, z)$, $\hat{a}_{\mathbf{Q}}$ and $\hat{a}_{\mathbf{Q}}^{+}$ are the phonon destruction and creation operators, respectively. The total scattering rate for an electron initially in subband ν, stage λ, to a final subband ν', stage λ', can obtained as [56, 81]

$$\begin{aligned}\Lambda_{\nu\lambda\eta}^{\nu'\lambda'\eta}(\mathbf{k}) = \sum_{\mathbf{k}'} S_{\nu\lambda\eta}^{\nu'\lambda'\eta}(\mathbf{k},\mathbf{k}') \;=\; & \frac{e_0^2\hbar\omega_0 m_{\nu'\lambda'}^{\eta *}}{8\pi\hbar^3}\left(n_0 + \frac{1}{2} \mp \frac{1}{2}\right)\left(\frac{1}{\varepsilon_\infty} - \frac{1}{\varepsilon_0}\right) \\ & \times \int_0^{2\pi} \mathrm{d}\theta \frac{F_{\nu\lambda\eta}^{\nu'\lambda'\eta}(q^{\pm})}{q^{\pm}} \vartheta\left(E_{\mathbf{k}} + E_{\nu\lambda}^{\eta} - E_{\nu'\lambda'}^{\eta} \pm \hbar\omega_0\right),\end{aligned} \tag{28}$$

where n_0 is the equilibrium phonon number, $\mathrm{q} = |\mathbf{k}' - \mathbf{k}|$, θ is the angle between $\mathbf{k}$ and $\mathbf{k}'$, and $\vartheta(\cdot)$ is the Heaviside step function.

The form factor function $F_{\nu\lambda\eta}^{\nu'\lambda'\eta}(q)$ depends on the valleys. For the Γ valley, since the electron wavefunctions include the influence of the valence bands, the form factor function is calculated by averaging over the elementary cell and employing the orthogonality of the zone-center Bloch functions $u_{j0}(\mathbf{r}, z)$ (j = c, lh, so). Then one obtains

$$F_{\nu\lambda\Gamma}^{\nu'\lambda'\Gamma}(q) = \sum_{j,j'} \int_0^d \mathrm{d}z \int_0^d \mathrm{d}z' \psi_{j,\nu'\lambda'}^{\Gamma}(z)\psi_{j',\nu'\lambda'}^{\Gamma *}(z')\psi_{j,\nu\lambda}^{\Gamma *}(z)\psi_{j',\nu\lambda}^{\Gamma}(z') e^{-q|z-z'|}. \tag{29}$$

For $\ell = \mathrm{X}_x, \mathrm{X}_z$ valleys, the form factor is calculated using the envelope functions as

$$F_{\nu\lambda\ell}^{\nu'\lambda'\ell}(q) = \int_0^d \mathrm{d}z \int_0^d \mathrm{d}z' \psi_{\nu'\lambda'}^{\ell}(z)\psi_{\nu'\lambda'}^{\ell *}(z')\psi_{\nu\lambda}^{\ell *}(z)\psi_{\nu\lambda}^{\ell}(z') e^{-q|z-z'|}. \tag{30}$$

X. Gao, D. Botez, and I. Knezevic, "Multivalley simulation and design of quantum cascade lasers,"
in Encyclopedia of Nanoscience and Nanotechnology, Edited by H. S. Nalwa, American Scientific Publishers, in press. (2008)

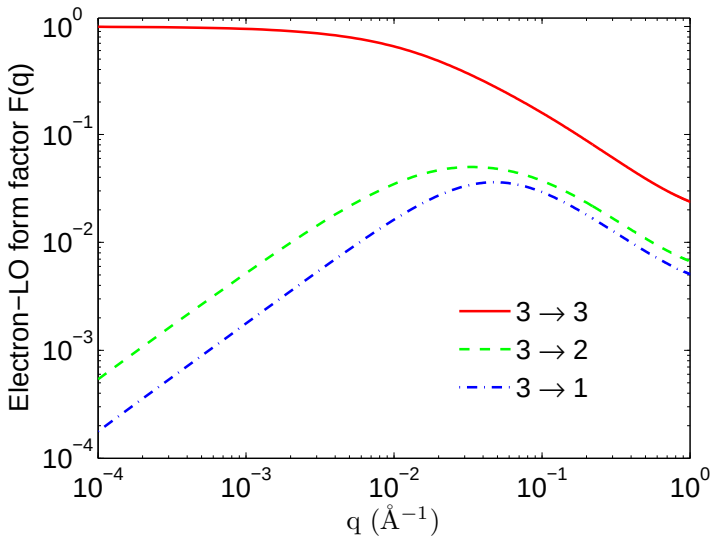

FIG. 12. Selected form factors for intrasubband ($3 \rightarrow 3$) and intersubband ($3 \rightarrow 2$, $3 \rightarrow 1$) electron-LO scattering within the same stage λ for the Γ-subbands 3, 2, 1 shown in the left panel of Fig. 11.

The allowed q's are fixed by the in-plane momentum conservation ($\mathbf{k}' = \mathbf{k} \pm \mathbf{q}$) and the energy conservation [Eq. (26)] laws. Taking into account the difference of the electron effective mass between the initial and final states, one obtains

$$\begin{aligned} q^{\pm} &= \frac{\sqrt{2}}{\hbar} \left\{ (m^{\eta *}_{\nu\lambda} + m^{\eta *}_{\nu'\lambda'}) E_{\mathbf{k}} + m^{\eta *}_{\nu'\lambda'} (\hbar\omega^{\pm}_{\nu\nu'}) \right. \\ &- \left. 2 \left[m^{\eta *}_{\nu\lambda} m^{\eta *}_{\nu'\lambda'} E_{\mathbf{k}} \left(E_{\mathbf{k}} + \hbar\omega^{\pm}_{\nu\nu'} \right) \right]^{\frac{1}{2}} \cos\theta \right\}^{\frac{1}{2}}, \end{aligned} \tag{31}$$

with $\hbar\omega^{\pm}_{\nu\nu'} = E^{\eta}_{\nu\lambda} - E^{\eta}_{\nu'\lambda'} \pm \hbar\omega_0$. Figure 12 plots the form factors $F^{3\lambda\Gamma}_{3\lambda\Gamma}(q)$ ($3 \rightarrow 3$), $F^{2\lambda\Gamma}_{3\lambda\Gamma}(q)$ ($3 \rightarrow 2$), and $F^{1\lambda\Gamma}_{3\lambda\Gamma}(q)$ ($3 \rightarrow 1$) as a function of q for the Γ-subbands 3, 2, 1 in the left panel of Fig. 11.

2. Intervalley scattering

It has been shown [83] that the phonon-assisted intervalley $\Gamma - X_x$ and $\Gamma - X_z$ electron transitions can be modeled through an intervalley deformation potential (DP). For bulk intervalley phonons, the total intervalley scattering rate for an electron from a state $|\mathbf{k}, \nu\lambda\eta\rangle$

X. Gao, D. Botez, and I. Knezevic, "Multivalley simulation and design of quantum cascade lasers,"
in Encyclopedia of Nanoscience and Nanotechnology, Edited by H. S. Nalwa, American Scientific Publishers, in press. (2008)

to a state of subband ν', stage λ', and valley η' is given by [81]

$$\Lambda_{\nu\lambda\eta}^{\nu'\lambda'\eta'}(\mathbf{k}) = \frac{Z_{\eta'} D_{\eta\eta'}^2 m_{\nu'\lambda'}^{\eta'*}}{2\hbar\rho E_{\eta\eta'}} \left(n_{\eta\eta'} + \frac{1}{2} \mp \frac{1}{2} \right) I_{\nu\lambda\eta}^{\nu'\lambda'\eta'} \vartheta \left(E_{\mathbf{k}} + E_{\nu\lambda}^{\eta} - E_{\nu'\lambda'}^{\eta'} \pm E_{\eta\eta'} \right), \tag{32}$$

where $D_{\eta\eta'}$ is the intervalley ($\eta - \eta'$) deformation potential constant, ρ is the mass density, and $E_{\eta\eta'}$ is the intervalley phonon energy; $n_{\eta\eta'}$ is the equilibrium intervalley phonon occupancy, and $Z_{\eta'}$ is the degeneracy of the final valley ($Z_\Gamma = 1$, $Z_{\mathrm{X}_z} = 1$, and $Z_{\mathrm{X}_x} = 1$ for intervalley $\mathrm{X}_x - \mathrm{X}_x$, 2 for others). The overlap integral $I_{\nu\lambda\eta}^{\nu'\lambda'\eta'}$ is given by

$$I_{\nu\lambda\Gamma}^{\nu'\lambda'\ell} = \sum_j \int_0^d \mathrm{d}z \left| \psi_{j,\nu\lambda}^{\Gamma}(z) \right|^2 \left| \psi_{\nu'\lambda'}^{\ell}(z) \right|^2, \tag{33a}$$

$$I_{\nu\lambda\ell}^{\nu'\lambda'\ell'} = \int_0^d \mathrm{d}z \left| \psi_{\nu\lambda}^{\ell}(z) \right|^2 \left| \psi_{\nu'\lambda'}^{\ell'}(z) \right|^2, \tag{33b}$$

where the first equation is for the scattering between Γ and ℓ ($\ell = \mathrm{X}_x, \mathrm{X}_z$) valleys, and the second one is for the intervalley scattering among the X valleys. All the material constants necessary for calculating scattering rates have been taken from GaAs [62].

3. Electron-electron scattering

The electron-electron (e-e) scattering among the Γ-subbands has a significant effect [41] on QCL structures. The e-e scattering is included for the Γ subbands, but not for the X subbands, since the electron densities in the X valleys are fairly low, except at high fields (above threshold). The e-e interaction may be divided into the binary e-e scattering and electron-plasmon coupling, with the latter being important in highly-doped systems and neglected in our calculation. The binary quasi-2D e-e scattering is treated by taking into account both the antiparallel-spin and parallel-spin e-e collisions, with the exchange effect [84] included for the parallel-spin collisions.

One can consider a "principal" Γ-electron in subband ν, stage λ, with an in-plane wave vector $\mathbf{k}$, and a "partner" Γ-electron in subband μ, stage λ_0, with a wave vector $\mathbf{k}_0$. Since the e-e scattering involves only the Γ valley, the valley index will be omitted in the following. The final states of these two electrons are, respectively, $|\mathbf{k}', \nu'\lambda'\rangle$ and $|\mathbf{k}_0', \mu'\lambda_0'\rangle$. The total electron scattering rate from the state $|\mathbf{k}, \nu\lambda\rangle$ into a final state of subband ν', stage λ', is

X. Gao, D. Botez, and I. Knezevic, "Multivalley simulation and design of quantum cascade lasers,"
in Encyclopedia of Nanoscience and Nanotechnology, Edited by H. S. Nalwa, American Scientific Publishers, in press. (2008)

given by [85]

$$\Lambda_{\nu\lambda}^{\nu'\lambda'}(\mathbf{k}) = \frac{e_0^4 m_{\nu\lambda}^*}{32\pi\hbar^3\varepsilon_\infty^2 A}\sum_{\mathbf{k}_0,\sigma}\sum_{\mu\mu'}\sum_{\lambda_0\lambda_0'} f_{\mu\lambda_0}(\mathbf{k}_0) \times \int_0^{2\pi} \mathrm{d}\theta \left[\frac{|F(q)|^2}{q^2\epsilon^2(q)} + \frac{|F(q')|^2}{q'^2\epsilon^2(q')} - \frac{|F(q)|\,|F(q')|}{q\epsilon(q)q'\epsilon(q')}\right], \tag{34}$$

where σ denotes the spin of electrons, $f_{\mu\lambda_0}(\mathbf{k}_0)$ is the Γ-valley electron distribution, θ is the angle between $\mathbf{g}$ ($\mathbf{g} = \mathbf{k}_0 - \mathbf{k}$) and $\mathbf{g}'$ ($\mathbf{g}' = \mathbf{k}_0' - \mathbf{k}'$), $q = |\mathbf{g} - \mathbf{g}'|/2$, and $\epsilon(q)$ is the static dielectric function; each of the three indices (λ', λ_0, λ_0') could be λ, λ + 1, or λ - 1. The form factor function $F(q)$ (with indices omitted for compactness) satisfies

$$F_{\nu\mu\nu'\mu'}^{\lambda\lambda_0\lambda'\lambda_0'}(q) = \sum_{i,j}\int_0^d \mathrm{d}z \int_0^d \mathrm{d}z' \psi_{i,\nu\lambda}^{\Gamma}(z)\psi_{i,\nu'\lambda'}^{\Gamma *}(z)\psi_{j,\mu\lambda_0}^{\Gamma}(z')\psi_{j,\mu'\lambda_0'}^{\Gamma *}(z')e^{-q|z-z'|}, \tag{35}$$

with i and j both running over the three bands (c, lh, so) at the zone-center. The values of q and q' are determined by

$$q = \frac{1}{2}\left[2g^2 + g_0^2 - 2g\sqrt{g^2+g_0^2}\cos\theta\right]^{1/2}, \tag{36a}$$

$$q' = \frac{1}{2}\left[2g^2 + g_0^2 + 2g\sqrt{g^2+g_0^2}\cos\theta\right]^{1/2}, \tag{36b}$$

where

$$g = |\mathbf{g}|, \quad g_0 = \frac{2}{\hbar}\left[m_{\nu\lambda}^{\Gamma *}\left(E_{\nu\lambda}^{\Gamma} + E_{\mu\lambda_0}^{\Gamma} - E_{\nu'\lambda'}^{\Gamma} - E_{\mu'\lambda_0'}^{\Gamma}\right)\right]^{1/2}. \tag{37}$$

Figure 13 shows the form factors as a function of q for intrasubband and intersubband electron-electron scattering within the same stage λ, for Γ-subband wavefunctions of Fig. 6.

Analysis of the screening phenomena in multisubband systems, such as QCLs, is a formidable task. The effect of multisubband screening is treated within the static random-phase approximation (RPA) [86]. In the long-wavelength limit $q \to 0$, for intrasubband ($\nu = \nu'$, $\lambda = \lambda'$, $\mu = \mu'$, $\lambda_0 = \lambda_0'$) e-e transitions, the static dielectric function may be written as [87]

$$\epsilon(q) = 1 + \sum_{\nu=1}^{\mathrm{N}_\Gamma} f_{\nu\lambda}(0)\frac{q_{\nu\lambda}}{q}, \quad q_{\nu\lambda} = \frac{e_0^2 m_{\nu\lambda}^{\Gamma *}}{2\pi\hbar^2\varepsilon_\infty}, \tag{38}$$

where $f_{\nu\lambda}(0)$ is the occupancy of the bottom of the subband ν in the central stage λ. The occupancy $f_{\nu\lambda}(0)$ is evaluated at each time step in the EMC simulation, allowing for the screening function to be adjusted according to the actual electron distribution.

X. Gao, D. Botez, and I. Knezevic, "Multivalley simulation and design of quantum cascade lasers,"
in Encyclopedia of Nanoscience and Nanotechnology, Edited by H. S. Nalwa, American Scientific Publishers, in press. (2008)

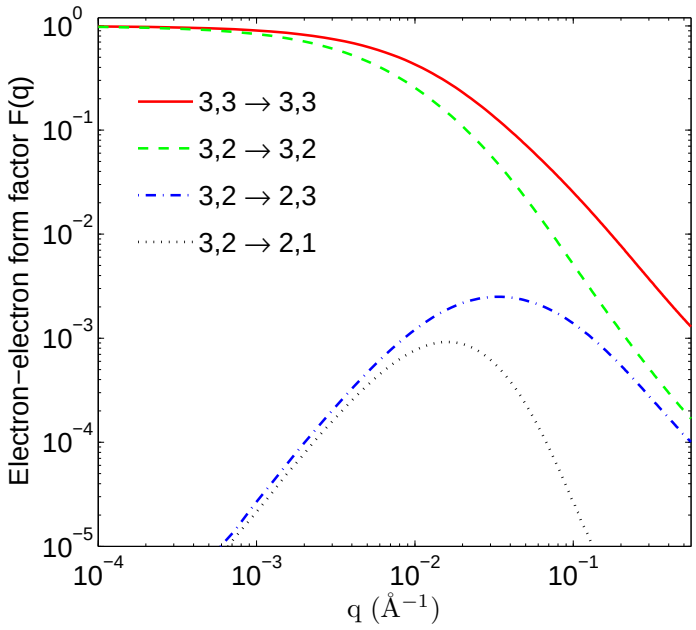

FIG. 13. Selected form factors for intrasubband [(3, 3) → (3, 3), (3, 2) → (3, 2)] and intersubband [(3, 2) → (2, 3), (3, 2) → (2, 1)] electron-electron scattering within the same stage λ for Γ-subband wavefunctions shown in Fig. 6, where $(\nu, \mu) \rightarrow (\nu', \mu')$ denotes that the principal electron in subband ν is scattered to subband ν' and the partner electron in subband μ is scattered to subband μ' due to the electron-electron scattering.

For intersubband e-e scattering, the effect of screening is expected to be much smaller than for the intrasubband case, since the dielectric function is weighted by the form factor functions within the RPA, and the intersubband form factors are much lower in magnitude and vanish for $q = 0$, as seen in Fig. 13, due to the orthogonality of the envelope functions. Therefore, to first-order, one can treat the intersubband e-e scattering as unscreened, which is also validated by Fig. 3 of Ref. [44], where the unscreened intersubband Coulomb potential is very close to their screened potential.

The implementation of the e-e interaction in the EMC code follows the technique of Goodnick and Lugli [88]: precalculate the form factors as a function of q according to Eq. (35) (note that one can make use of the symmetry to reduce the computation), then compute the scattering rate $\Lambda_{\nu\lambda}^{\nu'\lambda'}(\mathbf{k})$ in Eq. (34) by replacing the integrand with the square of the maximum value of $F_{\nu\mu\nu'\mu'}^{\lambda\lambda_0\lambda'\lambda_0'}(q)$ for given $\nu\lambda, \nu'\lambda'$, divided by $q_{\nu\lambda}^2$ given in (38); the actual value of the integrand function is accounted for through a rejection method when the

X. Gao, D. Botez, and I. Knezevic, "Multivalley simulation and design of quantum cascade lasers,"
in Encyclopedia of Nanoscience and Nanotechnology, Edited by H. S. Nalwa, American Scientific Publishers, in press. (2008)

final state is chosen. The scattering rate employed in the simulation is computed using half of the rate Eq. (34), since each electron from the simulated ensemble is scattered both as a principal electron and as a scattering partner [89]. In addition, it is necessary to update both the principal electron and its partner electron after the e-e collisions, in order to conserve the energy and momentum in the system [89].

III. X-VALLEY LEAKAGE IN GAAS/ALGAAS QUANTUM CASCADE LASERS

In this section, the Monte Carlo simulator presented in Sec. II is applied to simulate two GaAs-based mid-infrared QCLs with equivalent designs: the GaAs/$Al_{0.33}Ga_{0.67}As$ QCL of Refs. [28] and [29] (referred to as the 33% QCL), and the GaAs/$Al_{0.45}Ga_{0.55}As$ QCL of Ref. [31] (referred to as the 45% QCL). Designs of these two QCLs are equivalent [31], since they have similar emitting wavelengths (~ 9.4 μm), threshold fields (48 kV/cm), dipole matrix elements (1.6 nm for the 33% QCL and 1.7 nm for the 45% QCL), and lifetimes in the upper lasing level (1.5 ps and 1.4 ps, respectively).

Figure 14 shows the Γ-subband energy levels and wavefunction moduli squared in two adjacent stages for the 33% QCL (Fig. 14a) and the 45% QCL (Fig. 14b) at the above-threshold field F = 53 kV/cm and the lattice temperature T = 77 K. For the 33% QCL [28], the thicknesses of the layers in one stage (in Å), starting from the injection barrier (the widest barrier in a stage), are **58**, 15, **20**, 49, **17**, 40, **34**, 32, **20**, 28, **23**, 23, **25**, 23, **25**, 21. For the 45% QCL [31], the thicknesses of the layers in one stage (in Å), starting from the injection barrier (the widest barrier in a stage), are **46**, 19, **11**, 54, **11**, 48, **28**, 34, **17**, 30, **18**, 28, **20**, 30, **26**, 30. The bold script denotes the barriers, the normal script are the wells, and the underlined script denotes the n-type doped regions with a sheet density of $N_s = 3.9\times10^{11}$ cm^{-2} for the 33% QCL, $N_s = 3.8\times10^{11}$ cm^{-2} for the 45% QCL.

In each stage, ten Γ-subbands, including two Γ-continuum states (Γ_c), are used in the simulation of both lasers. In the 33% QCL, the upper lasing level and the injector localized states (Γ_l) are quite close to the Γ band edge, and there is appreciable wavefunction overlap between Γ_l and the next-stage Γ_c. On the other hand, in the 45% case, the Γ-point conduction band offset between the wells and the barriers increases by about 90 meV due to the higher Al content, so in order to achieve a similar emission wavelength (~ 9.4 μm), the

X. Gao, D. Botez, and I. Knezevic, "Multivalley simulation and design of quantum cascade lasers,"
in Encyclopedia of Nanoscience and Nanotechnology, Edited by H. S. Nalwa, American Scientific Publishers, in press. (2008)

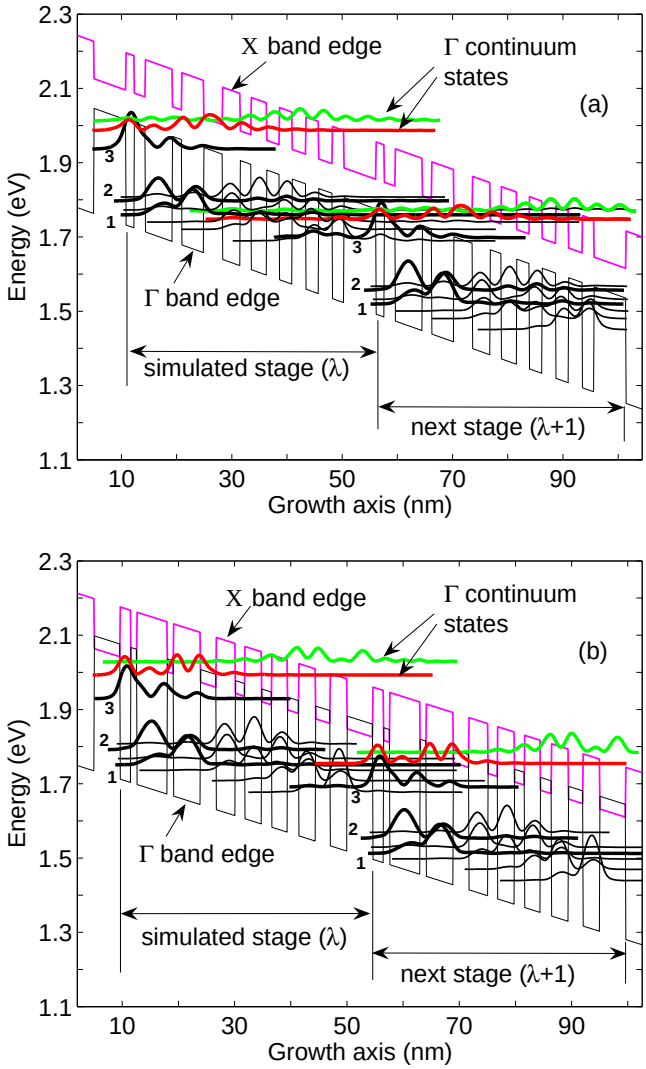

FIG. 14. Γ-subband energy levels and wavefunction moduli squared in two adjacent stages for the 33% QCL (a) and the 45% QCL (b) at F = 53 kV/cm (above-threshold) and T = 77 K. The bold black lines denote the active lasing levels (3 - upper lasing level, 2 - lower lasing level, 1 - active ground level). The black thin lines are the localized injector states (Γ_l), while the top two (red and green) are the continuum states (Γ_c). The radiative transition occurs between levels 3 and 2. Reprinted with permission from [59], X. Gao, D. Botez, and I. Knezevic, *J. Appl. Phys.* 101, 063101 (2007). © 2007, American Institute of Physics.

active lasing levels and the Γ_l levels are farther away from the Γ band edge than in the 33% QCL. Consequently, the wavefunction overlap between Γ_l and next-stage Γ_c is negligible in the 45% QCL.

The X-subbands under the same conditions are displayed in Fig. 15, with the Γ_c states

X. Gao, D. Botez, and I. Knezevic, "Multivalley simulation and design of quantum cascade lasers,"
in Encyclopedia of Nanoscience and Nanotechnology, Edited by H. S. Nalwa, American Scientific Publishers, in press. (2008)

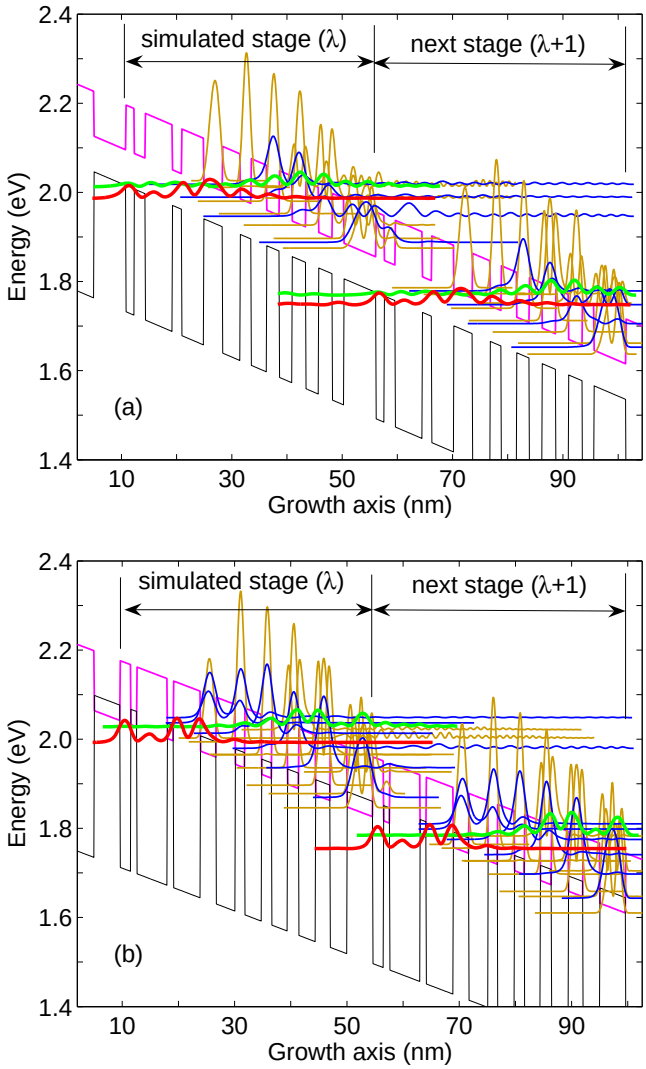

FIG. 15. X-subband energy levels and wavefunction moduli squared in two adjacent stages for the 33% QCL (a) and the 45% QCL (b) at F = 53 kV/cm and T = 77 K. The blue lines denote the doubly-degenerate X_x states, and the yellow ones are the X_z states, while the red and green lines are the Γ_c subbands. Reprinted with permission from [59], X. Gao, D. Botez, and I. Knezevic, *J. Appl. Phys.* 101, 063101 (2007). © 2007, American Institute of Physics.

also plotted, where Fig. 15a is for the 33% QCL and Fig. 15b for the 45% case. The number of X states in both stages is the same for each laser and chosen such that the highest X subband is right above the second Γ_c state and below other higher X levels. Since the X band edge is about 83 meV above the Γ band edge in the 33% QCL, but $\sim$ 30 meV below in the 45% QCL, more X subbands are needed to properly simulate the latter device. In particular, at F = 53 kV/cm and T = 77 K, nine (ten) X_z subbands and four (six) X_x

X. Gao, D. Botez, and I. Knezevic, "Multivalley simulation and design of quantum cascade lasers,"
in Encyclopedia of Nanoscience and Nanotechnology, Edited by H. S. Nalwa, American Scientific Publishers, in press. (2008)

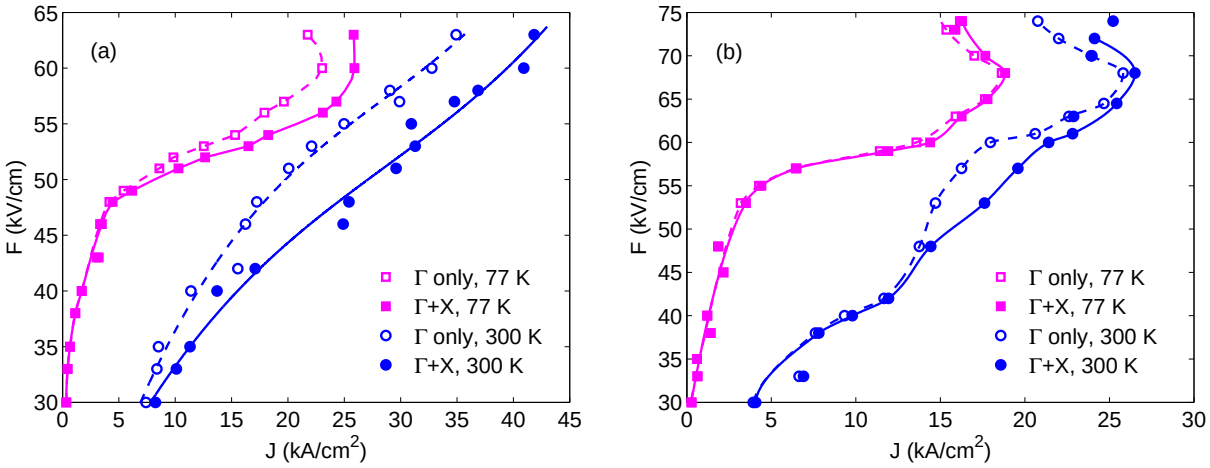

FIG. 16. Electric field vs current density characteristics for the 33% QCL (a) and the 45% QCL (b) at the lattice temperatures of 77 K and 300 K, with and without X-valley transport. Reprinted with permission from [58], X. Gao, D. Botez, and I. Knezevic, *Appl. Phys. Lett.* 89, 191119 (2006). © 2006, American Institute of Physics.

subbands are used in the 33% (45%) QCL simulation. It is clear from the figures that in both lasers, the Γ_c states are strongly coupled to the X states in the same stage.

A. X-Valley Leakage Mechanism

The applied field vs. current density characteristics at the lattice temperatures of 77 K and 300 K are shown in Fig. 16 for the 33% QCL (Fig. 16a) and the 45% QCL (Fig. 16b), with and without the X-valley transport included. (Note that the leakage to Γ-continuum states [53] is accounted for as part of the Γ-valley current, so it is present in both curves.) The calculated threshold current densities ($J_{\rm th}$) at the threshold field F = 48 kV/cm are summarized in Table II, together with the available experimental data. It can be seen that the calculated $J_{\rm th}$ values are in very good agreement with the experimental data, considering that the simulation does not account for the losses at the lateral waveguide (ridge) edges. Subsequent experimental work [22] on 45% QCLs, where the ridge edges had smooth surfaces due to wet chemical etching and no absorbing material, reported $J_{\rm th}$ (77 K) = 3 kA/cm^2, in excellent agreement with 2.9 kA/cm^2 obtained in our calculation.

At the cryogenic temperature, the inclusion of X-valley transport has a very negligible

X. Gao, D. Botez, and I. Knezevic, "Multivalley simulation and design of quantum cascade lasers,"
in Encyclopedia of Nanoscience and Nanotechnology, Edited by H. S. Nalwa, American Scientific Publishers, in press. (2008)

TABLE II. Calculated threshold current densities $J_{\rm th}$ with and without X-valley transport. Reprinted with permission from [59], X. Gao, D. Botez, and I. Knezevic, *J. Appl. Phys.* 101, 063101 (2007). © 2007, American Institute of Physics.

	$J_{\rm th}$ (kA/cm^2), 77 K			$J_{\rm th}$ (kA/cm^2), 300 K		
	w/o X	w/ X	Exper.	w/o X	w/ X	Exper.
33% QCL	4.1	4.4	5.0[a]	17.2	25.5	N/A
45% QCL	2.9	2.9	4.0[b]	13.7	14.4	16.7[b]

[a]Reference [29].
[b]Reference [31].

effect on the current density up to above-threshold fields in both QCLs, but the 33% QCL shows about 1 kA/cm^2 higher $J_{\rm th}$ than the 45% QCL in both theory and experiment. This difference is primarily due to the strong interstage leakage from the injector localized states (Γ_l) (thin black curves in Fig. 17a) to the next-stage Γ-continuum states (Γ_c) (green curves in Fig. 17a) in the 33% QCL. Ideally, all electrons in the Γ_l-states are expected to inject into the next-stage upper lasing level 3 (bold black curves in Fig. 17) for lasing transitions. In reality, however, the overlap between Γ_l and the next-stage Γ_c wavefunctions causes some electrons to leak into Γ_c, and these electrons do not contribute to the lasing process. In the 33% QCL, this overlap is large, due to poor localization of the Γ_l-states (Fig. 17a), while in the 45% case, the overlap is much smaller, thanks to the higher Γ-valley barriers, as seen in Fig. 17b. So it is the relatively large leakage from the Γ_l-states to the next-stage Γ_c-states that results in higher threshold current in the 33% QCL. This mechanism of leakage to the Γ_c-states has been well recognized [22, 31, 90] and studied [60].

At room temperature, the simulated threshold current in the 33% structure with the X-valley transport included is very high ($J_{\rm th} = 25.5$ kA/cm^2), which can help explain why the 33% QCL could not lase at 300 K. The increase in current density due to the inclusion of X-valley transport (X-valley leakage current) in the 33% QCL is very large, even at fields significantly below threshold, equaling 8.3 kA/cm^2 at threshold. In contrast, the X-valley leakage current in the 45% QCL is rather low in the whole simulated field range.

Figure 18 presents a variation of electron population in the Γ- and X-valleys with the field

X. Gao, D. Botez, and I. Knezevic, "Multivalley simulation and design of quantum cascade lasers,"
in Encyclopedia of Nanoscience and Nanotechnology, Edited by H. S. Nalwa, American Scientific Publishers, in press. (2008)

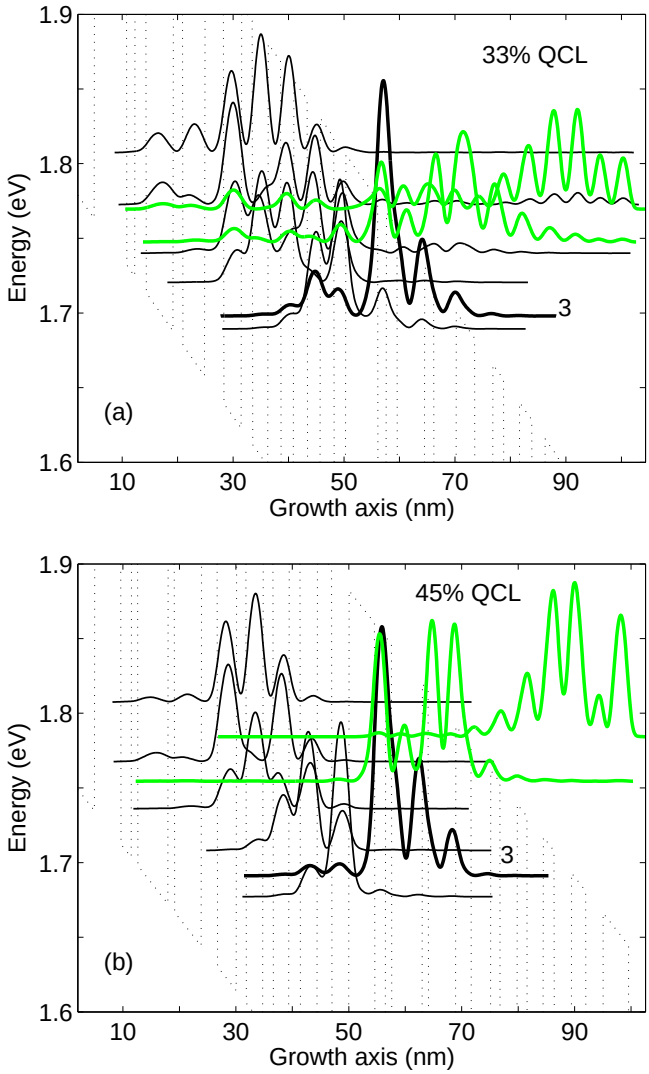

FIG. 17. Blow-up of the wavefunction moduli squared of the injector states (Γ_l) and the next-stage Γ-continuum (Γ_c) states in the 33% QCL (a) and the 45% QCL (b). Thin black curves denote the injector states, while the green ones are the next-stage Γ_c-states. The bold black curve 3 is the upper lasing level in the next stage, and the dotted black line indicates the Γ-valley band edge.

at different temperatures. By comparing the trends in Fig. 16 and Fig. 18 at 300 K, one can observe that both the X-valley leakage current and the X-valley electron population increase with the field in both lasers, which suggests that the increase in the X-valley leakage current follows the increase in the X-valley population (also true at 77 K, although somewhat less obvious). This is due to the fact that interstage X→X intervalley scattering is the dominant X-leakage mechanism in both QCLs, more efficient than direct interstage scattering between Γ and X. The dominant X-valley leakage takes place through the three-step mechanism

X. Gao, D. Botez, and I. Knezevic, "Multivalley simulation and design of quantum cascade lasers,"
in Encyclopedia of Nanoscience and Nanotechnology, Edited by H. S. Nalwa, American Scientific Publishers, in press. (2008)

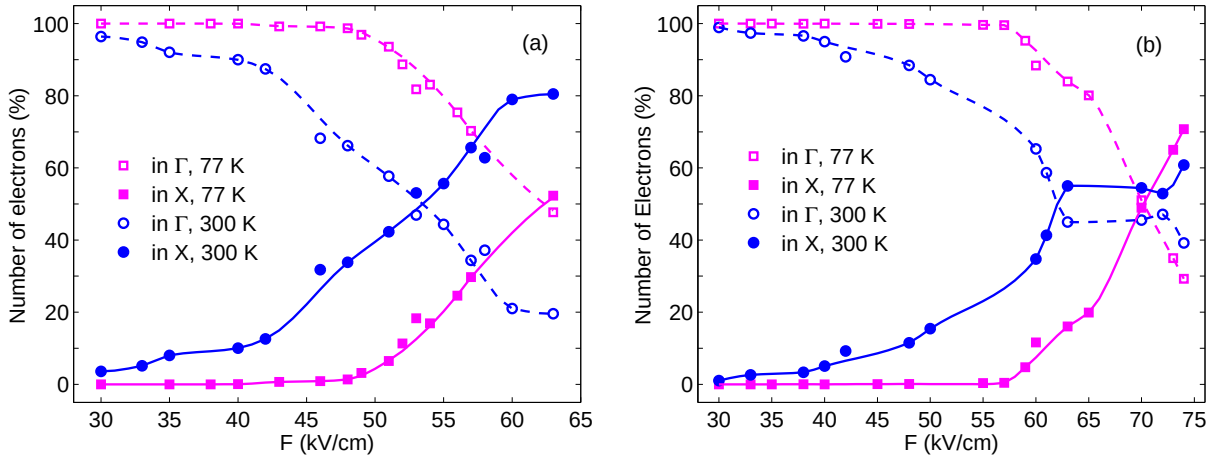

FIG. 18. Electron population in Γ and X valleys vs applied field for the 33% QCL (a) and the 45% QCL (b) at the lattice temperatures of 77 K and 300 K. Reprinted with permission from [58], X. Gao, D. Botez, and I. Knezevic, *Appl. Phys. Lett.* 89, 191119 (2006). © 2006, American Institute of Physics.

sketched in Fig. 19. First of all, the coupling between the injector states (Γ_l) and the next-stage Γ_c states results in the leakage current J_c, indicated by the red horizontal arrows. Secondly, once those continuum states are populated, a portion of the electrons will efficiently scatter into the same-stage X valleys (provided there are enough intervalley phonons to enable the transition), indicated by the green vertical arrows, because the X states have larger effective masses and are strongly coupled to the same-stage Γ_c states in both QCLs, as seen from their large wavefunction overlap in Fig. 15. The inverse scattering is significantly less efficient, because of the Γ-valley lower mass, so carriers scattered into the X-valleys tend to remain there rather than go back to Γ. Thirdly, with enough population in the X-subbands and the fact that the plane-wave-like tails of the X wavefunctions in one stage couple to the X states in the next stage (also seen in Fig. 15), the X→X intervalley scattering between adjacent stages occurs, giving rise to the leakage current J_X, indicated by the blue arrows. Other leakage paths, e.g., from Γ_l to the next-stage X states, are less efficient. Therefore, a large overlap between Γ_l and the next-stage Γ_c causes not only leakage to the Γ-continuum, J_c, but also significant parallel X-to-X leakage, J_X.

After identifying the dominant X-valley leakage mechanism, we are ready to explain why there is a large X-valley leakage current J_X in the 33% QCL at room temperature even at

X. Gao, D. Botez, and I. Knezevic, "Multivalley simulation and design of quantum cascade lasers,"
in Encyclopedia of Nanoscience and Nanotechnology, Edited by H. S. Nalwa, American Scientific Publishers, in press. (2008)

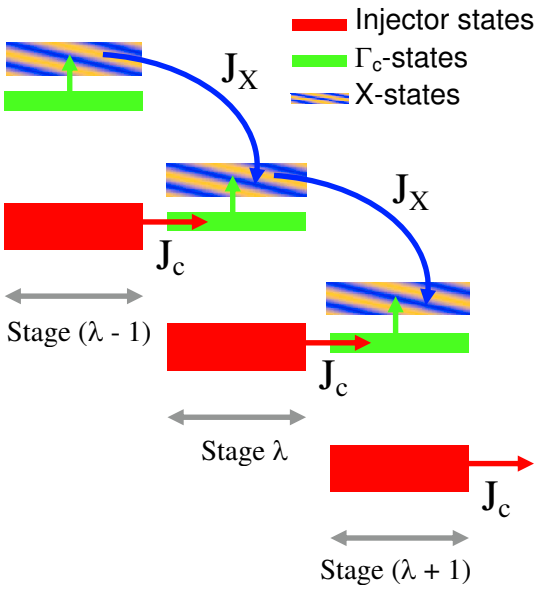

FIG. 19. Schematic of the dominant X-valley leakage mechanism in both the 33% and 45% QCLs. Reprinted with permission from [59], X. Gao, D. Botez, and I. Knezevic, *J. Appl. Phys.* 101, 063101 (2007). © 2007, American Institute of Physics.

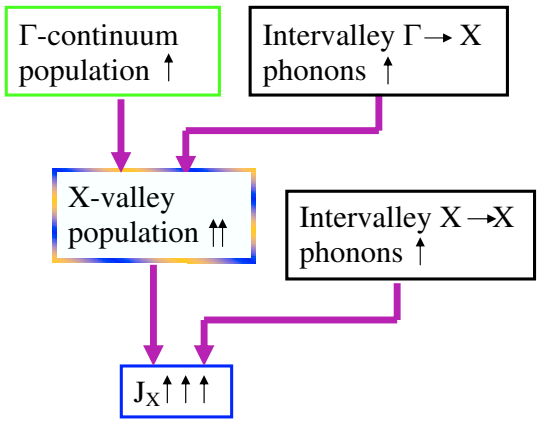

FIG. 20. Block diagram illustrating the large X-valley leakage current at 300 K in the 33% QCL.

low fields, but not in the 45% device. The reason is illustrated in Fig. 20. The value of J_X relies on the X-valley population and the number of intervalley X-X phonons. In the 33% QCL, at room temperature, the leakage J_c is very strong, due to both the large wavefunction overlap between Γ_l and Γ_c and the increase in the number of polar optical phonons, which leads to high Γ_c population. At the same time, the number of intervalley Γ-to-X phonons increases. The combination of these two factors results in highly efficient scattering from

X. Gao, D. Botez, and I. Knezevic, "Multivalley simulation and design of quantum cascade lasers,"
in Encyclopedia of Nanoscience and Nanotechnology, Edited by H. S. Nalwa, American Scientific Publishers, in press. (2008)

Γ_c to the same-stage X states (green arrows in Fig. 19), implying high X-valley population, since the scattering process efficiency depends on the number of phonons as well as the initial occupation. In addition, the number of intervalley (large phonon wave vector q) X-X phonons is also raised. Consequently, intervalley X-X scattering between adjacent stages is greatly enhanced, producing a large $J_{\rm X}$. In the 45% QCL, in contrast, Γ_c does not get filled through $\Gamma_l \rightarrow \Gamma_c$ scattering because their overlap is very small (Fig. 17b), which explains the near-zero $J_{\rm X}$ below threshold (Fig. 16b). Only at very high fields, Γ_c gets filled by intrastage scattering (i.e., high fields lead to high electronic temperatures), which then augments the leakage current $J_{\rm X}$ to some extent. The mechanism of X-valley leakage described above holds at 77 K as well, but leakage is much less pronounced because of few active phonons that enable intervalley scattering.

B. Electron-Electron Interaction and Electron Heating

The electron-electron (e-e) interaction plays a minor role in affecting the electron distribution for low electron sheet densities, and electrons relax their energy via a cascade of successive optical-phonon emissions ($\hbar\omega_{LO} \approx 36$ meV). However, for typical sheet densities in GaAs-based mid-IR QCLs (e.g., $N_s = 3.9 \times 10^{11}$ cm^{-2}), the e-e scattering has a significant effect on the steady-state electron distribution. Figure 21 displays the electron distributions in various Γ-subbands as a function of the in-plane electron kinetic energy at the above-threshold field F = 53 kV/cm and T = 77 K, without the e-e interaction (a), and with the e-e interaction (b), for the 33% QCL with a sheet density of 3.9×10^{11} cm^{-2}. It is clear that the e-e scattering drives the distribution in each subband to a heated Maxwellian profile [i.e., $f(E_k) \sim {\rm e}^{-E_k/k_B T_e}$]. This agrees with the findings by Iotti and Rossi [91]: for high electron densities, the e-e scattering is very effective in setting up a drifted Maxwellian distribution with a high electron temperature, and for typical operating conditions, electrons in QCLs thermalize within each subband. The slopes of the electron distributions in different subbands are fairly similar in Fig. 21b, indicating that the various subbands have an effective common electron temperature, as also found in Ref. [92]. The role of the e-e scattering is again crucial in setting up this behavior. As pointed out in Ref. [92], it can be mainly ascribed to the bi-intrasubband e-e scattering processes, i.e., two electrons in different subbands interact and stay in their own original subbands. These processes provide

X. Gao, D. Botez, and I. Knezevic, "Multivalley simulation and design of quantum cascade lasers,"
in Encyclopedia of Nanoscience and Nanotechnology, Edited by H. S. Nalwa, American Scientific Publishers, in press. (2008)

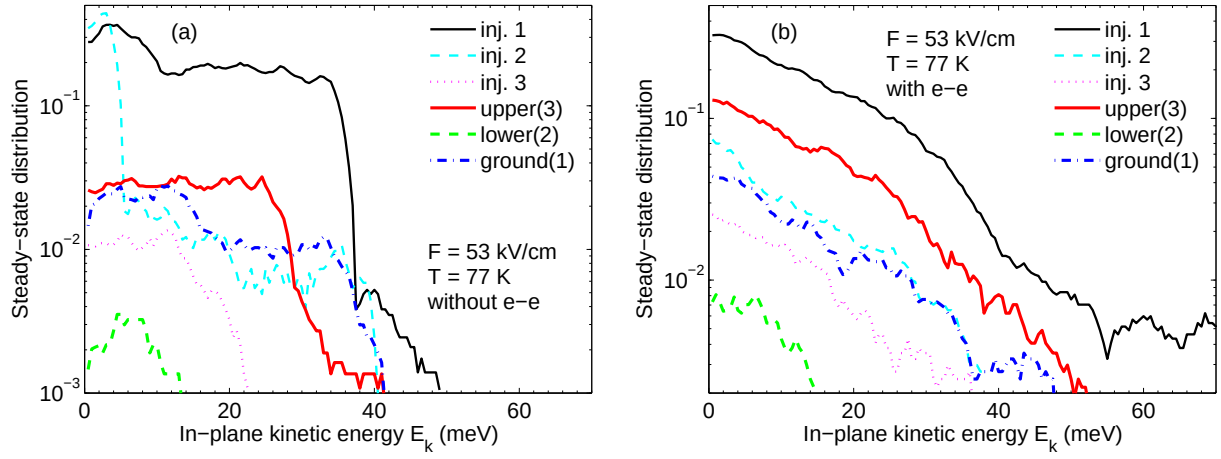

FIG. 21. Steady-state electron distributions in various Γ-subbands as a function of the in-plane kinetic energy at the above-threshold field F = 53 kV/cm and T = 77 K, without the e-e interaction (a) and with the e-e interaction (b) for the 33% QCL. In the legend of the figures, the first three indicate that the distributions are for the lowest three injector states (Γ_l), while the remaining three are for the lasing levels (3 - upper lasing level, 2 - lower lasing level, 1 - active ground level) indicated in Fig. 14a.

a very efficient way of redistributing excess kinetic energy among the electrons in order to achieve a common electron temperature. At high bias, such temperature is usually much higher than the lattice temperature. For example, in the case of Fig. 21b, the distribution function slope of the injector ground level (inj. 1) gives an approximate electron temperature of 221 K, much higher than the lattice temperature of 77 K. This estimated value of 221 K agrees well with the steady-state averaged electron temperature (244 K) obtained using $T_e = \langle E_k \rangle / k_B$ for a two-dimensional electron system, with $\langle E_k \rangle$ being the ensemble-averaged electron kinetic energy and k_B the Boltzmann constant.

The electron temperature is a direct measure of electron heating in QCL devices, and it is important to study how the electron temperature varies with the operating conditions. The elevated electron temperature is a clear fingerprint of a strong hot-electron regime: the electron system is not able to dissipate (via optical-phonon emission) the relatively large amount of energy provided by the applied bias. This electron heating in QCL devices has already been observed in experiment [61]. In Fig. 22, the electron temperature is plotted as a function of the current density for the 33% (a) and 45% (b) QCLs. It is clear that,

X. Gao, D. Botez, and I. Knezevic, "Multivalley simulation and design of quantum cascade lasers,"
in Encyclopedia of Nanoscience and Nanotechnology, Edited by H. S. Nalwa, American Scientific Publishers, in press. (2008)

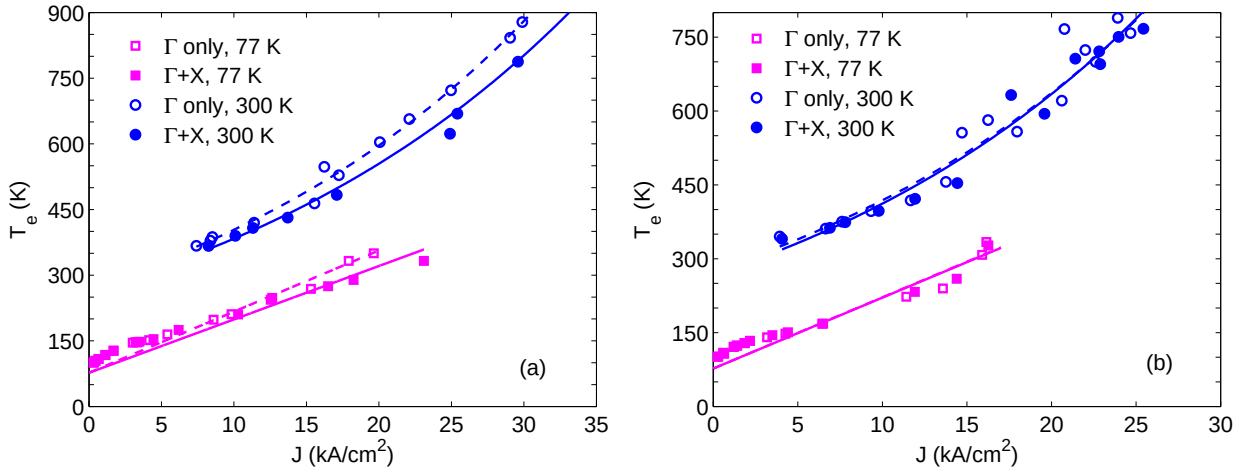

FIG. 22. Electron temperature vs current density at the lattice temperatures of 77 K and 300 K, with and without X-valley transport, for the 33% (a) and 45% (b) QCLs. The magenta lines are least-square linear fits ($T_e = T_l + \alpha_{e-l}J$) to the data. The blue curves are guides for the eyes.

in both QCLs, the temperature of the electron ensemble is much higher than the lattice temperature. At the low lattice temperature of 77 K, the electron temperature shows good linear relation with the current density in both lasers. The linearity can be described in the form of $T_e = T + \alpha_{e-l}J$, where T is the lattice temperature, and α_{e-l} is the electron temperature-current density coupling constant and can be obtained by least-square linear fits to the data. In the 33% QCL, the coupling constant α_{e-l} is calculated to be 14.0 K cm^2/kA for the case without X-valley transport, and 12.2 K/kA cm^{-2} for the case with X-valley transport. The latter is slightly smaller because the electrons lost to the X valleys have a heavier effective mass and thus a smaller kinetic energy. In the 45% QCL, the coupling constants are identical for the two cases (i.e., with and without X-valley transport) and equal to 14.4 K/kA cm^{-2}, because the electron loss to the X valleys is so small in the considered current density range that the heavier X-valley electrons are only a negligible portion of the whole electron ensemble. The linear dependence of the electron temperature on the current density was also obtained by Harrison *et al.* [93]. At the high lattice temperature of 300 K, the increase of the electron temperature with the current density becomes more non-linear in both QCLs. It is noted that at 300 K, in the 33% QCL, the difference in electron temperature between the two cases of with and without X-valley transport becomes more evident, but this difference is still negligible in the 45% case. The reason is that the 33%

X. Gao, D. Botez, and I. Knezevic, "Multivalley simulation and design of quantum cascade lasers,"
in Encyclopedia of Nanoscience and Nanotechnology, Edited by H. S. Nalwa, American Scientific Publishers, in press. (2008)

QCL has large carrier leakage to the X valleys at room temperature as explained in Sec. III A, and once carriers leak into the X valleys, they become heavier due to the larger X-valley effective mass, so that the average carrier kinetic energy decreases, meaning a lower electron temperature.

IV. DESIGN AND OPTIMIZATION OF 6.7 μm DEEP-ACTIVE-WELL GAAS-BASED QCLS

The GaAs/$Al_{0.45}Ga_{0.55}$As quantum cascade laser by Page *et al.* [31], emitting at 9.4 μm, has shown the best device performance so far among GaAs-based mid-infrared QCLs. It can achieve pulsed room-temperature operation and operate in continuous mode up to 150 K [36]. As described in the previous section, the superior performance of this particular design is due to the relatively large (370 meV) Γ-point conduction band offset between the wells and barriers, which minimizes the leakage arising from the scattering of carriers from the injector states to the next-stage Γ-continuum states [22], and also indirectly results in very small leakage to the X valleys even at room temperature [57, 58].

To decrease the wavelength of GaAs/Al_xGa_{1-x}As QCLs below 9 μm, one alternative is increasing the Al content in order to increase the Γ-point conduction band offset between the wells and the barriers. It is known that using 100% Al in the barriers (i.e., AlAs barriers) maximizes the conduction band discontinuity (∼1 eV). Wilson *et al.* [39] have shown that, in GaAs/AlAs QCLs incorporating a single injection barrier, once the upper lasing level becomes aligned with the lowest X-valley state of the injection barrier, lasing is suppressed due to intervalley (Γ-X) electron transfer, which limits the emission wavelengths to above 8 μm. Utilizing a double injection barrier [39], however, reduced the emission wavelength to 7.3 μm, with pulsed lasing observed only at cryogenic temperatures. In order to increase the operating temperature of GaAs/AlAs QCLs at these shorter wavelengths, Carder *et al.* [40] deposited InAs monolayers in the active quantum wells of a GaAs/AlAs QCL, and achieved room-temperature pulsed lasing at 8.5 μm. This technique of depositing InAs monolayers was also used in reducing the emission wavelength of the GaAs/$Al_{0.33}Ga_{0.67}$As QCL from 9.4 μm [28] to 7.4 μm [25], and the lasing was observed at 15 K in pulsed mode.

Recently, we proposed and optimized [94, 95] a deep-active-well GaAs QCL design that emits at 6.7 μm, the shortest room-temperature lasing wavelength projected to date for

X. Gao, D. Botez, and I. Knezevic, "Multivalley simulation and design of quantum cascade lasers,"
in Encyclopedia of Nanoscience and Nanotechnology, Edited by H. S. Nalwa, American Scientific Publishers, in press. (2008)

GaAs-based QCLs. This design utilizes compressively-strained $In_{0.1}Ga_{0.9}As$ in the active wells, GaAs in the injector wells, $Al_{0.45}Ga_{0.55}As$ in the barriers, and tensiley-strained $GaAs_{0.6}P_{0.4}$ in a layer adjacent to the injection barrier. The multivalley Monte Carlo (MMC) simulator described in Sec. II was employed to simulate the performance of three deep-active-well QCL structures (referred to as A, B, C) with different injector layer sequence. Their active-region layer thicknesses were all designed to lase around 6.7 μm. The unique inclusion of both Γ- and X-valley transport allows for identifying the issues associated with a particular structure. Simulation results from the first two structures A and B directly provide physical insights into obtaining an optimized injector layer sequence for both low- and room-temperature lasing operation. The optimized structure C was predicted to have threshold-current densities of 5 kA/cm^2 at 77 K and 14 kA/cm^2 at 300 K, similar to the experimental values obtained for the 9.4 μm GaAs QCL [31]. Furthermore, the electron temperature at 300 K lattice temperature is similar to that of the 9.4 μm device.

A. The Deep-Active-Well Design

The concept of utilizing deep wells in the active region (strained $In_xGa_{1-x}As$ active wells in GaAs-based devices) in order to significantly shorten the emission wavelength was demonstrated on single-stage $In_{0.3}Ga_{0.7}As/GaAs/Al_{0.7}Ga_{0.3}As$ devices, which provided strong room-temperature electroluminescence at 4.7 μm [96] and were not strain compensated. A similar concept was applied to the not-strain-compensated, deep-active-well $In_{0.04}Ga_{0.96}As/GaAs/Al_{0.33}Ga_{0.67}As$ devices [97], emitting at 10.4 μm and 9.45 μm up to a maximum temperature of 200 K.

Our proposed laser structure employs the conventional three-well active region design [31], but utilizes strained $In_{0.1}Ga_{0.9}As$ in the two wide active QWs to achieve a room-temperature emission wavelength below 7 μm, with the strain compensated in the injector of each stage. The calculated conduction band profile and the moduli squared of the relevant Γ- and X-valley wavefunctions in two adjacent stages for the optimized structure C are depicted in Fig. 23, where the Γ-states are solved for using the $\mathbf{k}\cdot\mathbf{p}$ method and the X-states are obtained within the effective mass framework, as described in Sec. II. The layer sequence in one stage (in Å) of structure C starting from the $GaAs_{0.6}P_{0.4}$ barrier step on the left is ***20***, **32**, 12, **11**, {48}, **11**, {40}, **28**, 34, **15**, 30, **16**, 28, **18**, 25, **20**, 19. The bold italic script denotes the

X. Gao, D. Botez, and I. Knezevic, "Multivalley simulation and design of quantum cascade lasers,"
in Encyclopedia of Nanoscience and Nanotechnology, Edited by H. S. Nalwa, American Scientific Publishers, in press. (2008)

$GaAs_{0.6}P_{0.4}$ barrier step, the bold script the $Al_{0.45}Ga_{0.55}As$ barriers, the normal script the GaAs wells, and the values in curly brackets indicate the $In_{0.1}Ga_{0.9}As$ wells. The underlined layers are n-type doped with a sheet doping density of $N_s = 3.8 \times 10^{11}$ cm^{-2}. Structures A and B have the same doping density and active-region layer thickness as structure C, but with different injector layer thickness. The layer sequence of structure A is ***20***, **28**, 12, **11**, {48}, **11**, {40}, **28**, 38, **13**, 34, **14**, 25, **16**, 22, **17**, 17, and structure B has ***20***, **28**, 12, **11**, {48}, **11**, {40}, **28**, 38, **13**, 30, **14**, 30, **16**, 27, **17**, 25. As will be shown in Sec. IV B, simulation results from structures A and B directly help to optimize the injector layer sequence of structure C.

To compensate the compressive strain in the $In_{0.1}Ga_{0.9}As$ layers, one $GaAs_{0.6}P_{0.4}$ layer is added just before the injection barrier. The parallel component (ϵ_{xx}, in the plane perpendicular to the growth direction) of the strain tensor for the compressively-strained $In_{0.1}Ga_{0.9}As$ well is $\epsilon_w = -0.71\%$, and for the tensilely-strained $GaAs_{0.6}P_{0.4}$ barrier it is $\epsilon_b = +1.46\%$. The ratio of the thicknesses of the $In_{0.1}Ga_{0.9}As$ layers to the $GaAs_{0.6}P_{0.4}$ barrier is designed such that the average in-plane lattice constant ($a_\parallel$) in one stage is nearly equal to that of the GaAs substrate (5.653 Å). $a_\parallel$ is calculated within the model solid theory [98], i.e., $a_\parallel = \sum_i a_i G_i d_i / \sum_i G_i d_i$, where a_i and d_i are the unstrained lattice constant and the thickness of the ith layer, respectively, and G_i is the ith layer elastic shear modulus. For the optimized structure C, the calculated $a_\parallel$ equals to 5.657 Å, resulting in a net compressive strain of 0.07% in one stage.

The Γ-point conduction band offset between the strained $In_{0.1}Ga_{0.9}As$ well and the $Al_{0.45}Ga_{0.55}As$ barrier (the strain-induced band offset is included using the model-solid theory [98]) is 45 meV larger than that between the GaAs well and the $Al_{0.45}Ga_{0.55}As$ barrier. The radiative transition energy (3→2) is 185 meV, about 54 meV larger than 131 meV for the 9.4 μm QCL of Page *et al.* [31]. While the upper lasing level of our proposed structure is 20 meV closer to the Γ-band edge due to the thinner active-region wells, the remaining 34 meV increase in the transition energy is thanks to the deep wells in the active region. The thinner active wells also enable the lowest Γ-continuum level (level 4 in Fig. 23) to shift up by 15 meV, which helps to reduce the leakage to the continuum [58]. The calculated lifetime due to the electron-LO interaction for level 3 is $\tau_3 = 1.5$ ps, where $1/\tau_3 = 1/\tau_{32} + 1/\tau_{31}$, $\tau_{32} = 2.5$ ps, and $\tau_{31} = 3.8$ ps. The lifetime of level 2 is $\tau_2 \approx \tau_{21} = 0.3$ ps. The dipole matrix element $\langle z_{32} \rangle$ is calculated to be 1.5 nm. These calculations were done at F = 55 kV/cm,

X. Gao, D. Botez, and I. Knezevic, "Multivalley simulation and design of quantum cascade lasers,"
in Encyclopedia of Nanoscience and Nanotechnology, Edited by H. S. Nalwa, American Scientific Publishers, in press. (2008)

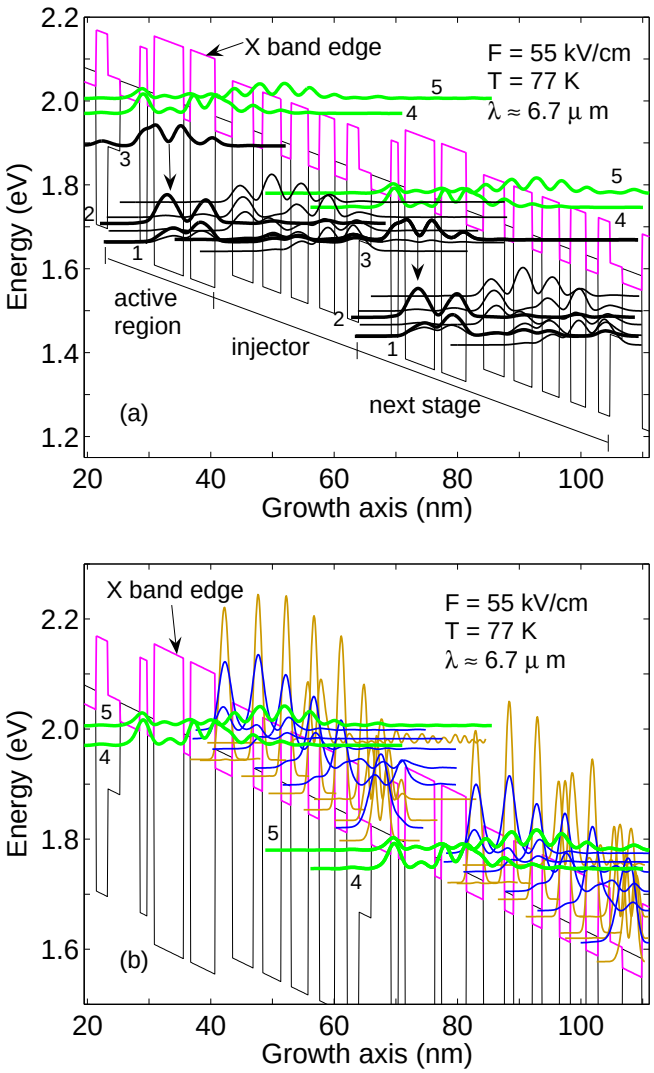

FIG. 23. Calculated conduction band profile and the moduli squared of the relevant Γ- and X-valley wavefunctions in two adjacent stages for the optimized structure C. (a) The bold black lines denote the active lasing levels 3, 2, and 1. The thin black lines are the injector miniband states, and the bold green lines are the Γ-continuum states. The vertical arrow denotes the lasing transition. (b) The thin blue lines are the (degenerate) X_x- and X_y-states, and the yellow ones are the X_z-states, together with the Γ-continuum states.

close to the estimated threshold field of F = 58 kV/cm and T = 77 K. The lifetimes and matrix element are similar to those of the 9.4 μm QCL (τ_3 = 1.4 ps, τ_2 = 0.3 ps, and $\langle z_{32} \rangle$ = 1.7 nm) [31].

As mentioned earlier, the three structures (A, B, C) all have the same active-region layer sequence, which is designed to obtain the lifetimes of the lasing levels and the dipole matrix

X. Gao, D. Botez, and I. Knezevic, "Multivalley simulation and design of quantum cascade lasers,"
in Encyclopedia of Nanoscience and Nanotechnology, Edited by H. S. Nalwa, American Scientific Publishers, in press. (2008)

element similar to those of the state-of-the-art 9.4 μm GaAs QCL [31], but with a much shorter wavelength of 6.7 μm enabled by the use of deep active wells. Apart from designing the active region, we have to design and optimize the thickness of layers in the injector for desired device performance. Our goal is to obtain an optimized injector layer sequence so that the resulting structure can achieve sufficient optical gain for lasing emission at both low and room temperatures. This is where the MMC simulator developed plays a crucial role. The injector of the initial structure A is modified from the 9.4 μm QCL. The MMC simulation of this structure clearly reveals that structure A is incapable of lasing action at 300 K. With an improved injector design, structure B shows better room-temperature performance, but sacrifices the gain at the low temperature of 77 K. Identification of issues associated with structures A and B directly helps to optimize the injector of structure C, which demonstrates adequate gain at both 77 K and 300 K.

B. Injector Optimization of Deep-Active-Well QCLs

This subsection will show how we can take advantage of the multivalley Monte Carlo (MMC) simulator presented in Sec. II to optimize the injector layer sequence for obtaining the desired structure C. The MMC simulation can theoretically characterize the output characteristics of GaAs QCL structures, namely, it yields the current density J, the electron density in each subband, and the electron temperature T_e for a given electric field. The modal gain G_m can then be calculated from the population inversion (i.e., the electron density difference between the upper and lower lasing levels) and the waveguide confinement factor Γ_w. Based on the estimate of the waveguide losses α_w and mirror losses α_m, a realistic threshold-current density can be determined.

The modal gain G_m is proportional to the population inversion Δn and is given under the steady-state conditions by [54]

$$G_m = \frac{4\pi e^2}{\varepsilon_0 \underline{n}} \frac{\langle z_{32} \rangle^2}{2\gamma_{32} L_p \lambda} \Gamma_w \Delta n = g \Gamma_w J, \tag{39}$$

where e is the electron charge, ε_0 is the vacuum dielectric permittivity, $\underline{n}$ is the optical mode refractive index, $2\gamma_{32}$ is the full width at half maximum of the electroluminescent spectrum below threshold, L_p is the length of one stage (active region + injector), λ is the laser emission wavelength, $\langle z_{32} \rangle$ is the dipole matrix element, Γ_w is the waveguide confinement

X. Gao, D. Botez, and I. Knezevic, "Multivalley simulation and design of quantum cascade lasers,"
in Encyclopedia of Nanoscience and Nanotechnology, Edited by H. S. Nalwa, American Scientific Publishers, in press. (2008)

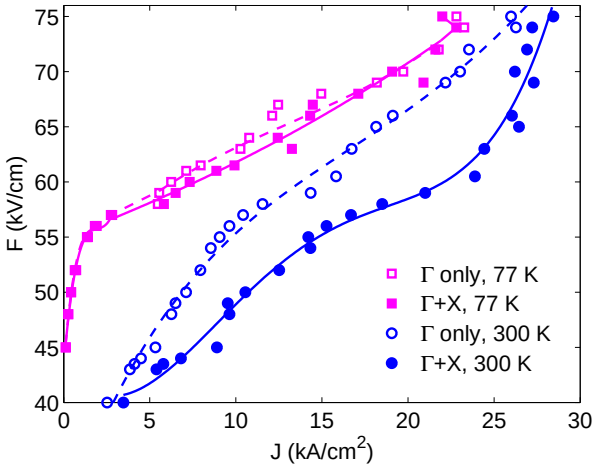

FIG. 24. Electric field vs current density characteristics at the lattice temperatures of 77 K and 300 K, with and without the X-valley transport included, for the QCL structure A. Dashed and solid curves are least-square polynomial fits to the calculated data, intended to guide the eyes.

factor, and g is the local gain coefficient. The waveguide is designed such that the 25-stage QCL structure is sandwiched between two 1.3 μm-thick, low-doped (4×10^{16} cm^{-3}) GaAs layers. (Only 25 stages are expected to be grown considering that the residual strain may cause dislocations in the crystal lattice.) The GaAs layers are followed by 0.3 μm-thick $Al_{0.9}Ga_{0.1}As$ cladding layers (doped to 1×10^{18} cm^{-3}) and 1 μm-thick GaAs layers (doped to 4×10^{16} cm^{-3}). On one side of the above layer sequence is a 1 μm-thick, highly doped (5×10^{18} cm^{-3}) GaAs contact layer, and on the other side is a 1 μm-thick, highly doped (5×10^{18} cm^{-3}) GaAs cladding layer and the GaAs substrate. The parameters of the designed waveguide are calculated to be $\Gamma_w = 33\%$, $\underline{n} = 3.21$, and $\alpha_w = 15$ cm^{-1}. Even with fewer stages, the addition of $Al_{0.9}Ga_{0.1}As$ cladding layers allows for a Γ_w value higher than 28%, the value used in the 36-stage 9.4 μm QCL [31]. The calculated waveguide losses are lower than those of the 9.4 μm QCL (20 cm^{-1}), due to a reduction in the free-carrier absorption with decreasing wavelength [99].

We started with the initial structure A whose injector layer sequence was modified from that of the state-of-the-art 9.4 μm QCL [31]. Without the MMC simulation, it was unknown whether this structure has the desired threshold current density or optical modal gain, so it is crucial to simulate the performance of a particular structure before carrying out any experiment. Figure 24 shows the electric field vs current density characteristics for the QCL

X. Gao, D. Botez, and I. Knezevic, "Multivalley simulation and design of quantum cascade lasers,"
in Encyclopedia of Nanoscience and Nanotechnology, Edited by H. S. Nalwa, American Scientific Publishers, in press. (2008)

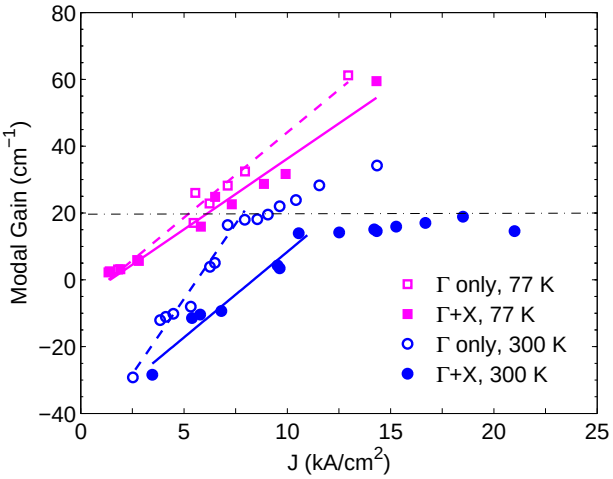

FIG. 25. Modal gain vs current density at the lattice temperatures of 77 K and 300 K, with and without the X-valley transport included, for the QCL structure A. Dashed and solid lines are least-square linear fits to the data, and the horizontal dash-dotted line indicates the calculated total losses ($\alpha_w + \alpha_m = 19$ cm^{-1}) of the improved waveguide.

structure A. The computed J values with the X-valley transport included account for the leakage currents through the next-stage Γ_c states and the X-valley states [58]. At the low lattice temperature of 77 K, the current density is nearly the same for the two cases of with and without the X-valley, whereas the increase in the current density due to the X-valley leakage is dramatic at room temperature. The modal gain as a function of the current density is shown in Fig. 25, where the gain was calculated with $L_p = 39.4$ nm, $\lambda = 6.7$ μm, $\langle z_{32} \rangle = 1.4$ nm, $2\gamma_{32} = 12$ meV at 77 K, and $2\gamma_{32} = 22$ meV at 300 K ($2\gamma_{32}$ values were taken from Ref. [31]). In order to observe lasing in a QCL device, the modal gain must be higher than the total waveguide losses. Structure A shows very high gain at 77 K, much higher than the losses. However, at 300 K, although the gain obtained without the X valleys is above the loss line, in reality, carrier loss to the X valleys largely reduces the population inversion, as shown in Fig. 26, so that the actual gain with the X valleys saturates below the total waveguide losses. Overall, structure A has two problems, namely, large X-valley leakage current and insufficient modal gain at room temperature.

The X-valley leakage was shown to take place through the three-step process described in Sec. III A, and significant overlap between the injector miniband states and the next-stage Γ_c-states results in not only direct carrier loss to the Γ_c-states, but also indirect high current

X. Gao, D. Botez, and I. Knezevic, "Multivalley simulation and design of quantum cascade lasers,"
in Encyclopedia of Nanoscience and Nanotechnology, Edited by H. S. Nalwa, American Scientific Publishers, in press. (2008)

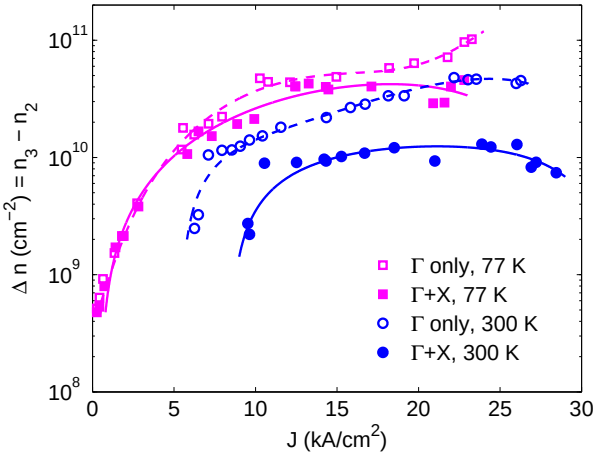

FIG. 26. Population inversion vs current density at the lattice temperatures of 77 K and 300 K, with and without the X-valley transport included, for the QCL structure A.

through the X-valley states by the three-step process. As can be seen from Fig. 27a, in structure A, the next-stage Γ_c-states (green) are indeed strongly coupled to the injector miniband (including level 2) (black), especially to the top two injector states. In fact, in the field range of 50-70 kV/cm, the two next-stage Γ_c-states become nearly resonant with the top two injector states; this leads to a large X-valley leakage current in that range of fields at 300 K, as seen in the F vs J characteristics (Fig. 24), and consequently to large carrier loss to the X valleys. Therefore, the strong coupling between the injector states and the next-stage Γ_c-states directly results in the large X-valley leakage and inadequate gain at room temperature in structure A.

In order to reduce the coupling of the injector states with the Γ_c-states, the injector layer sequence of structure A needs to be modified. The first improved QCL design is referred to as structure B. In structure B, the thicknesses of three injector wells on the left of the injection barrier are increased by a few angstroms with respect to structure A, so that the injector top two levels are brought down in energy and their wavefunction maxima are shifted away from the continuum, as shown in Fig. 27b. By comparing Fig. 27b with Fig. 27a, one can immediately see that structure B indeed shows smaller overlap between the injector and the Γ_c wavefunctions than in A. In Fig. 28, the electric field vs current density is compared for structures B and A at the lattice temperature of 300 K. The X-valley leakage current in structure B, i.e., the difference between the blue solid and dashed curves, does become smaller than in A, due to a decreased coupling of the injector states with the Γ_c-states. The

X. Gao, D. Botez, and I. Knezevic, "Multivalley simulation and design of quantum cascade lasers,"
in Encyclopedia of Nanoscience and Nanotechnology, Edited by H. S. Nalwa, American Scientific Publishers, in press. (2008)

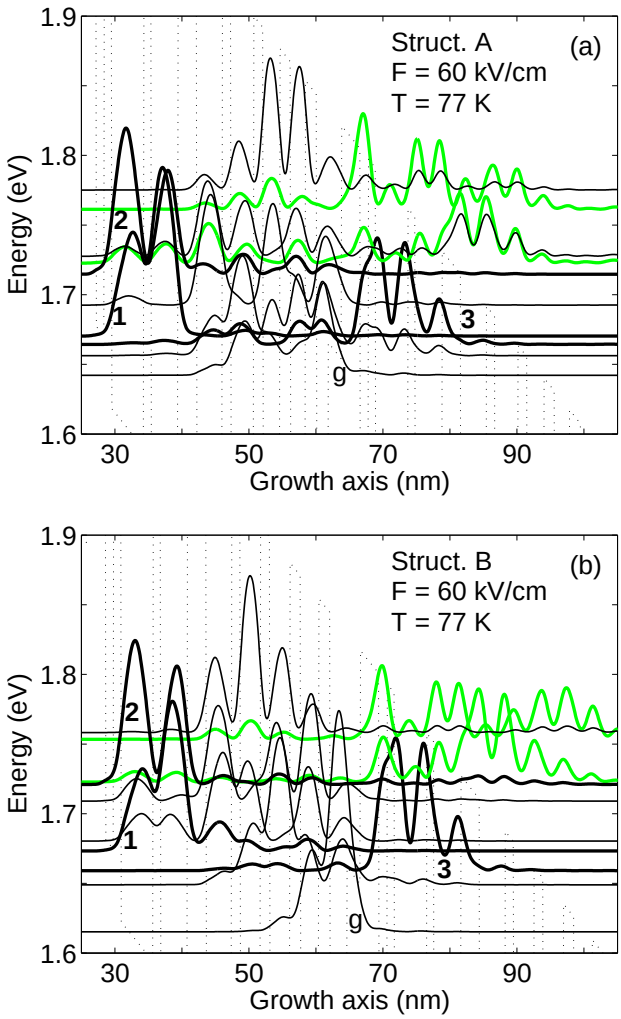

FIG. 27. Zoom-in of the wavefunction moduli squared of the injector miniband and the next-stage Γ-continuum (Γ_c) states in the initial structure A (a) and the improved structure B (b). Thin black curves denote the injector states, while the green ones are the next-stage Γ_c-states. The lasing levels are shown in bold black, where 2 indicates the lower lasing level, 1 the active ground state, and 3 the upper lasing level in the next stage.

modal gain vs current density at 300 K is shown in Fig. 29 for the two structures. The modal gain of structure B was calculated with $L_p = 40.8$ nm, $\lambda = 6.8$ μm, $\langle z_{32} \rangle = 1.6$ nm. The waveguide parameters are identical to those used for structure A. The dipole matrix element $\langle z_{32} \rangle$ in structure B is larger than in A [$\langle z_{32} \rangle = 1.4$ nm] thanks to better localization of the lasing levels, which further enhances the modal gain. Structure B indeed shows improved room-temperature gain compared to A, and the actual gain with the X-valley transport is

X. Gao, D. Botez, and I. Knezevic, "Multivalley simulation and design of quantum cascade lasers,"
in Encyclopedia of Nanoscience and Nanotechnology, Edited by H. S. Nalwa, American Scientific Publishers, in press. (2008)

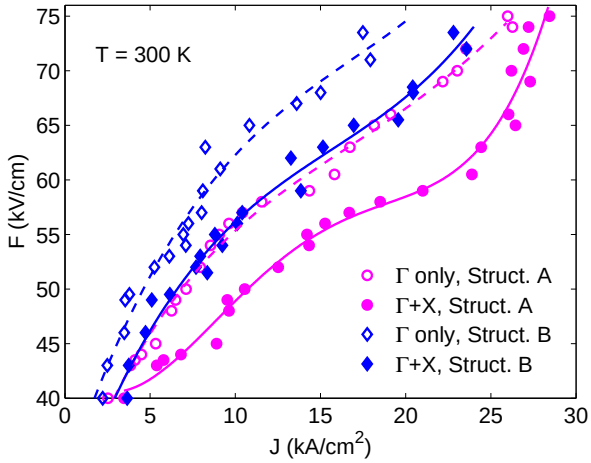

FIG. 28. Electric field vs current density characteristics at 300 K lattice temperature, with and without the X-valley transport included, for structures A and B. Dashed and solid curves are least-square polynomial fits to the calculated data, intended to guide the eyes.

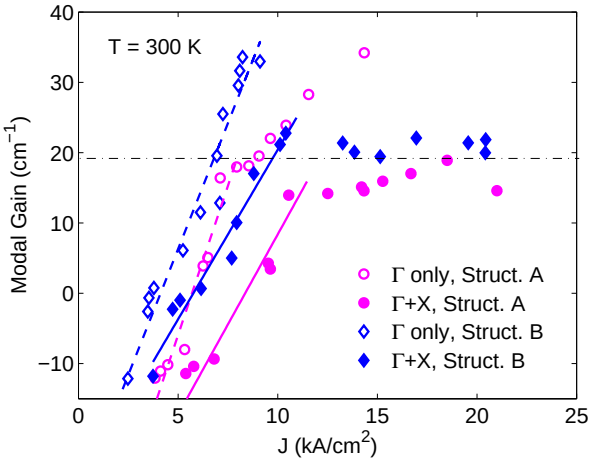

FIG. 29. Modal gain vs current density at 300 K lattice temperature, with and without the X-valley transport included, for structures A and B. Dashed and solid lines are least-square linear fits to the data, and the horizontal dash-dotted line indicates the calculated waveguide losses ($\alpha_w + \alpha_m$ = 19 cm^{-1}).

just enough to overcome the total losses.

However, the low-temperature output characteristics of structure B is not as good as that of structure A. The electric field vs current density at 77 K is plotted in Fig. 30 for structures A and B. The current density in structure B is rather small even at fields above 70 kV/cm. The low J leads to a very low population inversion, resulting in insufficient modal gain (<

X. Gao, D. Botez, and I. Knezevic, "Multivalley simulation and design of quantum cascade lasers,"
in Encyclopedia of Nanoscience and Nanotechnology, Edited by H. S. Nalwa, American Scientific Publishers, in press. (2008)

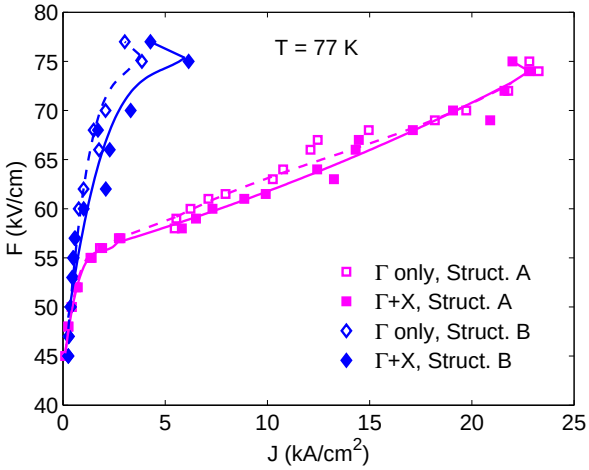

FIG. 30. Electric field vs current density at 77 K lattice temperature, with and without the X-valley transport included, for structures A and B. Dashed and solid curves are least-square polynomial fits to the calculated data, intended to guide the eyes.

15 cm^{-1}) in B at 77 K. The reason is that, in structure B, the next-stage upper lasing level (level 3 in Fig. 27b) is more weakly coupled to the injector ground state (level g) and far above in energy level (Fig. 27b), compared to structure A (Fig. 27a). At the low temperature of 77 K, the weak coupling and the large energy separation between levels 3 and g cause most electrons to stay in level g (injector ground state), e.g., the electron density in level 3 is only 3% of that in level g at $F = 70$ kV/cm, but this number is 78% in structure A. This electron accumulation in the injector ground state results in very poor injection efficiency. In contrast, at 300 K, the electrons are energetic and distribute among all the Γ-subbands due to active phonons, and thus the modal gain is still sufficient for lasing.

Identification of issues associated with structures A and B directly helps the optimization of structure C. The injector layer sequence of structure C was designed such that not only the coupling between the injector states and the next-stage Γ_c-states is reduced, but also the upper lasing level has a good wavefunction overlap and a small energy difference with the injector ground state, as seen in Fig. 31. The modal gain with the X-valley transport included is compared in Fig. 32 for the three structures A, B, and C. It is clear that structure C shows the highest modal gain among the three structures at 300 K and also excellent gain at 77 K. Similar to structures A and B, the modal gain of structure C at 300 K saturates in the high-J range (above 17 kA/cm^2) due to carrier loss to the X valleys [59] that results in reduced population inversion. Nevertheless, the saturation gain (≈ 25 cm^{-1}) is sufficiently

X. Gao, D. Botez, and I. Knezevic, "Multivalley simulation and design of quantum cascade lasers,"
in Encyclopedia of Nanoscience and Nanotechnology, Edited by H. S. Nalwa, American Scientific Publishers, in press. (2008)

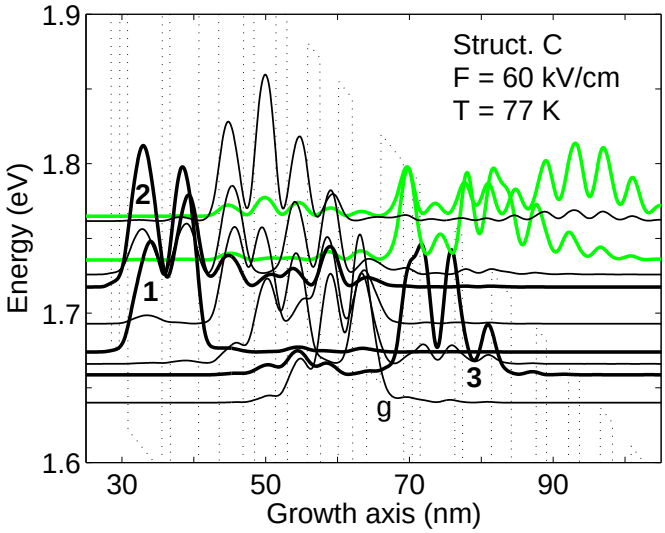

FIG. 31. Blow-up of the wavefunction moduli squared of the injector miniband and the next-stage Γ-continuum (Γ_c) states in the optimized structure C. Notation is the same as in Fig. 27.

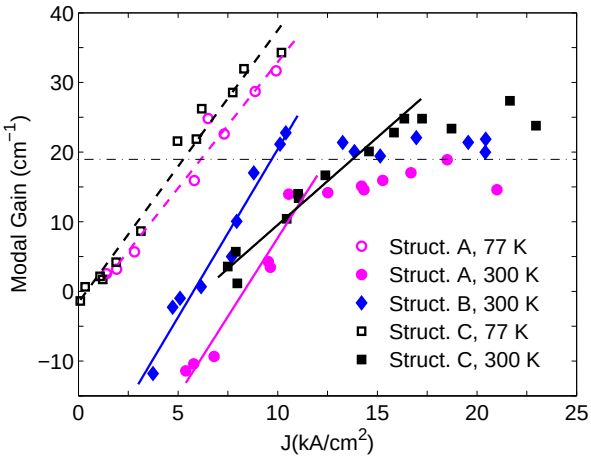

FIG. 32. Modal gain vs current density at the lattice temperatures of 77 K and 300 K, with the X-valley transport included, for structures A, B and C.

high with respect to the total losses of 19 cm^{-1} to deem room-temperature operation of the optimized structure C quite feasible.

C. Performance Comparison with the State-of-the-Art 9.4 μm QCL

In this subsection, the performance of the optimized 6.7 μm structure C is compared with that of the state-of-the-art 9.4 μm QCL [31] (the 45% QCL discussed in Sec. III). Figure

X. Gao, D. Botez, and I. Knezevic, "Multivalley simulation and design of quantum cascade lasers,"
in Encyclopedia of Nanoscience and Nanotechnology, Edited by H. S. Nalwa, American Scientific Publishers, in press. (2008)

33 presents the electric field vs current density behavior for the optimized 6.7 μm QCL structure C (a) and the 9.4 μm QCL of Ref.[31] (b), at the lattice temperatures of 77 K and 300 K, with and without the X-valley leakage. At both 77 K and 300 K, the X-valley leakage current in the 6.7 μm structure C is higher than in the 9.4 μm QCL. (At 77 K, the leakage in both structures is fairly low, predominantly due to a low number of intervalley phonons.) As seen in Fig. 34, the reason is the difference in the wavefunction overlap between the injector miniband (black) and the next-stage Γ-continuum states (green): the structure of Page *et al.* has a remarkably low overlap (Fig. 34b) between the injector miniband and the next-stage Γ_c-states; in the 6.7 μm structure C, however, this overlap is greater (Fig. 34a) due to the wavelength reduction, which results in a higher X-valley leakage current for a given electric field, especially at 300 K, through the X-leakage mechanism described in Sec. III A. However, even with more X-valley leakage, the total current at a given field is significantly lower in the 6.7 μm structure C than in the 9.4 μm QCL, owing to the design modification necessary for the wavelength shortening.

Furthermore, the 6.7 μm structure C demonstrates gain coefficients and threshold current densities similar to those of the 9.4 μm QCL. The gain coefficient g in Eq. (39) can be obtained for the structure C: $g = 11.8$ cm/kA at 77 K and $g = 7.6$ cm/kA at 300 K, values close to the calculations by Indjin *et al.* [60] for the 9.4 μm QCL ($g = 11$ cm/kA at 77 K and $g = 5$ cm/kA at 300 K). Given the calculated waveguide total losses ($\alpha_m + \alpha_w = 19$ cm^{-1}, $\alpha_m = 4$ cm^{-1}), since the threshold field was unknown for the structure C, the threshold-current density $J_{\rm th}$ can be defined at which the linear fit of optical modal gain intersects with the loss line in the G_m vs J relation. From Fig. 32, $J_{\rm th}$ is found to be 5 kA/cm^2 at 77 K and 14 kA/cm^2 at 300 K. (Structure B has $J_{\rm th} = 9.5$ kA/cm^2 at 300 K due to the smaller currents in Fig. 32 and higher $\langle z_{32} \rangle = 1.6$ nm.) For the 9.4 μm QCL, the calculated $J_{\rm th}$ has the values of 2.9 kA/cm^2 at 77 K and 14.4 kA/cm^2 at 300 K, which are listed in Table II, while the experimental values are 4 kA/cm^2 (77 K) and 16.7 kA/cm^2 (300 K), respectively. By comparison, it is clear that the threshold-current densities of the optimized 6.7 μm structure C are comparable to those of the 9.4 μm QCL.

The electron temperature T_e, generally higher than the lattice temperature, characterizes the degree of electron heating in a QCL device. With relatively high carrier densities per subband, distribution function within each subband i becomes Maxwellian [$f(E_{k,i}) \sim \exp(-E_{k,i}/k_B T_e)$] as a result of efficient carrier-carrier intrasubband scattering

X. Gao, D. Botez, and I. Knezevic, "Multivalley simulation and design of quantum cascade lasers,"
in Encyclopedia of Nanoscience and Nanotechnology, Edited by H. S. Nalwa, American Scientific Publishers, in press. (2008)

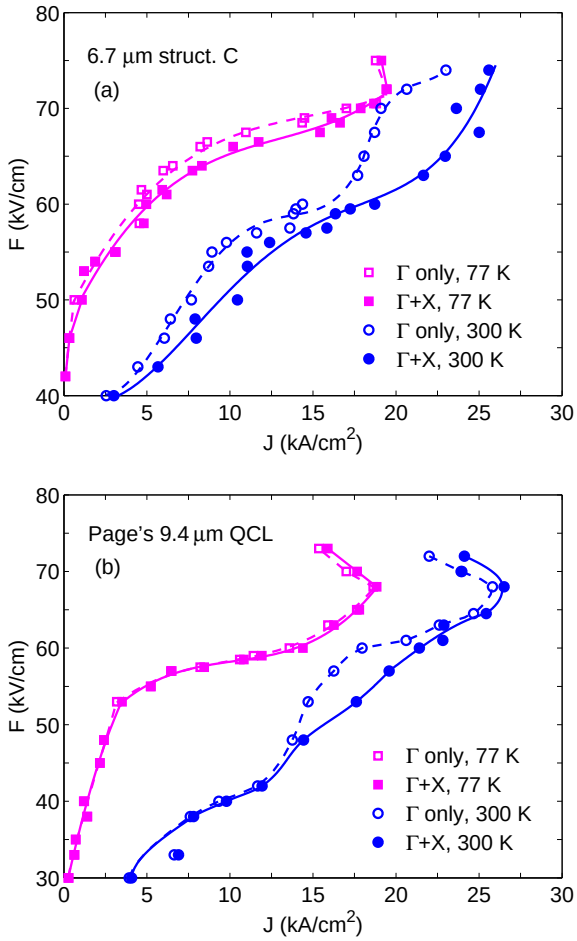

FIG. 33. Electric field vs current density for the optimized 6.7 μm structure C (a) and the 9.4 μm QCL from Ref. [31] (b), at the lattice temperatures of 77 K and 300 K, with and without the X-valley transport included. Dashed and solid curves are polynomial fits to the data points. Reprinted with permission from [94], X. Gao, M. D'Souza, D. Botez, and I. Knezevic, *J. Appl. Phys.* 102, 113107 (2007). © 2007, American Institute of Physics.

(intersubband scattering, both electron-electron and electron-phonon, are less efficient). The electronic temperature T_e is approximately the same for all subbands [91, 92]. In the Monte Carlo simulation, the electron temperature can be obtained either from the thermalized distribution function or from the ensemble average of the carrier kinetic energy $T_e = \langle E_k \rangle / k_B$. These two approaches are equivalent as long as the distribution is Maxwellian, as discussed in Sec. III B, and in this work the latter approach was used.

Figure 35 shows the electron temperature T_e as a function of the current density J (a) and as a function of the input electrical power density P_e (b), for the optimized 6.7 μm

X. Gao, D. Botez, and I. Knezevic, "Multivalley simulation and design of quantum cascade lasers,"
in Encyclopedia of Nanoscience and Nanotechnology, Edited by H. S. Nalwa, American Scientific Publishers, in press. (2008)

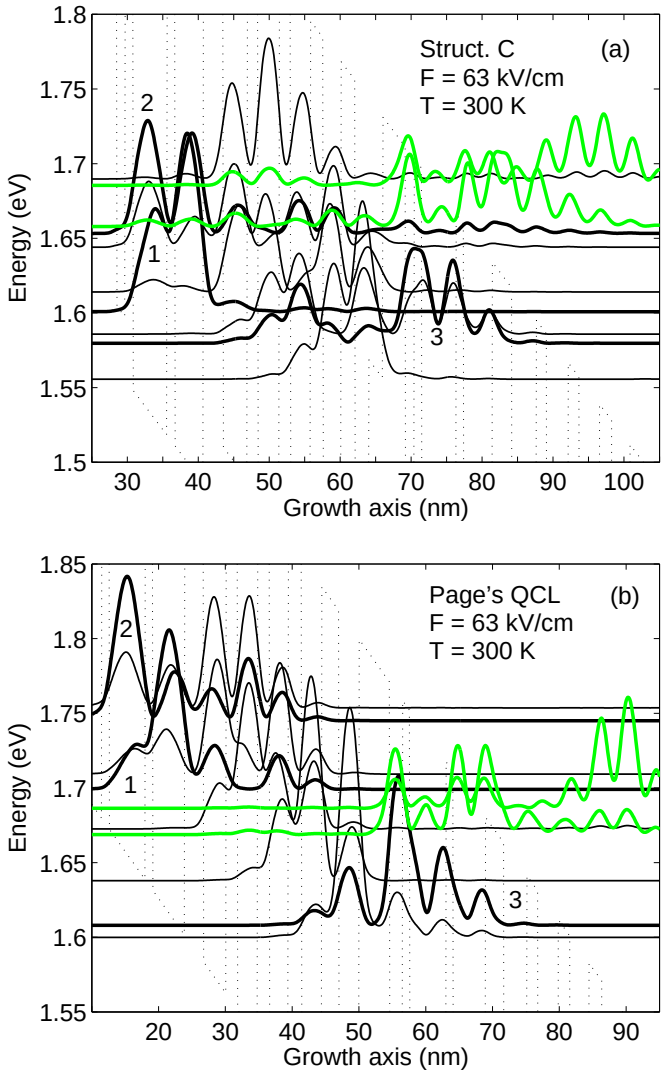

FIG. 34. Zoom-in of the wavefunction moduli squared of the injector miniband and the next-stage Γ-continuum (Γ_c) states in the optimized 6.7 μm structure C (a) and the 9.4 μm QCL from Ref. [31] (b), at the field of 63 kV/cm (above threshold for both structures). Thin black curves denote the injector states, while the green ones are the next-stage Γ_c-states. The lasing levels are shown in bold black, where 2 indicates the lower lasing level, 1 the active ground state, and 3 the upper lasing level in the next stage. Reprinted with permission from [94], X. Gao, M. D'Souza, D. Botez, and I. Knezevic, *J. Appl. Phys.* 102, 113107 (2007). © 2007, American Institute of Physics.

structure C and the 9.4 μm QCL [31], at the lattice temperature of 300 K. It is clear that the reduction in the room-temperature emission wavelength, provided by the proposed deep-active-well design, is achieved at no penalty in the electron heating: at threshold, the

X. Gao, D. Botez, and I. Knezevic, "Multivalley simulation and design of quantum cascade lasers,"
in Encyclopedia of Nanoscience and Nanotechnology, Edited by H. S. Nalwa, American Scientific Publishers, in press. (2008)

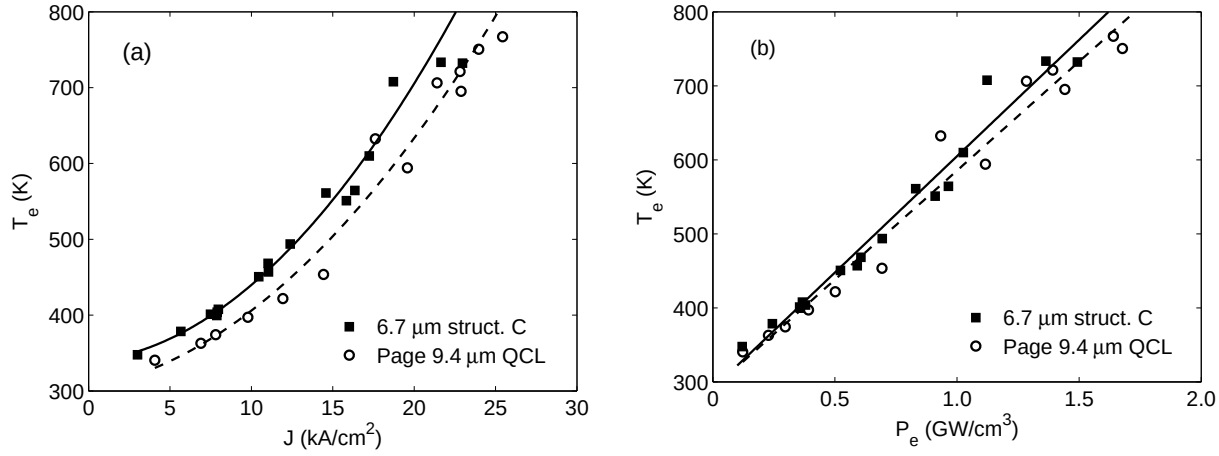

FIG. 35. Electron temperature T_e vs current density J (a) and vs input electrical power density P_e ($= JF$) (b), for the optimized 6.7 μm structure C and the 9.4 μm QCL, at the lattice temperature of 300 K. The lines are polynomial fits, intended to guide the eye. Reprinted with permission from [94], X. Gao, M. D'Souza, D. Botez, and I. Knezevic, *J. Appl. Phys.* 102, 113107 (2007). © 2007, American Institute of Physics.

electron temperatures are $T_e = 530$ K ($J_{\rm th} = 14$ kA/cm^2) for the 6.7 μm structure C, and $T_e = 544$ K ($J_{\rm th} = 16.7$ kA/cm^2) for the 9.4 μm QCL. (We find very little influence of the X-valley transport on the electron temperature up to very high electric fields, and therefore do not separate the curves with and without the X-valley transport. The reason is that the X-valley population is generally low and these X-subbands have low kinetic energy due to their larger effective mass up to high electric fields, as discussed in Sec. III B.)

In both structures, the variation of the electronic temperature with the current density is linear only for very low current densities (Fig. 35a), with the low-current electron-lattice coupling constant being $\lim_{J\to 0} \frac{T_e - T_L}{J} \approx 14$ K cm^2/kA for both devices. However, the variation of T_e with the power density ($P_e = JF$) obeys a quasi-linear law, even up to high power densities (Fig. 35b). This agrees with a simple energy-balance equation

$$nk_B \frac{d(T_e - T_L)}{dt} = JF - nk_B \frac{(T_e - T_L)}{\tau_E}, \tag{40}$$

where n is the total carrier density, and τ_E is an effective (ensemble averaged) energy relaxation time [62]. In the steady state, the above equation yields

$$T_e - T_L = \frac{\tau_E}{nk_B} JF, \tag{41}$$

X. Gao, D. Botez, and I. Knezevic, "Multivalley simulation and design of quantum cascade lasers,"
in Encyclopedia of Nanoscience and Nanotechnology, Edited by H. S. Nalwa, American Scientific Publishers, in press. (2008)

which is a simple, intuitive description of the linear behavior that we observe in the simulation (Fig. 35b).

V. PHONON CONFINEMENT IN GAAS QCLS

In the sections presented above, the electron-LO phonon scattering rates were calculated using the bulk GaAs phonon approximation. In general, transport simulations [43, 44, 48, 52, 59, 100] of QCLs assume electrons interacting with dispersionless bulk phonons of the well material, due to the simplicity of the scattering rate calculation under this approximation. However, it has been unclear whether the spatial confinement of phonons has a strong influence on the electron-LO phonon scattering strength in cascaded structures: on the one hand, Rücker *et al.* [82, 101] showed that phonon confinement has an insignificant effect on the scattering rate in single-well GaAs/AlGaAs structures, but is critical for interpreting the signals of time-resolved Raman spectroscopy [102]. Williams and Hu [103] also showed that the total phonon scattering rates including confinement in one stage (three quantum wells) of two GaAs/$Al_{0.3}Ga_{0.7}As$ THz QCLs are very close to those obtained using GaAs bulk phonons, thanks to wide wells and thin, low-Al barriers. On the other hand, calculations by Menon *et al.* [104] indicated that the scattering rate τ_{21} (levels 2 to 1) in a similar three-QW THz structure can be strongly enhanced due to phonon confinement, and Ref. [105] reported that, in step quantum-well structures using GaAs/$Al_{0.25}Ga_{0.75}As$/$Al_{0.4}Ga_{0.6}As$ materials, the scattering rates with phonon quantization are more than an order of magnitude greater than the bulk GaAs rate.

Furthermore, very little work has been done on incorporating phonon confinement in QCL transport calculations (beyond the scattering rate computation): notable work in this direction came from the University of Rome group [42, 106, 107], who focused on the electroluminescence spectra calculation in InGaAs/InAlAs superlattice QCLs (each period containing one barrier and one well) lattice-matched to InP substrates. The same group also reported calculation of the electron-LO phonon scattering rates with phonon quantization [108] for a GaAs/$Al_{0.45}Ga_{0.55}As$ 6.9 μm QCL structure consisting of triple-QW active regions, designed by Strasser *et al.* [27]. However, so far there has been no systematic account of the phonon confinement on the transport properties of GaAs-based QCLs, such as the current-field characteristics or population inversion.

X. Gao, D. Botez, and I. Knezevic, "Multivalley simulation and design of quantum cascade lasers,"
in Encyclopedia of Nanoscience and Nanotechnology, Edited by H. S. Nalwa, American Scientific Publishers, in press. (2008)

In this section, we provide a detailed account of the effects that phonon confinement has on the electron transport properties of mid-infrared, multiple-quantum-well, GaAs-based QCLs [109, 110]. The phonon quantization due to spatial confinement is treated within the macroscopic dielectric continuum model [111], where the LO phonons are classified as confined (CF) bulk-like modes and interface (IF) modes. The IF phonon spectra are obtained by using the transfer matrix method [112] with periodic boundary conditions [109]. The calculated CF and IF potentials are then utilized to evaluate both Γ- and X-valley electron transition rates due to the interaction with these phonon modes. Intravalley electron-IF, electron-CF, and electron-electron scattering, as well as intervalley scattering, are implemented in the multivalley Monte Carlo simulation of the deep-active-well optimized 6.7 μm structure C presented in Sec. IV.

A. Phonon Confinement Modeling

There are four macroscopic models that can treat the interaction of confined electrons with confined polar-optical phonons in III-V heterostructures: the dielectric continuum (DC) model [111, 113], the hydrodynamic (HD) model [114], the reformulated (RM) DC model [115, 116], and the hybrid model [117–119]. It was shown by Nash [118] that the first three models all produce the same scattering rates in a single GaAs/AlAs quantum well in the limit of dispersionless bulk phonons, provided that the modes in each model are mutually orthogonal and constitute a complete set. Constantinou and Ridley [119] found that the total scattering rates obtained by the hybrid model are reproduced to an excellent degree by the DC model, and are virtually insensitive to the bulk dispersion. Moreover, Rücker *et al.* [82] and Insook *et al.* [120] showed that the DC model accurately predicts the total scattering rates obtained by microscopic calculations. In view of the accuracy of the DC model in the scattering rate calculation and the relative simplicity of its implementation, the DC model has been widely used [103–105, 108, 112, 121] to treat phonon confinement in multiple-quantum-well (MQW) structures.

X. Gao, D. Botez, and I. Knezevic, "Multivalley simulation and design of quantum cascade lasers,"
in Encyclopedia of Nanoscience and Nanotechnology, Edited by H. S. Nalwa, American Scientific Publishers, in press. (2008)

TABLE III. Dielectric constants and optical phonon frequencies for the alloys used in the 6.7 μm QCL [94]. Reprinted with permission from [109], X. Gao, D. Botez, and I. Knezevic, *J. Appl. Phys.*, accepted (December, 2007). © 2007, American Institute of Physics.

	GaAs	AlAs	InAs	GaP	$Al_xGa_{1-x}As$ [126]	$In_xGa_{1-x}As$ [127]	$GaAs_{1-x}P_x$ [123, 128
ε_∞	10.89	8.16	12.3	9.11	10.89-2.73x	10.89+1.41x	10.89-1.78x
$\hbar\omega_{LO1}$ (meV)	36.25	50.09	29.79	50.19	36.22-4.67x-0.27x^2	36.32-3.75x-2.27x^2	36.17-3.17x
$\hbar\omega_{TO1}$ (meV)	33.29	44.88	27.18	45.47	33.16+0.58x-2.46x^2	33.5-3.64x	33.28+0.8x
$\hbar\omega_{LO2}$ (meV)					45.09+6.66x-1.72x^2	29.66-2.1x+2.08x^2	43.5+8.97x-2.49x^2
$\hbar\omega_{TO2}$ (meV)					44.93-1.19x+1.18x^2	29.53-2.45x	41.9+3.4x

1. Phonon dispersions

Within the DC model, the optical phonon modes are described by the electrostatic potential $\Phi(\mathbf{r}, z)$ ($\mathbf{r}$ is the in-plane position vector, z the growth direction) resulting from the polarization field created by atomic displacements in a polar semiconductor. In regions devoid of free charges, the phonon potential $\Phi(\mathbf{r}, z)$ satisfies the Poisson equation $\varepsilon(\omega)\nabla^2\Phi(\mathbf{r}, z) = 0$, where $\varepsilon(\omega)$ is the dielectric function. Using the generalized Lyddane-Sachs-Teller relation, $\varepsilon(\omega)$ takes the form of a single-pole function,

$$\varepsilon(\omega) = \varepsilon_\infty \frac{\omega^2 - \omega_{LO}^2}{\omega^2 - \omega_{TO}^2}, \tag{42}$$

for a binary alloy, and obeys a double-pole relation [122],

$$\varepsilon(\omega) = \varepsilon_\infty \frac{(\omega^2 - \omega_{LO1}^2)(\omega^2 - \omega_{LO2}^2)}{(\omega^2 - \omega_{TO1}^2)(\omega^2 - \omega_{TO2}^2)}, \tag{43}$$

for a ternary alloy, where LO (TO) stands for the longitudinal (transverse) optical mode, and 1 and 2 denote the material type. ε_∞ is the high-frequency dielectric constant of the alloy, found as a linear combination of the constituents' constants. The dielectric constants and phonon frequencies of the alloys used in the 6.7 μm QCL [94] are listed in Table III, where for ternary alloys $A_xB_{1-x}C$, $\hbar\omega_{LO1}$ ($\hbar\omega_{TO1}$) is the BC-like LO (TO) frequency, and $\hbar\omega_{LO2}$ ($\hbar\omega_{TO2}$) is the AC-like LO (TO) frequency. The strain-induced frequency shifts in $GaAs_{1-x}P_x$ and $In_xGa_{1-x}As$ grown on GaAs substrates are less than 1 meV [123–125], so they are not included here.

X. Gao, D. Botez, and I. Knezevic, "Multivalley simulation and design of quantum cascade lasers,"
in Encyclopedia of Nanoscience and Nanotechnology, Edited by H. S. Nalwa, American Scientific Publishers, in press. (2008)

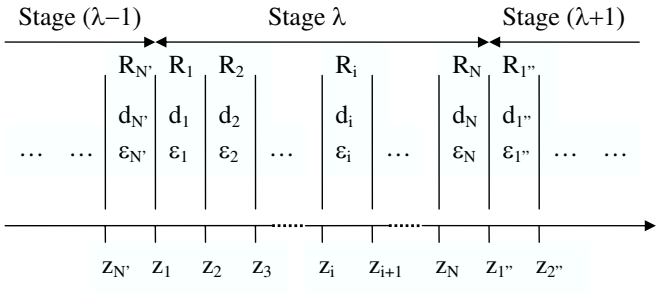

FIG. 36. Schematic of a MQW QCL heterostructure. The z axis is chosen as the growth direction. Reprinted with permission from [109], X. Gao, D. Botez, and I. Knezevic, *J. Appl. Phys.*, accepted (December, 2007). © 2007, American Institute of Physics.

Since phonons are unconfined in the x-y plane in a multiple quantum well system, the potential $\Phi(\mathbf{r}, z)$ can be written as

$$\Phi(\mathbf{r}, z) = \sum_{\mathbf{q}} f(q)\phi(q, z)e^{i\mathbf{q}\cdot\mathbf{r}}, \tag{44}$$

where $\mathbf{q}$ and $\mathbf{r}$ are the in-plane phonon wave and position vectors, $q = |\mathbf{q}|$, $\phi(q, z)$ is the so-called functional form, and $f(q)$ is the normalization coefficient (calculation of $f(q)$ can be found in Sec. V A 2). Substituting Eq. (44) into the Poisson equation, we obtain the equation that $\phi(q, z)$ must satisfy,

$$\varepsilon(\omega)\left(\frac{\partial^2}{\partial z^2} - q^2\right)\phi(q, z) = 0. \tag{45}$$

Eq. (45) has two types of solutions: interface (IF) modes, for which $[(\partial^2/\partial z^2) - q^2]\,\phi(q, z) = 0$ and $\varepsilon(\omega) \neq 0$, and confined (CF) modes, for which $\varepsilon(\omega) = 0$.

For interface (IF) modes, $\varepsilon(\omega) \neq 0$ and the modes should have frequencies $\omega(q) \neq \omega_{LO}$. In region R_i of Fig. 36 (i = 1, 2, ..., N, where N is the number of layers in one stage), $\phi_i(q, z)$ is given by

$$\phi_i(q, z) = c_{i,+}e^{q(z-z_i)} + c_{i,-}e^{-q(z-z_i)}. \tag{46}$$

In the DC model, the potential $\phi_i(q, z)$ and the tangential component of the electric field $\varepsilon_i(\partial/\partial z)\phi_i(q, z)$ (where $\varepsilon_i = \varepsilon_i(\omega)$, with ω omitted for brevity) must be continuous at each interface. It then follows that, at the interface between regions R_{i+1} and R_i (at $z = z_{i+1}$),

$$\phi_{i+1}(q, z_{i+1}) = \phi_i(q, z_{i+1}), \tag{47}$$

$$\varepsilon_{i+1}\frac{\partial}{\partial z}\phi_{i+1}(q, z_{i+1}) = \varepsilon_i\frac{\partial}{\partial z}\phi_i(q, z_{i+1}). \tag{48}$$

X. Gao, D. Botez, and I. Knezevic, "Multivalley simulation and design of quantum cascade lasers,"
in Encyclopedia of Nanoscience and Nanotechnology, Edited by H. S. Nalwa, American Scientific Publishers, in press. (2008)

After some manipulations, we obtain the following compact matrix-form equation,

$$\begin{bmatrix} c_{i+1,+} \\ c_{i+1,-} \end{bmatrix} = \mathbf{Q}_i(d_i) \begin{bmatrix} c_{i,+} \\ c_{i,-} \end{bmatrix}, \tag{49}$$

where d_i denotes the thickness of the ith layer, and the transfer matrix $\mathbf{Q}_i(d_i)$ is defined as

$$\mathbf{Q}_i(d_i) = \frac{1}{2} \begin{bmatrix} (1+\frac{\varepsilon_i}{\varepsilon_{i+1}})e^{qd_i} & (1-\frac{\varepsilon_i}{\varepsilon_{i+1}})e^{-qd_i} \\ (1-\frac{\varepsilon_i}{\varepsilon_{i+1}})e^{qd_i} & (1+\frac{\varepsilon_i}{\varepsilon_{i+1}})e^{-qd_i} \end{bmatrix}. \tag{50}$$

By applying the chain rule, the coefficients in the last (Nth) and the first layer of the same stage are related by

$$\begin{bmatrix} c_{N,+} \\ c_{N,-} \end{bmatrix} = \mathbf{Q}_{N-1}(d_{N-1})...\mathbf{Q}_i(d_i)...\mathbf{Q}_1(d_1) \begin{bmatrix} c_{1,+} \\ c_{1,-} \end{bmatrix}. \tag{51}$$

Next, by imposing the electrostatic boundary conditions at the interface between two adjacent stages, i.e., at $z = z_1$, we obtain

$$\begin{bmatrix} c_{1,+} \\ c_{1,-} \end{bmatrix} = \mathbf{Q}_{N'}(d_{N'}) \begin{bmatrix} c_{N',+} \\ c_{N',-} \end{bmatrix}, \tag{52}$$

with $\mathbf{Q}_{N'}$ defined as

$$\mathbf{Q}_{N'}(d_{N'}) = \frac{1}{2} \begin{bmatrix} (1+\frac{\varepsilon_{N'}}{\varepsilon_1})e^{qd_{N'}} & (1-\frac{\varepsilon_{N'}}{\varepsilon_1})e^{-qd_{N'}} \\ (1-\frac{\varepsilon_{N'}}{\varepsilon_1})e^{qd_{N'}} & (1+\frac{\varepsilon_{N'}}{\varepsilon_1})e^{-qd_{N'}} \end{bmatrix}. \tag{53}$$

To obtain the IF dispersions in a MQW QCL, the isolated-stage boundary conditions (BCs) are generally assumed [103, 104, 112], namely, the IF potentials purely decay in the N'th and Nth layers of Fig. 36, i.e., $c_{N,+} = 0$ and $c_{N',-} = 0$. However, this assumption leads to a discontinuity in the phonon potentials at the interfaces between adjacent stages [129], which violates the BCs of the DC model. In order to properly account for the periodicity of QCL structures, *periodic BCs* [106] are used here in obtaining the IF modes, namely, $c_{N',+} = c_{N,+}$, and $c_{N',-} = c_{N,-}$. It is also evident that $Q_{N'}(d_{N'}) = Q_N(d_N)$. Then we end up with the following eigenvalue equation,

$$(\mathbf{M} - \mathbf{I}) \begin{bmatrix} c_{1,+} \\ c_{1,-} \end{bmatrix} = 0, \tag{54}$$

X. Gao, D. Botez, and I. Knezevic, "Multivalley simulation and design of quantum cascade lasers,"
in Encyclopedia of Nanoscience and Nanotechnology, Edited by H. S. Nalwa, American Scientific Publishers, in press. (2008)

where $\mathbf{I}$ is the identity matrix, and

$$\mathbf{M} = \mathbf{Q}_N(d_N)\mathbf{Q}_{N-1}(d_{N-1})...\mathbf{Q}_i(d_i)...\mathbf{Q}_1(d_1). \tag{55}$$

For Eq. (54) to have a nontrivial solution, $\det(\mathbf{M}-\mathbf{I}) = 0$. Since $\mathbf{M} = \mathbf{M}(q,\omega)$, the solutions to $\det(\mathbf{M}-\mathbf{I}) = 0$ yield the dispersion relations of IF modes. The number of IF modes is determined by the number of interfaces in one stage and the constituents of each interface. Each binary/binary interface contributes with 2 IF modes, while the number of contributed modes per interface is 3 for a binary/ternary (each ternary has two LO-like frequencies), and 4 for a ternary/ternary interface.

The IF dispersions for the 6.7 μm QCL are shown in Fig. 37. One stage of this structure has 17 interfaces, among which 5 are ternary/ternary and 12 are ternary/binary, giving rise to a total of 56 IF modes. The mode frequencies at each q are obtained by numerically solving $\det(\mathbf{M}(q,\omega)-\mathbf{I}) = 0$. Due to the many interfaces and the multiplication in Eq. (55), $\det(\mathbf{M}(q,\omega)-\mathbf{I})$ rapidly oscillates as a function of ω, making it increasingly difficult to resolve between consecutive zeroes for larger chosen q's. Therefore, for the 6.7 μm QCL considered, we explicitly calculate the frequencies up to $q_{lim} = 0.25$ Å^{-1}, while at higher q's we simply extrapolate $\omega(q > q_{lim}) = \omega(q_{lim})$ for each mode obtained.

Once the IF dispersions have been obtained, the potential $\phi_i(q,z)$ in region R_i for each IF mode, can be deduced by setting $c_{1,+} = 1$. [The real value of $c_{1,+}$ will be taken care of by the normalization coefficient $f(q)$ (Sec. V A 2).] The IF potential in one stage consists of the different layer $\phi_i(q,z)$ in that stage, i.e., $\phi_\lambda(q,z) = \phi_i(q,z)$, $z \in R_i$. Then the IF potential in the entire computational domain (ECD) (two or more stages), $\phi(q,z)$, is obtained by repeating the one-stage potential, $\phi_\lambda(q,z)$, with the proper shift in the z-axis.

For confined (CF) bulk-like modes, $\varepsilon(\omega) = 0$, so $\omega = \omega_{LO}$ for a binary alloy, and $\omega = \omega_{LO1}$ or ω_{LO2} for a ternary alloy. The LO phonons propagate in a chosen layer to the interfaces, and are fully backscattered from them because the neighboring layers have different LO frequencies; the incident and backscattered waves interfere and result in zero potential at the interfaces [130, 131]. Therefore, in each layer i ($i = 1, 2, \cdots, N_{tot}$, where N_{tot} is the total number of layers in the ECD), the following functional form of the CF potential holds:

$$\phi_i(q,z) = \sin\left[\frac{m\pi}{d_i}(z - z_i)\right], \quad m = 1, 2, \cdots, \tag{56}$$

where $z_i \le z < z_{i+1}$ and $d_i = z_{i+1} - z_i$ is the layer thickness. In the case of the 6.7 μm QCL, there are 7 CF LO modes: InAs-like from InGaAs (29.47 meV), GaP-like from

X. Gao, D. Botez, and I. Knezevic, "Multivalley simulation and design of quantum cascade lasers,"
in Encyclopedia of Nanoscience and Nanotechnology, Edited by H. S. Nalwa, American Scientific Publishers, in press. (2008)

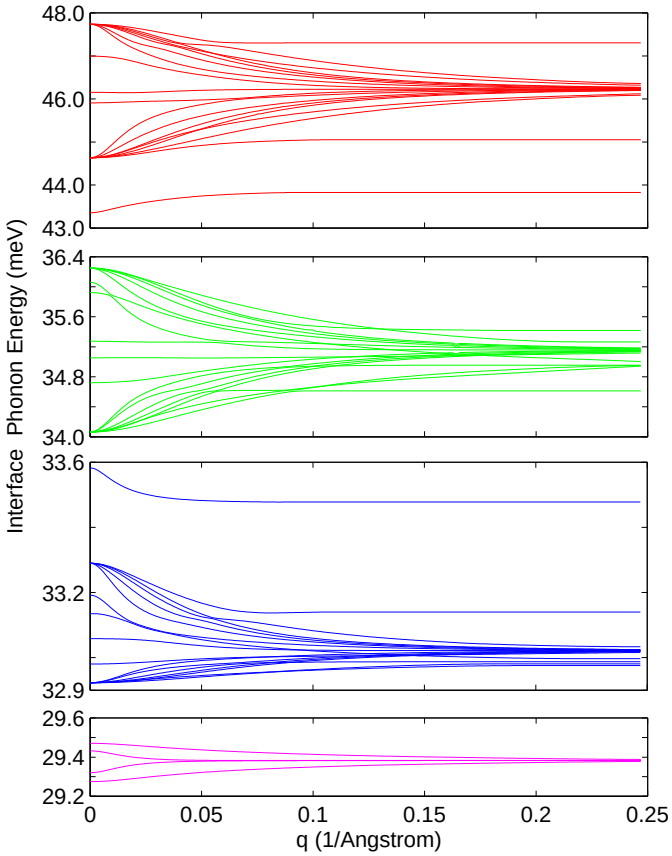

FIG. 37. Dispersion relations of the 56 IF modes for the 6.7 μm QCL. Bottom to top, the dispersions include 4 InAs-like modes around 29.4 meV, 17 GaAs-like modes within 32.8-33.6 meV, a second set of 17 GaAs-like modes within 34-36.4 meV, and 18 modes (2 GaP-like and 16 AlAs-like) within 43-48 meV. Reprinted with permission from [109], X. Gao, D. Botez, and I. Knezevic, *J. Appl. Phys.*, accepted (December, 2007). © 2007, American Institute of Physics.

GaAsP (46.69 meV), AlAs-like from AlGaAs (47.74 meV), GaAs (36.25 meV), GaAs-like from InGaAs (35.92 meV), GaAs-like from AlGaAs (34.06 meV), and GaAs-like from GaAsP (34.9 meV) (see Table III).

2. Phonon mode normalization

The normalization coefficient $f(q)$ of the IF and CF potentials for each phonon mode can be determined from the orthonormality and completeness conditions imposed on the phonon eigenfunctions [111, 132]. In polar crystals, optical vibrations of the lattice, characterized by a relative displacement $\mathbf{u}(\mathbf{r}, z)$, result in macroscopic electric and polarization

X. Gao, D. Botez, and I. Knezevic, "Multivalley simulation and design of quantum cascade lasers,"
in Encyclopedia of Nanoscience and Nanotechnology, Edited by H. S. Nalwa, American Scientific Publishers, in press. (2008)

fields ($\mathbf{E}(\mathbf{r},z)$ and $\mathbf{P}(\mathbf{r},z)$, respectively). These quantities are related to each other by the macroscopic Born-Huang theory [133]. Using two-dimensional Fourier transforms, we can rewrite $\mathbf{u}(\mathbf{r},z) = \sum_q \mathbf{u}(q,z)e^{i\mathbf{q}\cdot\mathbf{r}}$, similarly for $\mathbf{E}(\mathbf{r},z)$ and $\mathbf{P}(\mathbf{r},z)$. For binary layers, the Fourier transforms are related by [111, 113, 133]

$$\rho(\omega_{TO}^2 - \omega^2)\mathbf{u}(q,z) = e^*\mathbf{E}(q,z), \tag{57a}$$

$$\mathbf{P}(q,z) = \varepsilon_0(\varepsilon_\infty - 1)\mathbf{E}(q,z) + e^*\mathbf{u}(q,z), \tag{57b}$$

where ρ is the reduced mass density, e^* the effective ionic charge density, and ε_0 is the vacuum permittivity. In Eq. (57b), the first term on the right-hand side represents the electronic polarization, while the second term describes the ionic polarization. Making use of the relation

$$\mathbf{D}(q,z) = \varepsilon_0\varepsilon(\omega)\mathbf{E}(q,z) = \varepsilon_0\mathbf{E}(q,z) + \mathbf{P}(q,z), \tag{58}$$

and Eq. (42), it is straightforward to obtain

$$(e^*)^2 = \rho\varepsilon_0\varepsilon_\infty(\omega_{LO}^2 - \omega_{TO}^2), \tag{59}$$

and then

$$\left|\sqrt{\rho}\mathbf{u}(q,z)\right|^2 = \frac{\varepsilon_0}{2\omega}\frac{d\varepsilon(\omega)}{d\omega}\left|\mathbf{E}(q,z)\right|^2, \tag{60}$$

where the relation that $d\varepsilon(\omega)/d\omega = \varepsilon_\infty 2\omega\left(\omega_{LO}^2 - \omega_{TO}^2\right)/\left(\omega^2 - \omega_{TO}^2\right)^2$ has been used.

In the case of ternary layers $\mathrm{A}_x\mathrm{B}_{1-x}\mathrm{C}$ $(0 < x < 1)$, we have [106, 120]

$$\rho_1(\omega_{TO1}^2 - \omega^2)\mathbf{u}_1(q,z) = e_1^*\mathbf{E}(q,z), \tag{61a}$$

$$\rho_2(\omega_{TO2}^2 - \omega^2)\mathbf{u}_2(q,z) = e_2^*\mathbf{E}(q,z), \tag{61b}$$

$$\begin{aligned}\mathbf{P}(q,z) &= \varepsilon_0(\varepsilon_\infty - 1)\mathbf{E}(q,z)\\ &+(1-x)e_1^*\mathbf{u}_1(q,z) + xe_2^*\mathbf{u}_2(q,z),\end{aligned} \tag{61c}$$

with 1 and 2 referring to the BC-like and AC-like alloy modes, respectively. Combination of Eqs. (58) and (61c) results in

$$\varepsilon_0\left[\varepsilon(\omega) - \varepsilon_\infty\right]\mathbf{E}(q,z) = (1-x)e_1^*\mathbf{u}_1(q,z) + xe_2^*\mathbf{u}_2(q,z). \tag{62}$$

Substituting Eqs. (61a), (61b) and (43) into Eq. (62) leads to

$$\begin{aligned}&\frac{(1-x)\left(e_1^*\right)^2}{\rho_1}\left(\omega_{TO2}^2 - \omega^2\right) + \frac{x\left(e_2^*\right)^2}{\rho_2}\left(\omega_{TO1}^2 - \omega^2\right)\\ =\ &\varepsilon_0\varepsilon_\infty\left[\left(\omega^2 - \omega_{LO1}^2\right)\left(\omega^2 - \omega_{LO2}^2\right)\right.\\ -\ &\left.\left(\omega^2 - \omega_{TO1}^2\right)\left(\omega^2 - \omega_{TO2}^2\right)\right].\end{aligned} \tag{63}$$

X. Gao, D. Botez, and I. Knezevic, "Multivalley simulation and design of quantum cascade lasers,"
in Encyclopedia of Nanoscience and Nanotechnology, Edited by H. S. Nalwa, American Scientific Publishers, in press. (2008)

¿From Eq. (63), we can derive the expressions for $(e_1^*)^2$ (let $\omega = \omega_{TO1}$) and $(e_2^*)^2$ (let $\omega = \omega_{TO2}$),

$$(e_1^*)^2 = \frac{\rho_1 \varepsilon_0 \varepsilon_\infty \left(\omega_{LO1}^2 - \omega_{TO1}^2\right)\left(\omega_{LO2}^2 - \omega_{TO1}^2\right)}{(1-x)\left(\omega_{TO2}^2 - \omega_{TO1}^2\right)}, \tag{64a}$$

$$(e_2^*)^2 = \frac{\rho_2 \varepsilon_0 \varepsilon_\infty \left(\omega_{LO1}^2 - \omega_{TO2}^2\right)\left(\omega_{LO2}^2 - \omega_{TO2}^2\right)}{x\left(\omega_{TO1}^2 - \omega_{TO2}^2\right)}. \tag{64b}$$

By combining Eqs. (61) and (64), we obtain

$$\begin{aligned}(1-x)\left|\sqrt{\rho_1}\mathbf{u}_1(q,z)\right|^2 + x\left|\sqrt{\rho_2}\mathbf{u}_2(q,z)\right|^2 \\ = \frac{\varepsilon_0}{2\omega}\frac{d\varepsilon(\omega)}{d\omega}\left|\mathbf{E}(q,z)\right|^2,\end{aligned} \tag{65}$$

where the first derivative of the dielectric function has the following form for ternary alloys,

$$\begin{aligned}\frac{d\varepsilon(\omega)}{d\omega} = \varepsilon_\infty 2\omega \Bigg[&\frac{\left(\omega_{LO1}^2 - \omega_{TO1}^2\right)\left(\omega_{LO2}^2 - \omega_{TO1}^2\right)}{\left(\omega^2 - \omega_{TO1}^2\right)^2\left(\omega_{TO2}^2 - \omega_{TO1}^2\right)} \\ &+ \frac{\left(\omega_{LO1}^2 - \omega_{TO2}^2\right)\left(\omega_{LO2}^2 - \omega_{TO2}^2\right)}{\left(\omega^2 - \omega_{TO2}^2\right)^2\left(\omega_{TO1}^2 - \omega_{TO2}^2\right)}\Bigg].\end{aligned} \tag{66}$$

The generalized normalization condition for each optical (IF and CF) phonon mode ν in MQW structures consisting of arbitrary combinations of binary and ternary layers is given by [111, 122]

$$\begin{aligned}\sum_i A \int_{R_i} dz \Big[(1-x)\left|\sqrt{\rho_{1i}}\mathbf{u}_{1i}(q,z)\right|^2 \\ + x\left|\sqrt{\rho_{2i}}\mathbf{u}_{2i}(q,z)\right|^2\Big] = \frac{\hbar}{2\omega_\nu},\end{aligned} \tag{67}$$

where the summation goes over all the layers of interest, A is the in-plane area, $x = 0, 1$ for binary alloys, and $0 < x < 1$ for ternary ones. Substituting Eqs. (60) and (65) into Eq. (67), the normalization condition can be rewritten as

$$\sum_i A \int_{R_i} dz \, \frac{\varepsilon_0}{2\omega_\nu}\frac{d\varepsilon_i(\omega)}{d\omega}\left|\mathbf{E}^\nu(q,z)\right|^2 = \frac{\hbar}{2\omega_\nu}. \tag{68}$$

On the other hand, the electric field is related to the potential through

$$\begin{aligned}\mathbf{E}^\nu(\mathbf{r},z) &= -\nabla\Phi^\nu(\mathbf{r},z) \\ &= -\sum_{\mathbf{q}} e^{i\mathbf{q}\cdot\mathbf{r}}\left(iq\hat{q} + \hat{z}\frac{\partial}{\partial z}\right) f^\nu(q)\phi^\nu(q,z),\end{aligned} \tag{69}$$

X. Gao, D. Botez, and I. Knezevic, "Multivalley simulation and design of quantum cascade lasers,"
in Encyclopedia of Nanoscience and Nanotechnology, Edited by H. S. Nalwa, American Scientific Publishers, in press. (2008)

where $\hat{q}$ and $\hat{z}$ are the unit vectors for the $\mathbf{q}$ and z directions, respectively, hence,

$$\mathbf{E}^{\nu}(q,z) = \left(-iq\hat{q} - \hat{z}\frac{\partial}{\partial z}\right) f^{\nu}(q)\phi^{\nu}(q,z). \tag{70}$$

Putting Eqs. (70) into (68), we obtain the final expression for the normalization coefficient $f^{\nu}(q)$,

$$f^{\nu}(q) = \left(\frac{\hbar}{2A\omega_{\nu}}\right)^{\frac{1}{2}} \left\{\sum_i \left[\frac{\varepsilon_0}{2\omega_{\nu}}\frac{d\varepsilon_i(\omega)}{d\omega} I_i(q)\right]\right\}^{-\frac{1}{2}}, \tag{71}$$

where the summation over the layers 'i' should be carried out in one stage for IF modes, and $I_i(q)$ is defined as

$$I_i(q) = \int_{R_i} dz \left[q^2 \left|\phi_i^{\nu}(q,z)\right|^2 + \left|\frac{\partial \phi_i^{\nu}(q,z)}{\partial z}\right|^2\right]. \tag{72}$$

For IF modes, $I_i(q)$ is simplified to be

$$I_i(q) = q\left[c_{i,+}^2\left(e^{2qd_i} - 1\right) - c_{i,-}^2\left(e^{-2qd_i} - 1\right)\right], \tag{73}$$

and for CF modes,

$$I_i(q) = \left[q^2 + \left(\frac{m\pi}{d_i}\right)^2\right]\frac{d_i}{2}. \tag{74}$$

The IF potentials are calculated for all q's of interest for the 6.7 μm QCL. Arbitrarily selected normalized IF potentials, $f^{\nu}(q)\phi^{\nu}(q,z)$, at $q = 0.03$ Å^{-1} are given in Fig. 38. It is clearly seen that the IF potentials peak at the layer interfaces and are periodic between stages. The normalized GaAs-like CF potentials for m = 1 and $q = 0.03$ Å^{-1} are shown in Fig. 39. The CF potentials in each layer are independent and calculated separately, and they are plotted together for comparison. The layers consisting of the same alloy have the same confined GaAs-like LO frequencies, so there are 4 different frequencies in Fig. 39. It is noted that for the layers that have the same GaAs-like LO frequency within one stage, the normalized CF potentials show different amplitudes, which is because the normalization coefficients directly depend on the layer thickness as given in Eq. (74). The InAs-like, GaP-like, and AlAs-like CF potentials are similar to those in Fig. 39, but with different amplitudes.

B. Electron-LO Scattering with Phonon Confinement

The obtained IF dispersions and the potentials of the IF and CF modes are utilized to evaluate the electron-longitudinal polar optical (electron-LO) phonon scattering rates, which

X. Gao, D. Botez, and I. Knezevic, "Multivalley simulation and design of quantum cascade lasers,"
in Encyclopedia of Nanoscience and Nanotechnology, Edited by H. S. Nalwa, American Scientific Publishers, in press. (2008)

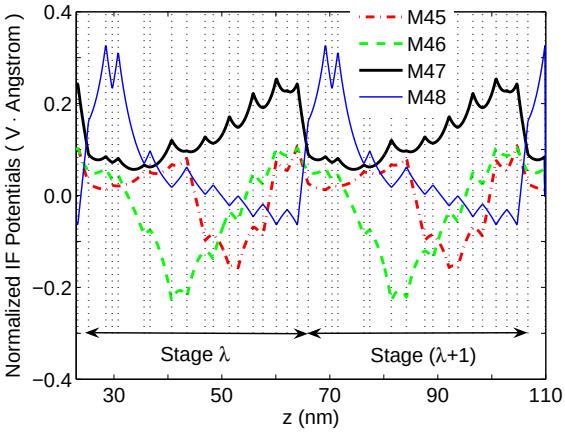

FIG. 38. Selected normalized IF potentials at $q = 0.03$ Å^{-1} for the 6.7 μm QCL, illustrating the continuity of the IF potentials and their periodicity between stages. The arbitrarily selected IF modes are 4 of the 18 modes within 43-48 meV from Fig. 37. The vertical dotted lines indicate interfaces between layers. Reprinted with permission from [109], X. Gao, D. Botez, and I. Knezevic, *J. Appl. Phys.*, accepted (December, 2007). © 2007, American Institute of Physics.

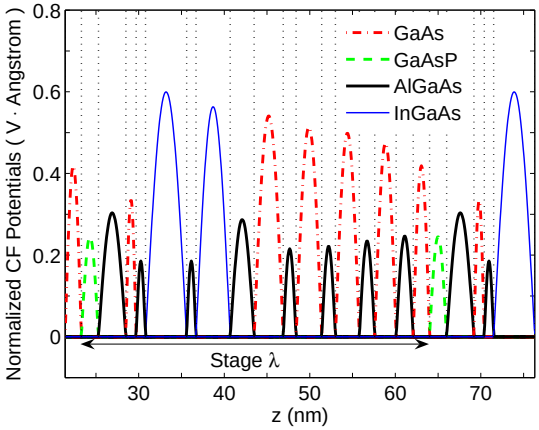

FIG. 39. Normalized GaAs-like CF potentials at m = 1 and $q = 0.03$ Å^{-1} for the 6.7 μm QCL. The dash-dotted red curves are the confined potentials in the GaAs layers, the dashed green ones in the GaAsP layers, the bold black curves in the AlGaAs layers, and the thin blue ones in the InGaAs layers. The vertical dotted lines indicate the interfaces between layers. Reprinted with permission from [109], X. Gao, D. Botez, and I. Knezevic, *J. Appl. Phys.*, accepted (December, 2007). © 2007, American Institute of Physics.

are then incorporated in the MMC simulator [59]. The electron-LO phonon interaction Hamiltonian can be written as

$$\begin{aligned} H_{e-LO}(\mathbf{r},z) &= -e\Phi(\mathbf{r},z) \\ &= -e\sum_{\mathbf{q},\nu} f^{\nu}(q)\phi^{\nu}(q,z)e^{i\mathbf{q}\cdot\mathbf{r}}(b_q + b^{+}_{-q}), \end{aligned} \tag{75}$$

where b_q and b^{+}_{-q} are the phonon destruction and creation operators, respectively, inserted to indicate the destruction and creation of phonons, ν goes over all IF and CF modes, while $f^{\nu}(q)$ and $\phi^{\nu}(q,z)$ depend on a particular IF or CF mode. Following Fermi's Golden Rule, the transition rate of an electron from an initial state $|j\mathbf{k}\rangle$ (in-plane wave vector $\mathbf{k}$ and subband j) to a final state $|j'\mathbf{k}'\rangle$ is given by

$$S_{jj'}(\mathbf{k},\mathbf{k}') = \frac{2\pi}{\hbar}\left|M_{jj'}(\mathbf{k},\mathbf{k}')\right|^2 \delta\left[E' - E \pm \hbar\omega_{\nu}(q)\right], \tag{76}$$

with the upper and lower signs corresponding to phonon emission and absorption, respectively (this convention will be used throughout this section). The delta function guarantees energy conservation in the process, where $E' = E_{j'} + \hbar^2 k'^2/2m^*_{j'}$, and $E = E_j + \hbar^2 k^2/2m^*_j$, with E_j ($E_{j'}$) and m^*_j ($m^*_{j'}$) being the electron subband energy and effective mass obtained as detailed in Sec. II. The matrix element of the electron-LO interaction is

$$\begin{aligned} M_{jj'}(\mathbf{k},\mathbf{k}') &= \langle n_{q\nu} \pm 1, j'\mathbf{k}' \left| H_{e-LO}(\mathbf{r},z) \right| n_{q\nu}, j\mathbf{k}\rangle \\ &= -e\sum_{q\nu}\sqrt{n_{q\nu} + \frac{1}{2} \pm \frac{1}{2}}\int_V \Psi^*_{j'\mathbf{k}'}(\mathbf{r},z) \\ &\times\ f^{\nu}(q)\phi^{\nu}(q,z)e^{\mp i\mathbf{q}\cdot\mathbf{r}}\Psi_{j\mathbf{k}}(\mathbf{r},z), \end{aligned} \tag{77}$$

where $n_{q\nu}$ denotes the number of equilibrium phonons in mode ν, the integration is carried out in the whole volume of computation, and the electronic states take the form

$$\Psi_{j\mathbf{k}}(\mathbf{r},z) = \frac{1}{\sqrt{A}}e^{i\mathbf{k}\cdot\mathbf{r}}\psi_j(z). \tag{78}$$

Details of solving for $\psi_j(z)$ are given in Sec. II. By performing the integration, we obtain

$$\begin{aligned} M_{jj'}(\mathbf{k},\mathbf{k}') &= -e\sum_{\nu}\sqrt{n_{q\nu} + \frac{1}{2} \pm \frac{1}{2}}\, g^{\nu}_{jj'}(q) \\ &\times\ \delta(\mathbf{k}' - \mathbf{k} \pm \mathbf{q}), \end{aligned} \tag{79}$$

where the summation over q is killed due to the delta function that ensures the in-plane momentum conservation. Given the electron initial ($\mathbf{k}$) and final ($\mathbf{k}'$) wave vectors, the

X. Gao, D. Botez, and I. Knezevic, "Multivalley simulation and design of quantum cascade lasers,"
in Encyclopedia of Nanoscience and Nanotechnology, Edited by H. S. Nalwa, American Scientific Publishers, in press. (2008)

exchanged phonon wave vector must have the following magnitude,

$$q = |\mathbf{k}' - \mathbf{k}| = k'^2 + k^2 - 2k'k\cos\theta, \tag{80}$$

with θ being the angle between vectors $\mathbf{k}'$ and $\mathbf{k}$. The electron-phonon coupling function, $g^{\nu}_{jj'}(q)$, is defined as

$$g^{\nu}_{jj'}(q) = \int_0^L dz \psi^*_{j'}(z) f^{\nu}(q) \phi^{\nu}(q,z) \psi_j(z), \tag{81}$$

with L being the total length of the ECD along z. The total scattering rate, $\Gamma_{jj'}(\mathbf{k})$, is obtained by summing over all final wave vectors $\mathbf{k}'$, i.e.,

$$\begin{aligned}\Gamma_{jj'}(\mathbf{k}) &= \sum_{\mathbf{k}'} S_{jj'}(\mathbf{k},\mathbf{k}') = \frac{2\pi e^2}{\hbar}\frac{A}{(2\pi)^2} \\ &\times \sum_{\nu} \int d^2\mathbf{k}' \left(n_{q\nu} + \frac{1}{2} \pm \frac{1}{2}\right) \left|g^{\nu}_{jj'}(q)\right|^2 \\ &\times \delta(\mathbf{k}' - \mathbf{k} \pm \mathbf{q}) \delta\left(E' - E \pm \hbar\omega_{\nu}(q)\right). \end{aligned} \tag{82}$$

where the "sum-to-integral" rule, $\sum_{\mathbf{k}'} = A/(2\pi)^2 \int d^2\mathbf{k}'$, is used. By performing the $\mathbf{k}'$ integration in polar coordinates and utilizing properties of the delta functions, we reach the final expression for $\Gamma_{jj'}(\mathbf{k})$,

$$\begin{aligned}\Gamma_{jj'}(\mathbf{k}) = \frac{A m^*_{j'} e^2}{2\pi\hbar^3} \sum_{\nu} \int_0^{2\pi} d\theta \left(n_{q\nu} + \frac{1}{2} \pm \frac{1}{2}\right) \\ \times \left|g^{\nu}_{jj'}(q)\right|^2 \vartheta\left(E_{\mathbf{k}} + \hbar\omega^{\mp}_{\nu}\right), \end{aligned} \tag{83}$$

with $E_{\mathbf{k}} = \hbar^2 k^2/2m^*_j$, $\hbar\omega^{\mp}_{\nu} = E_j - E_{j'} \mp \hbar\omega_{\nu}(q)$, and ϑ being the Heaviside step function. For the IF modes, $n_{q\nu}$ and $\hbar\omega_{\nu}(q)$ depend on the wave vector q, but there is no q-dependence for the CF modes. The q value in Eq. (83) is determined from the in-plane momentum and energy conservation laws, taking into account the different effective masses in the initial and final subbands,

$$\begin{aligned} q = \frac{\sqrt{2}}{\hbar} \Big\{ &(m^*_j + m^*_{j'}) E_{\mathbf{k}} + m^*_{j'}(\hbar\omega^{\mp}_{\nu}) \\ &- 2\cos\theta \left[m^*_j m^*_{j'} E_{\mathbf{k}} (E_{\mathbf{k}} + \hbar\omega^{\mp}_{\nu})\right]^{\frac{1}{2}} \Big\}^{\frac{1}{2}}. \end{aligned} \tag{84}$$

Since the right-hand side of Eq. (84) has a complicated q-dependence for the IF modes due to their dispersions, it is necessary to numerically solve Eq. (84) for a required q during the IF rate calculations. If $q \leq q_{lim}$, the exact IF frequency $\omega_{\nu}(q)$, is taken; otherwise,

X. Gao, D. Botez, and I. Knezevic, "Multivalley simulation and design of quantum cascade lasers,"
in Encyclopedia of Nanoscience and Nanotechnology, Edited by H. S. Nalwa, American Scientific Publishers, in press. (2008)

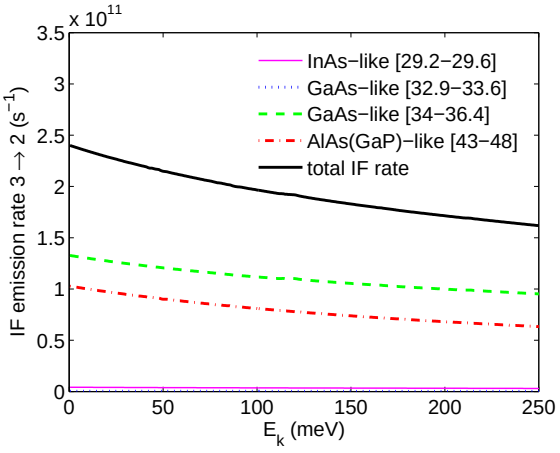

FIG. 40. IF emission rates from the upper to lower lasing levels (3→2) for the 6.7 μm QCL at F = 55 kV/cm and T = 77 K. The numbers in the brackets denote the energy ranges (in meV) of the corresponding IF modes shown in Fig. 37. Each curve represents the sum of the IF rates for all the modes in the specified energy range. Reprinted with permission from [109], X. Gao, D. Botez, and I. Knezevic, *J. Appl. Phys.*, accepted (December, 2007). © 2007, American Institute of Physics.

the IF frequency at q_{lim}, $\omega_\nu(q_{lim})$, is used to compute q. The calculated IF emission rates from the upper lasing level 3 to the lower lasing level 2 are shown in Fig. 40 for the 6.7 μm QCL, at the field of 55 kV/cm and the lattice temperature of 77 K. The cumulative rate for the 17 GaAs-like IF modes within the 32.9-33.6 meV window is indistinguishable from the horizontal axis, implying their negligible contribution. The 4 InAs-like IF modes also have a small contribution due to the low In content (10%) and the smaller phonon energies. The dominant contributions come from the higher-energy IF modes, where the GaAs-like modes within 34-36.4 meV contribute the most, as expected for transitions in GaAs-rich wells.

The CF scattering rates can be calculated in the zero-dispersion limit of the bulk-like CF modes, since it was shown [119] that these rates are insensitive to the bulk dispersions. For each mode $\hbar\omega_{LO}$, the CF rates are computed separately with $m = 1, 2, \cdots, 20$ (the contribution of higher-order modes is negligible) for all the layers that have the same frequency, and are summed up to yield the total rate for the particular mode. Figure 41 shows the CF emission rates of 3→2 for the 6.7 μm QCL at F = 55 kV/cm and T = 77 K. The GaP-like CF mode shows a negligible contribution to the total CF rate, since each stage has only one GaAsP layer and the electronic wavefunction magnitudes in that layer are very small. The 4 GaAs-like CF modes completely dominate the total rate, among which the GaAs-like mode

X. Gao, D. Botez, and I. Knezevic, "Multivalley simulation and design of quantum cascade lasers,"
in Encyclopedia of Nanoscience and Nanotechnology, Edited by H. S. Nalwa, American Scientific Publishers, in press. (2008)

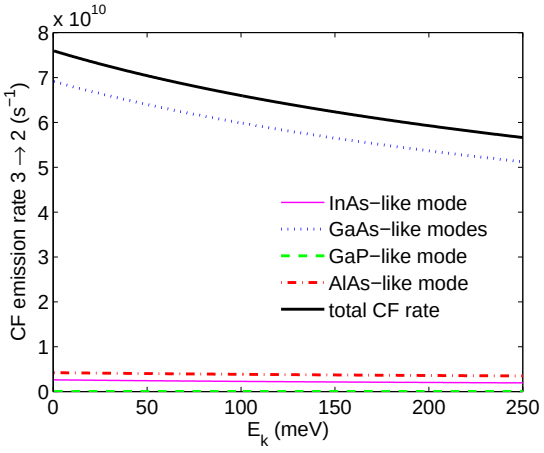

FIG. 41. CF emission rates of 3→2 for the 6.7 μm QCL at F = 55 kV/cm and T = 77 K. The GaAs-like modes include GaAs LO and 3 GaAs-like LO modes that originate from InGaAs, AlGaAs, and GaAsP. Reprinted with permission from [109], X. Gao, D. Botez, and I. Knezevic, *J. Appl. Phys.*, accepted (December, 2007). © 2007, American Institute of Physics.

originating from InGaAs contributes to the CF rate about an order of magnitude more than the other 3 modes.

C. Effects of Phonon Confinement

Next, the effects of phonon confinement on the electron-LO scattering rates and the transport properties of the optimized 6.7 μm structure C are investigated in detail. In Figs. 42 and 43, the sum of the IF and CF emission rates for the 3→2 and 2→1 transitions are compared to the rates obtained using bulk GaAs and AlAs phonons. In both transitions, it can be seen that the total IF+CF rates fall between the bulk GaAs and AlAs rates, consistent with the sum rule for scattering rate calculation in quantum-well systems [82]. And the total IF+CF rates are very close to the bulk GaAs rates, which justifies the use of bulk GaAs phonon approximation in Secs. II-IV. This result also agrees with other work [82, 103] on phonon confinement in quantum-well systems.

In order to explore the effects of phonon confinement on the transport properties of GaAs QCLs, we compute the scattering rates of all the Γ- and X-valley electronic states of interest by all of the 56 IF and 7 CF modes for the 6.7 μm QCL, and fully incorporate them in the MMC simulator. Due to the enormous memory requirement of storing the electron-IF

X. Gao, D. Botez, and I. Knezevic, "Multivalley simulation and design of quantum cascade lasers,"
in Encyclopedia of Nanoscience and Nanotechnology, Edited by H. S. Nalwa, American Scientific Publishers, in press. (2008)

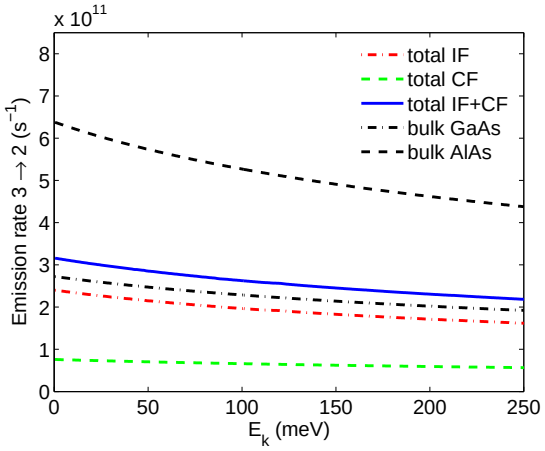

FIG. 42. Emission rates of 3→2 for the 6.7 μm QCL at F = 55 kV/cm and T = 77 K using the bulk phonon approximation and the IF+CF modes. Reprinted with permission from [109], X. Gao, D. Botez, and I. Knezevic, *J. Appl. Phys.*, accepted (December, 2007). © 2007, American Institute of Physics.

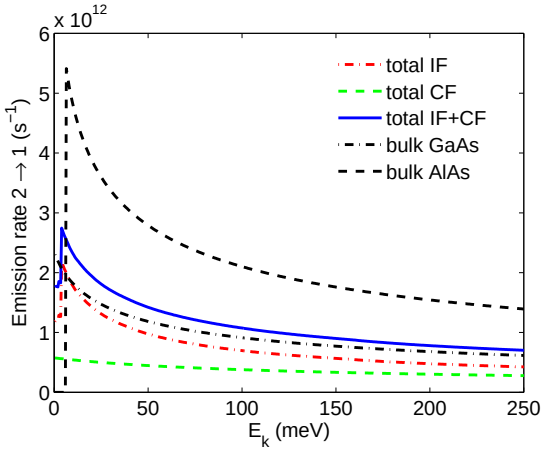

FIG. 43. Emission rates from the lower lasing level 2 to the active ground level 1 (2→1) for the 6.7 μm QCL at F = 55 kV/cm and T = 77 K using the bulk phonon approximation and the IF+CF modes. Reprinted with permission from [109], X. Gao, D. Botez, and I. Knezevic, *J. Appl. Phys.*, accepted (December, 2007). © 2007, American Institute of Physics.

and electron-CF rates for all phonon modes, only the total IF+CF rates between any two subbands are pre-calculated and stored. During the Monte Carlo simulation, the IF and CF rates between two specified subbands by all phonon modes are calculated in real time, and random numbers are used to choose a particular phonon mode for scattering of an electron.

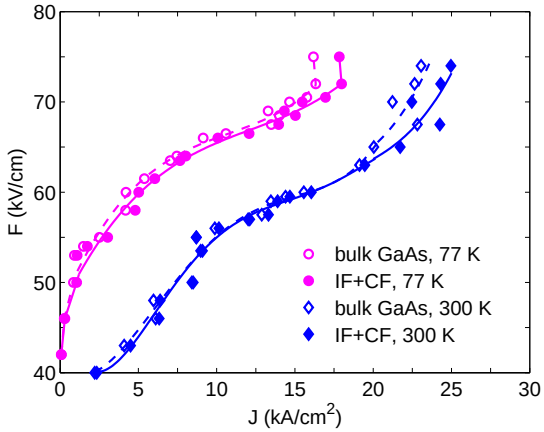

FIG. 44. Electric field vs current density at 77 K and 300 K lattice temperatures using the bulk GaAs phonon approximation and the IF+CF modes. Dashed and solid curves are polynomial fits to the data points to guide the eyes. Reprinted with permission from [109], X. Gao, D. Botez, and I. Knezevic, *J. Appl. Phys.*, accepted (December, 2007). © 2007, American Institute of Physics.

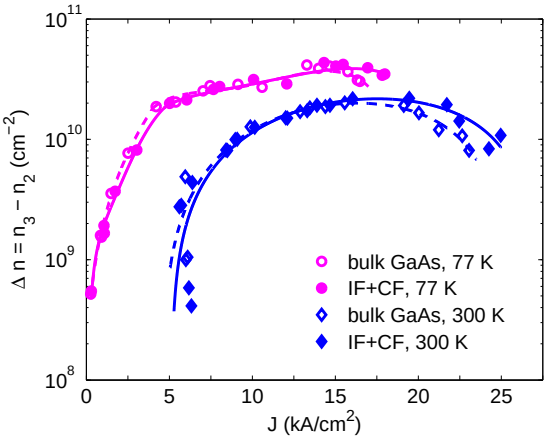

FIG. 45. Population inversion vs current density at 77 K and 300 K using the bulk GaAs phonon approximation and the IF+CF modes. Dashed and solid curves are polynomial fits to the data points to guide the eyes. Reprinted with permission from [109], X. Gao, D. Botez, and I. Knezevic, *J. Appl. Phys.*, accepted (December, 2007). © 2007, American Institute of Physics.

Besides the electron-IF and electron-CF scattering in both Γ- and X-valleys, the electron-electron and various intervalley scattering mechanisms are also included for the same stage and between adjacent stages (for details, see Sec. II).

The output characteristics of the 6.7 μm QCL from the above-described Monte Carlo

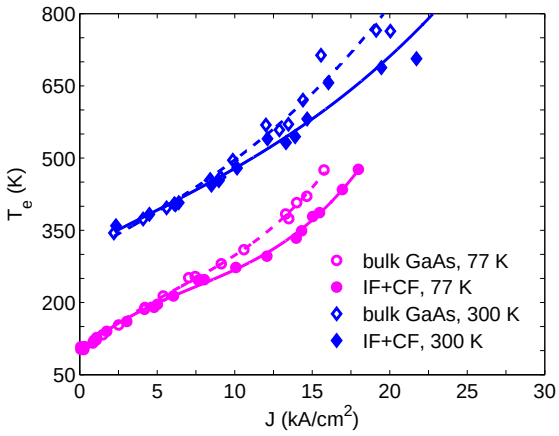

FIG. 46. Electron temperature vs current density at 77 K and 300 K using the bulk GaAs phonon approximation and the IF+CF modes. Dashed and solid curves are polynomial fits to the data points to guide the eyes. Reprinted with permission from [109], X. Gao, D. Botez, and I. Knezevic, *J. Appl. Phys.*, accepted (December, 2007). © 2007, American Institute of Physics.

simulator are presented in Figs. 44-46 at 77 K and 300 K lattice temperatures, where the results with the phonon confinement are compared to those obtained by using the bulk GaAs phonon approximation. From Fig. 44, it is clear that phonon confinement induces a minor correction to the current density for a given electric field at both 77 K and 300 K. The population inversion, with phonon confinement included, remains nearly identical to the case with bulk phonons at both temperatures (Fig. 45). On the other hand, the electron temperature T_e (Fig. 46), which characterizes the degree of electron heating, is somewhat reduced at high currents due to phonon confinement. This reduction occurs because, in the case of including phonon confinement, high-energy (> bulk GaAs LO) IF and CF phonons come into play, and through emitting those high-energy phonons, electrons are able to dissipate more energy to the lattice, leading to a lower electron temperature. Overall, simulation results demonstrate that phonon confinement turns out to have a minor impact on the device performance of the 6.7 μm QCL even at room temperature, and thus the GaAs bulk phonon approximation remains valid in transport simulation of GaAs QCLs.

VI. CONCLUSION

In this chapter, the following points were presented:

X. Gao, D. Botez, and I. Knezevic, "Multivalley simulation and design of quantum cascade lasers,"
in Encyclopedia of Nanoscience and Nanotechnology, Edited by H. S. Nalwa, American Scientific Publishers, in press. (2008)

(1) Development of the multivalley Monte Carlo QCL simulator

An ensemble Monte Carlo simulator that includes both Γ- and X-valley transport was described. The details of solving the Γ- and X-valley electronic states were presented. The Γ-states were calculated using the $\mathbf{k}\cdot\mathbf{p}$ method within the envelope function approximation, while the X-states were obtained within the effective mass framework. The Γ- and X-states were used to compute all the relevant scattering rates in detail. The included interaction mechanisms were electron-longitudinal polar optical (electron-LO) phonon, electron-electron, and various intervalley scattering processes, within the same stage and between adjacent stages (the LO and intervalley phonons are treated as bulk phonons). The effect of the electrostatic potential on the subband energy levels and wavefunctions has been studied by self-consistently solving the Schrödinger-Poisson equations. The electrostatic potential was shown to have a very minor effect on the electronic states for typical sheet doping densities in QCLs below 4×10^{11} cm^{-2}.

(2) X-valley leakage in GaAs/AlGaAs QCLs

The multivalley Monte Carlo simulator has been applied to simulate the transport properties of the two well-known equivalent-design GaAs/$Al_{0.33}Ga_{0.67}$As (33% QCL) and GaAs/$Al_{0.45}Ga_{0.55}$As (45% QCL) mid-infrared QCLs. The dominant X-valley leakage path in both QCLs was found to be through the interstage X→X intervalley scattering, causing a parallel leakage current J_{X}. The magnitude of J_{X} depends on the temperature and occupation of the X-valley subbands, which are populated primarily by the same-stage scattering from the Γ-continuum states (Γ_c). At the low lattice temperature of 77 K, J_{X} is small up to very high fields in both QCLs. However, at room temperature, the 33% QCL shows a much higher J_{X} than the 45% QCL even at low fields. The reason is that in the 33% QCL the coupling between the Γ-valley injector states (Γ_l) and the next-stage Γ_c is strong, which not only leads to the well-recognized $\Gamma_l \rightarrow \Gamma_c$ leakage, but also facilitates filling of the X states through efficient intrastage $\Gamma_c \rightarrow$ X scattering; with high X-valley population and high temperature, the efficient interstage X → X scattering yields a large J_{X}. In contrast, in the 45% QCL, coupling of Γ_l with the next-stage Γ_c is weak, due to good localization of the Γ_l states coming from the high (45% Al) barriers. Consequently, occupation of the X states through the same-stage $\Gamma_c \rightarrow$ X scattering is low, leading to small J_{X} up to high fields. The simulated threshold current density J_{th} with the X-valley leakage included is in very good agreement with experiment for both QCLs at both cryogenic and room temperatures.

X. Gao, D. Botez, and I. Knezevic, "Multivalley simulation and design of quantum cascade lasers,"
in Encyclopedia of Nanoscience and Nanotechnology, Edited by H. S. Nalwa, American Scientific Publishers, in press. (2008)

In addition, the effects of the electron-electron (e-e) interaction and electron heating in the two QCLs have been presented. The e-e scattering was shown to have two important effects: (i) it strongly increases intersubband electron redistribution; (ii) it drives the electron distributions in both the active region and the injector subbands to the heated-Maxwellian distributions, and all the electron distributions have an effective common electron temperature, higher than the lattice temperature. The elevated electron temperature directly reflects that, in QCLs, the electron system is not able to dissipate the large amount of energy provided by an external bias, which leads to strong internal heating.

(3) Simulation and optimization of deep-active-well GaAs QCLs

Three deep-active-well QCL structures (A, B, and C) that utilize the strain-compensated $In_{0.1}Ga_{0.9}As/GaAs/Al_{0.45}Ga_{0.55}As$ materials system grown on GaAs substrates have been analyzed. The three QCLs are all expected to emit at ~ 6.7 μm, the shortest wavelength so far achieved in GaAs-based mid-infrared QCLs, but have different injector design. The Monte Carlo simulator is employed to simulate the output characteristics of the three lasers and optimize the injector design for room-temperature operation.

Identification of issues associated with structures A and B by using the MMC simulator plays a direct and important role in obtaining the optimized structure C. The injector layer sequence of this structure is designed such that not only the coupling between the injector states and the next-stage Γ_c-states is reduced, but also the upper lasing levels has a good wavefunction overlap and small energy difference with the injector ground level. The optimized structure C shows the best device performance among the three structures, namely, it shows adequate optical gain for lasing action at both 77 K and 300 K lattice temperatures, in conjunction with an improved waveguide design that all three structures share. Compared to the state-of-the-art 9.4 μm GaAs QCL of Page *et al.* [31], although the optimized structure C shows higher X-valley leakage current due to the shorter wavelength, its threshold current density $J_{\rm th}$ is calculated to be 5 kA/cm^2 at 77 K and 14 kA/cm^2 at 300 K, close to the values for the 9.4 μm QCL ($J_{\rm th} = 4$ kA/cm^2 at 77 K and 16.7 kA/cm^2 at 300 K) [31]. Furthermore, electron heating at room temperature is similar to that of the 9.4 μm device. Therefore, structure C demonstrates that utilization of deep active quantum wells appears to be an attractive design approach for high performance GaAs-based QCLs at wavelengths below 7 μm.

(4) Investigation of phonon confinement in mid-IR GaAs QCLs

X. Gao, D. Botez, and I. Knezevic, "Multivalley simulation and design of quantum cascade lasers,"
in Encyclopedia of Nanoscience and Nanotechnology, Edited by H. S. Nalwa, American Scientific Publishers, in press. (2008)

Phonon confinement has been implemented in detail in the MMC simulator and its effects on the electronic transport properties in mid-infrared, GaAs-based multiple-quantum-well (MQW) QCLs were investigated. The macroscopic dielectric continuum model was used to describe the interface (IF) and confined (CF) optical phonons. The IF-mode dispersions were obtained by using the transfer matrix method with periodic boundary conditions. Normalization coefficients of the IF and CF potentials were thoroughly derived for MQW structures consisting of arbitrary combinations of binary and ternary alloys. The resulting IF dispersions and phonon potentials were utilized to compute the scattering rates for all the relevant Γ- and X-valley electron states. Electron-IF, electron-CF, electron-electron, and intervalley scattering mechanisms were fully incorporated in the multivalley Monte Carlo simulation of the optimized deep-active-well 6.7 μm GaAs QCL structure C. At both 77 K and 300 K lattice temperatures, simulation results demonstrated that inclusion of phonon confinement enhances the electron-LO phonon scattering rates only to a small extent and induces very minor correction to the device performance, with respect to the results obtained in the bulk-GaAs-phonon approximation. Therefore, the bulk phonon approximation in GaAs-based QCLs remains meritorious due to its simplicity and high accuracy.

The MMC simulator presented is not only able to characterize the electrical transport properties and quantify the possible leakage currents and electron heating for a given QCL structure, but is also able to provide a physical insight into optimizing a QCL design for desired performance. The simulator is applicable to any mid-infrared QCL structure, since their carrier transport is dominated by the scattering processes. It takes much less time than the NEGF method, but is able to capture the proper microscopic electron dynamics. The MMC simulator can be improved by coupling it with a thermal transport solver, so that the coupled simulator is capable of simultaneously predicting the electrical and thermal behavior in a real QCL device. Transport simulation continues to be an active research area and play a crucial role in the advancement of QCL devices.

Glossary

Quantum cascade laser (QCL) An electrically-pumped unipolar mid- to far-infrared coherent light source, where an electron cascades down the energy level staircase formed in a multiple-quantum-well heterostructure and emits multiple photons.

X. Gao, D. Botez, and I. Knezevic, "Multivalley simulation and design of quantum cascade lasers,"
in Encyclopedia of Nanoscience and Nanotechnology, Edited by H. S. Nalwa, American Scientific Publishers, in press. (2008)

Continuous wave operation Mode of operation in which a laser is continuously pumped (electrically or optically) and continuously emits light. In continuous-wave operation, lasers tend to generate a lot of heat and need efficient cooling systems.

Pulsed operation Mode of operation in which a laser is pumped with a periodic electrical or optical pulse signal and emits light in the form of optical pulses. In pulsed operation, lasers become much less heated than in continuous-wave operation.

Effective mass A quantity describing the curvature of crystalline bands near the band extrema. For the description of transport properties in semiconductors, where relevant electronic states are usually near the conduction band bottom (valence band top), electrons (holes) can be treated as free particles, with an effective mass determined from the bandstructure.

Envelope function approximation The wavefunction of an electron in a semiconductor heterostructure is approximated by a slowly varying (on atomic scales) envelope function, from which physical properties can be derived.

k·p method An efficient approach for calculating the band structure in the vicinity of a band extremum. Often used in optical devices near the Γ-valley point.

Schrödinger-Poisson solver The Schrödinger equation is solved self-consistently with the Poisson equation: electron states found by solving the Schrödinger equation are used to calculate the charge distribution that is utilized to solve the Poisson equation, and the electrostatic potential from the Poisson solver is then used in the Schrödinger equation; the process is repeated until self-convergence is achieved.

Ensemble Monte Carlo (EMC) A method for solving the Boltzman transport equation using random numbers, widely employed in simulating carrier transport in semiconductor devices.

Intervalley scattering A scattering process that transfers electrons from one valley to another, mediated by both acoustic and optical phonons that have large momenta (near the first Brillouin zone boundary). Intervalley scattering is modeled as phenomenological deformation potential scattering.

X. Gao, D. Botez, and I. Knezevic, "Multivalley simulation and design of quantum cascade lasers,"
in Encyclopedia of Nanoscience and Nanotechnology, Edited by H. S. Nalwa, American Scientific Publishers, in press. (2008)

Intravalley scattering A scattering process within the same valley, which requires small momentum transfer. Both acoustic and optical phonons can contribute to the intravalley scattering, and they are modeled differently.

Interface phonon A type of polar optical phonon. Electrostatic potential associated with interface phonon shows a peak at the heterojunction between two dissimilar materials due to a difference in the dielectric properties.

Confined phonon A type of polar optical phonon. Electrostatic potential associated with this type of phonon is confined to each layer in a heterostructure, and zero at the interfaces.

Acknowledgement

The authors acknowledge partial support from the Wisconsin Alumni Research Foundation (WARF) and DARPA-EMIL under grant FA8650-07-1-7709.

---

[1] R. F. Kazarinov and R. A. Suris, Sov. Phys. Semicond. **5**, 207 (1971).

[2] J. Faist, F. Capasso, D. L. Sivco, C. Sirtori, A. L. Hutchinson, and A. Y. Cho, Science **264**, 553 (1994).

[3] C. Sirtori, S. Dhillon, C. Faugeras, A. Vasanelli, and X. Marcadet, Physica Status Solidi A **203**, 3533 (2006).

[4] C. Gmachl, F. Capasso, D. L. Sivco, and A. Y. Cho, Rep. Prog. Phys. **64**, 1533 (2001).

[5] J. P. Lima, H. Vargas, A. Miklós, M. Angelmahr, and P. Hess, Appl. Phys. B: Lasers Opt **85**, 279 (2006).

[6] J. Faist, Optics & Photonics News **17**, 32 (2006).

[7] L. Menzel, A. A. Kosterev, R. F. Curl, F. K. Tittel, C. Gmachl, F. Capasso, D. L. Sivco, J. N. Baillargeon, A. L. Huchinson, A. Y. Cho, et al., Appl. Phys. B: Lasers Opt. **72**, 859 (2001).

[8] A. A. Kosterev, F. K. Tittel, W. Durante, M. Allen, R. Köhler, C. Gmachl, F. Capasso, D. L. Sivco, and A. Y. Cho, Appl. Phys. B: Lasers Opt. **74**, 95 (2002).

[9] http:/www.bell-labs.com/org/physicalsciences/projects/qcl/qcl.html (2000).

X. Gao, D. Botez, and I. Knezevic, "Multivalley simulation and design of quantum cascade lasers,"
in Encyclopedia of Nanoscience and Nanotechnology, Edited by H. S. Nalwa, American Scientific Publishers, in press. (2008)

[10] M. Beck, D. Hofstetter, T. Aellen, J. Faist, U. Oesterle, M. Ilegems, E. Gini, and H. Melchior, Science **295**, 301 (2002).

[11] S. Blaser, D. A. Yarekha, L. Hvozdara, Y. Bonetti, A. Muller, M. Giovannini, and J. Faist, Appl. Phys. Lett. **86**, 041109 (2005).

[12] J. S. Yu, S. R. Darvish, A. Evans, J. Nguyen, S. Slivken, and M. Razeghi, Appl. Phys. Lett. **88**, 041111 (2006).

[13] J. S. Yu, A. Evans, S. Slivken, S. R. Darvish, and M. Razeghi, Appl. Phys. Lett. **88**, 251118 (2006).

[14] A. Evans, J. S. Yu, S. Slivken, and M. Razeghi, Appl. Phys. Lett. **85**, 2166 (2004).

[15] A. Evans, J. Nguyen, S. Slivken, J. S. Yu, S. R. Darvish, and M. Razeghi, Appl. Phys. Lett. **88**, 051105 (2006).

[16] L. Diehl, D. Bour, S. Corzine, J. Zhu, G. Hofler, M. Loncar, M. Troccoli, and F. Capasso, Appl. Phys. Lett. **89**, 081101 (2006).

[17] A. Evans, S. R. Darvish, S. Slivken, J. Nguyen, Y. Bai, and M. Razeghi, Appl. Phys. Lett. **91**, 071101 (2007).

[18] J. Faist, F. Capasso, D. L. Sivco, A. L. Hutchinson, S. G. Chu, and A. Y. Cho, Appl. Phys. Lett. **72**, 680 (1998).

[19] R. Colombelli, F. Capasso, C. Gmachl, A. L. Hutchinson, D. L. Sivco, A. Tredicucci, M. C. Wanke, A. M. Sergent, and A. Y. Cho, Appl. Phys. Lett. **78**, 2620 (2001).

[20] M. P. Semtsiv, M. Wienold, S. Dressler, and W. T. Masselink, Appl. Phys. Lett. **90**, 051111 (2007).

[21] D. G. Revin, J. W. Cockburn, M. J. Steer, R. J. Airey, M. Hopkinson, A. B. Krysa, L. R. Wilson, and S. Menzel, Appl. Phys. Lett. **90**, 021108 (2007).

[22] C. Sirtori, H. Page, C. Becker, and V. Ortiz, IEEE J. Quantum Electron. **38**, 547 (2002).

[23] D. Botez, M. D'Souza, G. Tsvid, A. Khandekhar, D. Xu, J. C. Shin, T. Kuech, A. Lyakh, and P. Zory, Wiley Interscience-IEEE Press **380** (2007).

[24] D. P. Xu, M. D'Souza, J. C. Shin, L. J. Mawst, and D. Botez, J. Crystal Growth, in press (2008).

[25] L. R. Wilson, J. W. Cockburn, M. J. Steer, D. A. Carder, M. S. Skolnick, M. Hopkinson, and G. Hill, Appl. Phys. Lett. **78**, 413 (2001).

[26] C. Walther, G. Scalari, and J. Faist, Appl. Phys. Lett. **89**, 231121 (2006).

X. Gao, D. Botez, and I. Knezevic, "Multivalley simulation and design of quantum cascade lasers,"
in Encyclopedia of Nanoscience and Nanotechnology, Edited by H. S. Nalwa, American Scientific Publishers, in press. (2008)

[27] G. Strasser, P. Kruck, M. Helm, J. N. Heyman, L. Hvozdara, and E. Gornik, Appl. Phys. Lett. **71**, 2892 (1997).

[28] C. Sirtori, P. Kruck, S. Barbieri, P. Collot, J. Nagle, M. Beck, J. Faist, and U. Oesterle, Appl. Phys. Lett. **73**, 3486 (1998).

[29] C. Sirtori, P. Kruck, S. Barbieri, H. Page, J. Nagle, M. Beck, J. Faist, and U. Oesterle, Appl. Phys. Lett. **75**, 3911 (1999).

[30] H. Page, A. Robertson, C. Sirtori, C. Becker, G. Glastre, and J. Nagle, IEEE Photon. Technol. Lett. **13**, 556 (2001).

[31] H. Page, C. Becker, A. Robertson, G. Glastre, V. Ortiz, and C. Sirtori, Appl. Phys. Lett. **78**, 3529 (2001).

[32] H. Page, P. Collot, A. Rossi, V. Ortiz, and C. Sirtori, Semicond. Sci. Technol. **17**, 1312 (2002).

[33] S. Anders, W. Schrenk, E. Gornik, and G. Strasser, Appl. Phys. Lett. **80**, 1864 (2002).

[34] C. Pflügl, W. Schrenk, S. Anders, G. Strasser, C. Becker, C. Sirtori, Y. Bonetti, and A. Muller, Appl. Phys. Lett. **83**, 4698 (2003).

[35] H. Page, S. Dhillon, M. Calligaro, V. Ortiz, and C. Sirtori, Electron. Lett. **39**, 1053 (2003).

[36] H. Page, S. Dhillon, M. Calligaro, C. Becker, V. Ortiz, and C. Sirtori, IEEE J. Quantum Electron. **40**, 665 (2004).

[37] C. Becker, C. Sirtori, H. Page, G. Glastre, V. Ortiz, X. Marcadet, M. Stellmacher, and J. Nagle, Appl. Phys. Lett. **77**, 463 (2000).

[38] W. Schrenk, N. Finger, S. Gianordoli, E. Gornik, and G. Strasser, Appl. Phys. Lett. **77**, 3328 (2000).

[39] L. R. Wilson, D. A. Carde, J. W. Cockburn, R. P. Green, D. G. Revin, M. J. Steer, M. Hopkinson, G. Hill, and R. Airey, Appl. Phys. Lett. **81**, 1378 (2002).

[40] D. A. Carder, L. R. Wilson, R. P. Green, J. W. Cockburn, M. Hopkinson, M. J. Steer, R. Airey, and G. Hill, Appl. Phys. Lett. **82**, 3409 (2003).

[41] R. C. Iotti and F. Rossi, Phys. Rev. Lett. **87**, 146603 (2001).

[42] F. Compagnone, A. D. Carlo, and P. Lugli, Appl. Phys. Lett. **80**, 920 (2002).

[43] H. Callebaut, S. Kumar, B. S. Williams, Q. Hu, and J. L. Reno, Appl. Phys. Lett. **84**, 645 (2004).

[44] O. Bonno, J. L. Thobel, and F. Dessenne, J. Appl. Phys. **97**, 043702 (2005).

X. Gao, D. Botez, and I. Knezevic, "Multivalley simulation and design of quantum cascade lasers,"
in Encyclopedia of Nanoscience and Nanotechnology, Edited by H. S. Nalwa, American Scientific Publishers, in press. (2008)

[45] D. Indjin, P. Harrison, R. W. Kelsall, and Z. Ikonić, J. Appl. Phys. **91**, 9019 (2002).

[46] V. D. Jovanović, D. Indjin, N. Vukmirović, Z. Ikonić, P. Harrison, and E. H. Linfield, Appl. Phys. Lett. **86**, 211117 (2005).

[47] S. C. Lee and A. Wacker, Phys. Rev. B **66**, 245314 (2002).

[48] S. C. Lee, F. Banit, M. Woerner, and A. Wacker, Phys. Rev. B **73**, 245320 (2006).

[49] R. C. Iotti and F. Rossi, Rep. Prog. Phys. **68**, 2533 (2005).

[50] F. Eickemeyer, K. Reimann, M. Woerner, and T. Elsaesser, Phys. Rev. Lett. **89**, 047402 (2002).

[51] M. Woerner, K. Reimann, and T. Elsaesser, J. Phys: Condens. Matter **16**, R25 (2004).

[52] V. D. Jovanović, S. Höfling, D. Indjin, N. Vukmirović, Z. Ikonić, P. Harrison, J. P. Reithmaier, and A. Forchel, J. Appl. Phys. **99**, 103106 (2006).

[53] D. Indjin, S. Tomić, Z. Ikonić, P. Harrison, R. W. Kelsall, V. Milanović, and S. Kočinac, Appl. Phys. Lett. **81**, 2163 (2002).

[54] A. Mirčetić, D. Indjin, Z. Ikonić, P. Harrison, V. Milanović, and R. W. Kelsall, J. Appl. Phys. **97**, 084506 (2005).

[55] C. A. Evans, V. D. Jovanović, D. Indjin, Z. Ikonić, and P. Harrison, Appl. Phys. Lett. **87**, 141109 (2005).

[56] C. Jacoboni and P. Lugli, *The Monte Carlo Method for Semiconductor Device Simulation* (Springer-Verlag, New York, 1989).

[57] S. R. Jin, C. N. Ahmad, S. J. Sweeney, A. R. Adams, B. N. Murdin, H. Page, X. Marcadet, C. Sirtori, and S. Tomic, Appl. Phys. Lett. **89**, 221105 (2006).

[58] X. Gao, D. Botez, and I. Knezevic, Appl. Phys. Lett. **89**, 191119 (2006).

[59] X. Gao, D. Botez, and I. Knezevic, J. Appl. Phys. **101**, 063101 (2007).

[60] D. Indjin, P. Harrison, R. W. Kelsall, and Z. Ikonić, Appl. Phys. Lett. **81**, 400 (2002).

[61] V. Spagnolo, G. Scamarcio, H. Page, and C. Sirtori, Appl. Phys. Lett. **84**, 3690 (2004).

[62] M. Lundstrom, *Fundamentals of Carrier Transport* (University Press, Cambridge, 2000).

[63] K. Tomizawa, *Numerical Simulation of Submicron Semiconductor Devices* (Artech House, Boston, 1993).

[64] S. L. Chuang, *Physics of Optoelectronic Devices* (Wiley Interscience, New York, 1995).

[65] L. R. Ram-Mohan, K. H. Yoo, and R. L. Aggarwal, Phys. Rev. B **38**, 6151 (1988).

[66] G. Liu and S. L. Chuang, Phys. Rev. B **65**, 165220 (2002).

X. Gao, D. Botez, and I. Knezevic, "Multivalley simulation and design of quantum cascade lasers,"
in Encyclopedia of Nanoscience and Nanotechnology, Edited by H. S. Nalwa, American Scientific Publishers, in press. (2008)

[67] C. R. Pidgeon and R. N. Brown, Phys. Rev. **146**, 575 (1966).

[68] J. M. Luttinger and W. Kohn, Phys. Rev. **97**, 869 (1955).

[69] E. O. Kane, *Semiconductors and Semimetals*, vol. 1 (Academic, New York, 1966).

[70] G. L. Bir and G. E. Pikus, *Symmetry and Strain-Induced Effects in Semiconductors* (Wiley, New York, 1974).

[71] I. Vurgaftman and J. R. Meyer, J. Appl. Phys. **89**, 5815 (2001).

[72] B. Chen, M. Lazzouni, and L. R. Ram-Mohan, Phys. Rev. B **45**, 1204 (1992).

[73] X. Cartoixá, D. Z.-Y. Ting, and T. C. McGill, J. Appl. Phys. **93**, 3974 (2003).

[74] L. R. Ram-Mohan, K. H. Yoo, and J. Moussa, J. Appl. Phys. **95**, 3081 (2004).

[75] F. Szmulowicz, Phys. Rev. B **71**, 245117 (2005).

[76] S. Barbieri, F. Beltram, and F. Rossi, Phys. Rev. B **60**, 1953 (1999).

[77] B. Vinter, Phys. Rev. B **66**, 045324 (2002).

[78] E. J. Roan and S. L. Chuang, J. Appl. Phys. **69**, 3249 (1991).

[79] K. T. Kim, S. S. Lee, and S. L. Chuang, J. Appl. Phys. **69**, 6617 (1991).

[80] P. Lugli and D. K. Ferry, IEEE Trans. Electron Devices **ED-32**, 2431 (1985).

[81] S. M. Goodnick and P. Lugli, *Hot Carriers in Semiconductor Nanostructures* (Academic, New York, 1992).

[82] H. Rücker, E. Molinari, and P. Lugli, Phys. Rev. B **45**, 6747 (1992).

[83] O. E. Raichev, Phys. Rev. B **49**, 5448 (1994).

[84] A. Mošková and M. Moško, Phys. Rev. B **49**, 7443 (1994).

[85] M. Moško, A. Mošková, and V. Cambel, Phys. Rev. B **51**, 16860 (1995).

[86] M. V. Fischetti, J. Appl. Phys. **89**, 1232 (2001).

[87] S. M. Goodnick and P. Lugli, Appl. Phys. Lett. **51**, 584 (1987).

[88] S. M. Goodnick and P. Lugli, Phys. Rev. B **37**, 2578 (1988).

[89] M. Moško and A. Mošková, Phys. Rev. B **44**, 10794 (1991).

[90] S. Barbieri, C. Sirtori, H. Page, M. Stellmacher, and J. Nagle, Appl. Phys. Lett. **78**, 282 (2001).

[91] R. C. Iotti and F. Rossi, Appl. Phys. Lett. **78**, 2902 (2001).

[92] P. Harrison, Appl. Phys. Lett. **75**, 2800 (1999).

[93] P. Harrison, D. Indjin, and R. W. Kelsall, J. Appl. Phys. **92**, 6921 (2002).

[94] X. Gao, M. D'Souza, D. Botez, and I. Knezevic, J. Appl. Phys. **102**, 113107 (2007).

X. Gao, D. Botez, and I. Knezevic, "Multivalley simulation and design of quantum cascade lasers,"
in Encyclopedia of Nanoscience and Nanotechnology, Edited by H. S. Nalwa, American Scientific Publishers, in press. (2008)

[95] X. Gao, M. D'Souza, D. Botez, and I. Knezevic, Opt. Quantum Electron., submitted (September 2007).

[96] D. P. Xu, A. Mirabedini, M. D'Souza, S. Li, D. Botez, A. Lyakh, Y. J. Shen, P. Zory, and C. Gmachl, Appl. Phys. Lett. **85**, 4573 (2004).

[97] S. Gianordoli, W. Schrenk, L. Hvozdara, N. Finger, G. Strasser, and E. Gornik, Appl. Phys. Lett. **76**, 3361 (2000).

[98] C. G. V. de Walle, Phys. Rev. B **39**, 1871 (1989).

[99] W. G. Spitzer and J. M. Whelan, Phys. Rev. **114**, 59 (1959).

[100] R. C. Iotti and F. Rossi, Semicond. Sci. Technol. **19**, S323 (2004).

[101] H. Rücker, E. Molinari, and P. Lugli, Phys. Rev. B **44**, 3463 (1991).

[102] P. Lugli, P. Bordone, E. Molinaris, H. Rüker, A. M. de Paula, A. C. Maciel, J. F. Ryan, and M. Shayegan, Semicond. Sci. Technol. **7**, B116 (1992).

[103] B. S. Williams and Q. Hu, J. Appl. Phys. **90**, 5504 (2001).

[104] V. M. Menon, W. D. Goodhue, A. S. Karakashian, and L. R. Ram-Mohan, J. Appl. Phys. **88**, 5262 (2000).

[105] H. B. Teng, J. P. Sun, G. I. Haddad, M. A. Stroscio, S. Yu, and K. W. Kim, J. Appl. Phys. **84**, 2155 (1998).

[106] F. Compagnone, A. D. Carlo, and P. Lugli, Phys. Rev. B **65**, 125314 (2002).

[107] G. Scarpa, P. Lugli, N. Ulbrich, G. Abstreiter, M. C. Amann, M. Manenti, F. Compagnone, and A. D. Carlo, Semicond. Sci. Technol. **19**, S342 (2004).

[108] F. Compagnone, M. Manenti, A. D. Carlo, and P. Lugli, Physica B **314**, 336 (2002).

[109] X. Gao, D. Botez, and I. Knezevic, J. Appl. Phys., in press (2008).

[110] X. Gao, D. Botez, and I. Knezevic, J. Comput. Electron., in press (2008).

[111] M. A. Stroscio and M. Dutta, *Phonons in Nanostructures* (Cambridge University Press, 2001).

[112] S. Yu, K. W. Kim, M. A. Stroscio, G. J. Iafrate, J. P. Sun, and G. I. Haddad, J. Appl. Phys. **82**, 3363 (1997).

[113] B. K. Ridley, *Electrons and Phonons in Semiconductor Multilayers* (Cambridge University Press, 1997).

[114] M. Babiker, J. Phys. C: Solid St. Phys. **19**, 683 (1986).

[115] K. Huang and B. Zhu, Phys. Rev. B **38**, 13377 (1988).

X. Gao, D. Botez, and I. Knezevic, "Multivalley simulation and design of quantum cascade lasers,"
in Encyclopedia of Nanoscience and Nanotechnology, Edited by H. S. Nalwa, American Scientific Publishers, in press. (2008)

[116] K. J. Nash and D. J. Mowbray, J. Lumin **44**, 315 (1989).

[117] X. Zianni, P. N. Butcher, and I. Dharssi, J. Phys.: Condens. Matter **4**, L77 (1992).

[118] K. J. Nash, Phys. Rev. B **46**, 7723 (1992).

[119] N. C. Constantinou and B. K. Ridley, Phys. Rev. B **49**, 17065 (1994).

[120] I. Lee, S. M. Goodnick, M. Gulia, E. Molinari, and P. Lugli, Phys. Rev. B **51**, 7046 (1995).

[121] C. Becker, C. Sirtori, H. Page, A. Robertson, V. Ortiz, and X. Marcader, Phys. Rev. B **65**, 085305 (2002).

[122] K. W. Kim and M. A. Stroscio, J. Appl. Phys. **68**, 6289 (1990).

[123] M. E. Pistol and X. Liu, Phys. Rev. B **45**, 4312 (1992).

[124] G. Armelles, M. J. Sanjuan, L. Gonzalez, and Y. Gonzalez, Appl. Phys. Lett. **68**, 1805 (1996).

[125] G. Burns, C. R. Wie, F. H. Dacol, G. D. Pettit, and J. M. Woodall, Appl. Phys. Lett. **51**, 1919 (1987).

[126] Z. C. Feng, S. Perkowitz, D. K. Kinell, R. L. Whitney, and D. N. Talwar, Phys. Rev. B **47**, 13466 (1993).

[127] J. Groenen, R. Carles, G. Landa, C. G. Piecourt, C. Fontaine, and M. Gendry, Phys. Rev. B **58**, 10452 (1998).

[128] Y. S. Chen, W. Shockley, and G. L. Pearson, Phys. Rev. **151**, 648 (1966).

[129] G. Xu and A. Li, Phys. Rev. B **71**, 235304 (2005).

[130] L. Wendler, Phys. Stat. Sol.(b) **129**, 513 (1985).

[131] L. Wendler and R. Pechstedt, Phys. Stat. Sol.(b) **141**, 129 (1987).

[132] N. Mori and T. Ando, Phys. Rev. B **40**, 6175 (1989).

[133] M. Born and K. Huang, *Dynamical Theory of Crystal Lattices* (Oxford University Press, Oxford, 1954).

X. Gao, D. Botez, and I. Knezevic, "Multivalley simulation and design of quantum cascade lasers,"
in Encyclopedia of Nanoscience and Nanotechnology, Edited by H. S. Nalwa, American Scientific Publishers, in press. (2008)